Adaptive and Reconfigurable Architected Materials Driven by Electrochemistry

Thesis by

Xiaoxing Xia

In Partial Fulfillment of the Requirements for

the degree of

Doctor of Philosophy

CALIFORNIA INSTITUTE OF TECHNOLOGY

Pasadena, California

2019

Defended May 21, 2019

Xiaoxing Xia
ORCID: 0000-0003-1255-3289

ACKNOWLEDGEMENTS

This journey has been the most joyful, challenging, and satisfying period of my life so far. I wouldn't have made it through all the difficulties leading to such a small yet meaningful scientific discovery if it weren't for the amazing support group that I am so fortunate to have. First and foremost, I would like to thank my academic advisor, or in her words my academic "mother", Prof. Julia R. Greer. Over the years, Julia has been my teacher, mentor, role model, and friend, but most importantly, she is my champion. She taught me how to ask the most fundamental questions, showed me what it means to be completely fearless and dedicated, and somehow managed to instill faith into me for my own work and for the elusive answers that I am striving to find. I would also like to thank Prof. Claudio V. Di Leo and Prof. Dennis M. Kochmann for being the best collaborators that I could ever ask for. I am so grateful to Prof. William L. Johnson for being a great source of inspiration from the thermodynamics classes in the first year to the endless discussions on statistical mechanics during my last year at Caltech. I want to thank Prof. Katherine T. Faber, Prof. Chiara Daraio, Prof. Harry A. Atwater, and Prof. Morteza Gharib for their insightful advice as members of my thesis and candidacy committee.

I would also like to thank the great community that I am so lucky to have at Caltech. Every member of the Greer group has made this place more like a home for me. I thank Lucas Meza and Wendy Gu for being great mentors ever since I first started to do research. I thank Dylan Tozier, Ottman Tertuliano, Alessandro Maggi, Xiaoyue Ni, Daryl Yee, Carlos Portela, and Andrey Vyatskikh for the countless inspiring and brain-picking discussions throughout the years. I thank Arturo Mateos, Max Lifson, Mike Citrin, Bryce Edwards, Anthony Kwong, Kai Narita, and all other Greer group members for filling my PhD years with great fun and friendship. I am particularly grateful to Dr. Heng Yang for being the elder brother I never had in my life, and to Cong Wang for being such a great friend. I thank Melissa Melendes, Matthew Hunt, Guy DeRose, Nathan Lee, Bruce Brunschwig for being so accommodating and generous to me in KNI and MMRC at Caltech. I would also like to thank Christy Jenstad, Cecilia Gamboa, and Angie Riley for making things so much easier for all students in the department.

Finally, I would like to acknowledge my dearest family for their unwavering support during my PhD and in my life. I thank my wife Fengwan Wang for always having faith in me, and I own her a lot of apologies for all the vacations we couldn't have. Wanwan, you are the love of my life and thank you for giving me the best gift I have ever had, our little boy. My dear son, I would like to thank you for making me realize what the most important things in life are, and I hope you will always enjoy whatever you want to do in your life. I would also like to thank my parents, Xilan Xia and Yi Chi, for raising me to the person I am today. They poured everything they had to my upbringing and never hesitated a bit when sending me abroad to receive the best education. Lastly, I would like to thank my parent-in-law, Rui Wang and Rong Liu, for allowing me to marry their precious daughter and for their support and patience for me during all these years. I know they are just as proud as my parents are for my accomplishment when I finally get my PhD.

ABSTRACT

Architected materials are a new class of engineered materials with carefully controlled internal structures that give rise to properties that differ from or surpass those of their constituent materials. Recent advances in additive manufacturing provide an extraordinary opportunity to rationally design the structure and the chemical composition of architected materials across multiple length scales to optimize properties and functionalities for a variety of applications. These functional architected materials are capable of decoupling critical trade-offs, such as strength vs. density, to reach new regions of the material property space, and enabling exotic properties that rarely exist in classical materials such as negative refraction and negative thermal expansion.

This thesis probes into the dynamic behaviors of architected materials undergoing electrochemical reactions and aims to provide an in-depth understanding of the underlying mechanisms as well as design principles generalizable for other functional architected material systems. We developed novel fabrication methods based on two-photon lithography and various physical and chemical post-processing techniques to create architected materials with multi-level design freedom including feature sizes, structural geometries, and material compositions, which resonates with the multi-faceted challenges in electrochemical systems. We demonstrated that architected materials provide a new platform to design battery electrodes that could accommodate the large volumetric changes associated with conversion-based electrode materials, while decoupling the longstanding trade-off between active material loading and transport kinetics in batteries. Furthermore, we presented a new class of electrochemically reconfigurable architected materials that could transform their structures in a programmable, reversible and non-volatile fashion, which provide new vistas for designing mechanical metamaterials with tunable phononic bandgaps and deployable micro-devices for biomedical applications.

The multi-scale and multi-physics nature of these electrochemically driven architected materials prompted us to develop a toolset of (1) *in situ* SEM and optical microscopy to visualize the dynamic responses, (2) coupled chemo-mechanical finite element analysis to reconstruct detailed mechanical evolution as electrochemical reactions proceed, and (3) a

statistical mechanics framework to capture the transient interactions between coupled mechanical instabilities. Using these tools, we investigated lithiation-induced cooperative beam buckling in tetragonal Si microlattices: from the deformation mechanisms of individual beams and the cooperative coupling between buckling directions of neighboring beams to the lithiation rate-dependent distribution of ordered buckling domains separated by distorted domain boundaries. Results indicate that local defects and stochastic energy fluctuations play a critical role in the dynamic response of architected materials in a way analogous to that during phase transformations of classical materials. These connections have profound implications on how we could understand and design architected materials by drawing inspiration from established theories in materials science.

PUBLISHED CONTENT AND CONTRIBUTIONS

Chapter 3 had been adapted from:

(1) **Xia, X.**, Di Leo, C. V., Gu, X. W. & Greer, J. R. In situ lithiation-delithiation of mechanically robust Cu-Si core-shell nanolattices in a scanning electron microscope. *ACS Energy Letters* 1, 492–499 (2016). DOI: 10.1021/acsenergylett.6b00256

Contribution: X.X. conceived the study, developed, fabricated and characterized the samples, designed and implemented the *in situ* SEM setup, and wrote the manuscript.

(2) Yang. H., Citrin, M., **Xia, X.**, Nieh, S., Greer, J. R. Microstructure evolution in "Li-free" thin film solid-state batteries. *In preparation* (2019).

Contribution: X.X. participated in the conception of this study, and designed the *in situ* SEM setup for visualizing the Li nucleation process.

Chapter 4 had been adapted from:

(3) **Xia, X.**, Afshar, A., Yang, H., Portela, C. M., Kochmann, D. M., Di Leo, C. V., Greer, J. R. Electrochemically reconfigurable architected materials. *Under review* (2019).

Contribution: X.X. conceived the study, developed the fabrication process, fabricated all samples, designed the experimental setups, conducted electrochemical testing, analyzed the data and the domain maps, conducted the Monte Carlo simulations, and wrote the manuscript.

TABLE OF CONTENTS

LIST OF ILLUSTRATIONS AND TABLES

Chapter 1

INTRODUCTION

1.1 What Are Architected Materials?

Architected materials are engineered materials with carefully controlled internal structures that give rise to properties that differ from or surpass those of their constituent materials. Such spatial variations of multiple material components or quite commonly of materials and open space provide a new degree of architectural freedom to design materials for enhanced functionalities. The structures of architected materials could be stochastic or ordered in one, two, or all three dimensions. Well-established architected materials such as foams, lamellar structures, or honeycombs have been widely used primarily for improved mechanical properties at a reduced weight compared to their bulk constituents. Recent advances of additive manufacturing provide an extraordinary opportunity to rationally design architected materials to optimize specific properties for various applications. Additive manufacturing, more commonly known as 3D printing, could produce almost any arbitrary 3D geometries with intricate structures spanning multiple lengths scales. The increasingly higher resolution, broader material options, and better architectural control of 3D printing and post-processes have enabled exotic material properties in architected materials such as negative Poisson's ratios [1,2], negative refractive indices [3,4], photonic and phononic bandgaps [5–8], and mechanical strengths approaching the theoretical limits [9,10].

1.2 Nature's Hierarchical Designs

Nature provides the best inspiration for architected materials. It is almost impossible to find any biological systems of homogenous, bulk material components without sophisticated 3D architectures. Evolution has taught biological species to optimize material architectures to adapt to stringent, multi-faceted environmental challenges with limited resources. Bone is a fascinating example of biological materials with hierarchical architectures spanning eight orders of magnitude in length scales as illustrated in Fig. 1.1 [11]. Such intricate internal structures give rise to bone's simultaneous high strength and high toughness while being lightweight and even self-healing.

However, this highly efficient and multi-functional hierarchical architecture also poses significant challenges for medical implants such as joint replacements made from engineering materials.

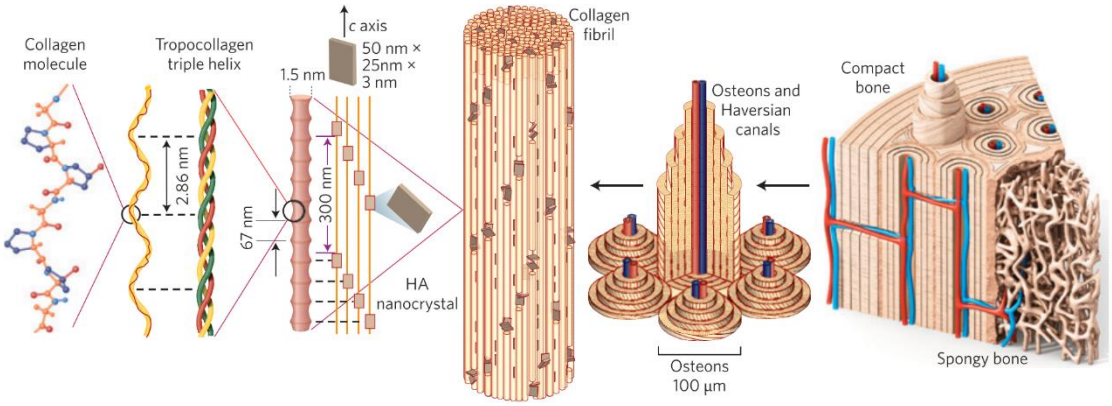

Figure 1.1 Hierarchical architecture of bone spanning eight orders of magnitude in length scales. Adapted from [11].

To some extent, architected materials originate from mimicking the biological systems with the honeycomb structure as a prime example. By investigating the structure–property relations of nacre shells, "brick-and-mortar" ceramic composites are made to achieve high toughness and strength [12]. Biological materials can also provide their intricate architectures as templates for further engineering. For example, natural woods have been processed into high-performance structural materials with a more than tenfold increase in strength, toughness and ballistic resistance by chemical treatment and densification while preserving the internal hierarchical structure [13]. Ultimately, fundamental design principles can be generalized from natural materials to be applied to architected materials based on the demands for specific applications. One example of such bio-inspired design parameters is the fractal order in hierarchical architecture, which has been explored in hollow alumina nanolattices [14]. However, due to the complex, multi-functional nature of biological systems, it is difficult to decipher the contribution of different architectural features from the combined results. Therefore, it is important to establish a framework to isolate and investigate individual aspects of structure-property relations in architected materials.

1.3 Remarkable Properties of Architected Materials

The notion of optimizing structural design has been practiced for centuries in ancient buildings and towers as well as modern bridges, stadiums and skyscrapers. Individual beams, plates, arches, and

cables are assembled into intricate architectures in the most efficient, reliable, and resilient way through meticulous calculation and thoughtful design. Architected materials borrow this concept of structural design to enhance the performance of the constituent materials, but architected materials are used as *materials with redefined properties that homogenize the entire structure* such as density for lightweight foams. Occasionally, they are referred to as metamaterials because their topological structures resemble the atomic structures for classical materials in a sense that the geometric structures (lattices) govern the material properties, but the individual building blocks (unit cells) are not discretized during practical usage, creating an effective separation of scales. In this section, we survey some exciting discoveries of the remarkable properties of architected materials in the literature for those who are unfamiliar with this emerging field. A few outstanding examples are provided in Fig. 1.2.

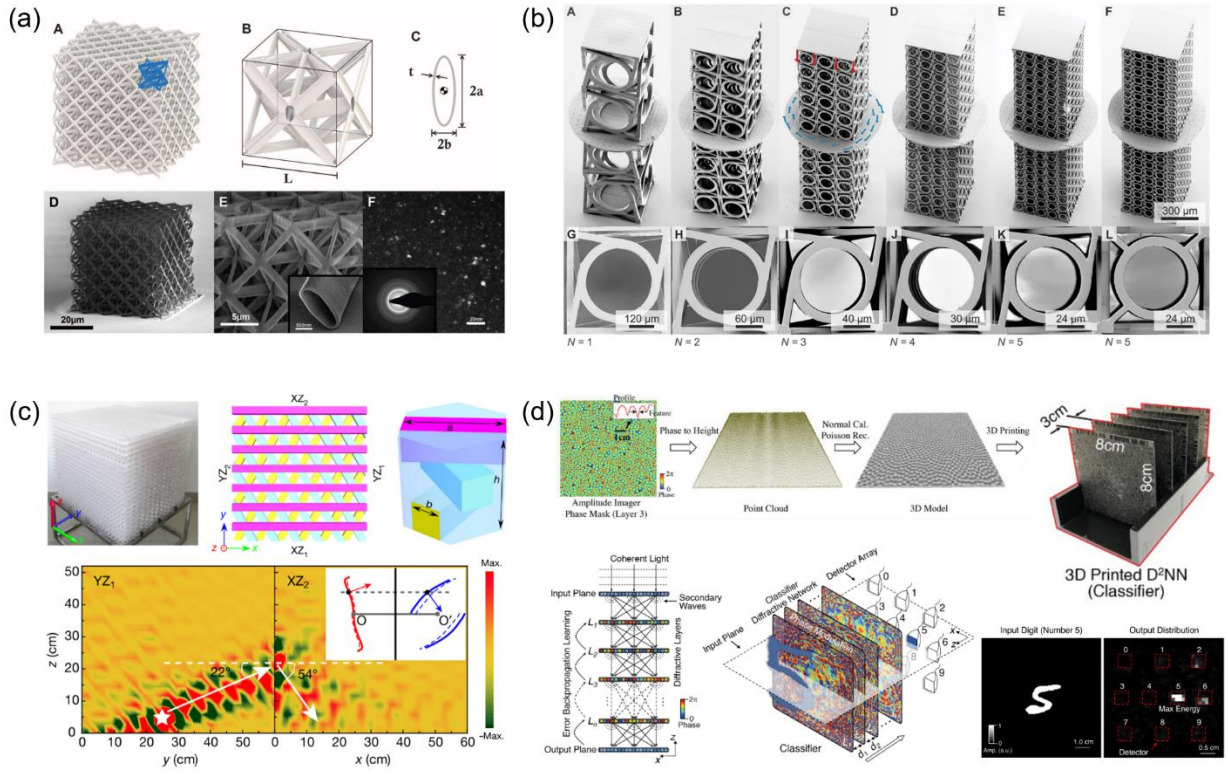

Figure 1.2 Examples of architected materials' novel properties. (a) Strong, lightweight, and recoverable 3D ceramic nanolattices [10]. (b) Mechanical metamaterials that twist upon compression [15]. (c) a Weyl phononic crystal with topological negative refraction for surface acoustic waves [4]. (d) An all-optical Diffractive Deep Neural Network architecture that could implement image classification [16].

Structural Mechanics

One of the most important motivations for architected materials is to build lightweight structural materials with tailored mechanical properties such as high stiffness, high strength, and high toughness. Significant research efforts have been using additive manufacturing methods to miniaturize the lattice truss structures widely used in construction of buildings and bridges such as octet, kagome and honeycomb lattices [10,14,17–21]. One promising direction is to take advantage of the small-scale size effects to improve mechanical properties. These nanosizing effects have been observed and investigated in nanoscale elements such as thin films (e.g., graphene [22]), nanowires [23] and nanopillars [24], but they are difficult to utilize at larger form factors relevant to practical applications. Architected materials provide a platform to proliferate the superior mechanical properties at small scales to larger structures. Dimensional confinement in solid, hollow or composite beams of architected materials can induce strengthening for nano-crystalline metals [18,19], toughening for brittle materials [10,14], and defect and damage tolerance for metallic glasses and ceramics [9,25,26], which have enabled 3D nanolattices that are ultra-strong, lightweight and mechanically resilient. These fascinating mechanical properties call for systematic and multi-scale modeling frameworks [27,28] that combine classical beam and rigidity theories in structural mechanics and size-dependent phenomena in small-scale mechanics.

Unusual and Non-linear Reponses

The design flexibility enabled by additive manufacturing allows for innovative material architecture to achieve exotic properties that are impossible or unusual in the past. Architected materials have been shown to exhibit negative Poisson's ratios [1,2], negative thermal expansion [29,30], and near infinite bulk-to-shear modulus ratios [31]. The ability to create structures with designed curvature have enabled architected materials that can twist upon uniaxial loading [15] and demonstrate handedness upon shearing [32]. Non-linear responses upon deformation can be programed through buckling and snapping instabilities to enable novel mechanisms for shock absorption and structural transformation [33–35]. The development of architected material with non-linear responses is still in its early stage with a vast amount of design space unexplored. New algorithms based on space-filling tessellation [36] and combinatorial selection [37] are developed to search from and program reconfigurable and shape-morphing architected materials. Disordered structures and geometric

frustration in architected materials are also being investigated with fundamental implications [38–40].

Wave Propagation

When the unit cell size of periodic structures approaches that of electromagnetic or acoustic waves at certain frequencies, architected materials could interfere and therefore control wave propagation, a phenomenon more commonly described as photonic or phononic crystals [41,42]. Due to Bragg scattering and local resonance, carefully designed architected materials exhibit dispersion relations (i.e. band diagrams) with bandgaps in one, two or three dimensions [5–8]. Such bandgaps give rise to interesting and useful properties like structural coloration and vibration cancellation. Further dispersion relation engineering could produce negative refractive indices [3,4] and cloaking mechanisms [43–45] for light, sound and heat. Architected materials with chirality [46,47] and non-reciprocity [48,49] have been designed and fabricated with promises for future optical and acoustic logic and computation. Recently, researchers have computationally trained optical diffractive layers for machine learning and 3D printed the Diffractive Deep Neural Network architectures to perform complex functions such as image analysis and object classification [16], shedding light on what architected materials can potentially achieve through interacting with waves.

Topological Metamaterials

Architected materials also provide a platform to create mechanical and photonic topological metamaterials [50,51] that are analogous to electronic topological insulators [52]. Electronic topological insulators can be analyzed by simply focusing on how Fermi surface topology interacts with band structure to define available electron states without any microscopic details. Similarly, topological metamaterials display topologically protected properties that are insensitive to smooth deformation and presence of defects. Purposefully designed architected materials can utilize such topologically protected properties to achieve distinct and robust functionalities. Through topological polarization induced by symmetry breaking [53], mechanical metamaterials can be reconfigured by the motion of floppy modes [54], alter their deformability and rigidity [55], program the location of failure [56], and exhibit static non-reciprocity [57]. Beyond these zero-frequency properties, architected materials can also have topologically protected edge states for phononic or photonic wave propagation. The localization at the edge is not a result of local variation of the material properties,

but a manifestation of a more general topological feature of the corresponding band structure, as characterized by the presence of integer-valued topological invariants such as the Chern number. Based on this mechanism, topological metamaterials with designed architectures can facilitate unidirectional propagation of edge states that are immune to defects and back-scattering for both phonons and photons [49,58–60], with potential applications in vibration isolation and waveguides.

1.4 What is Electrochemistry?

Electrochemistry is the branch of chemistry that studies the relationship between electricity and chemical reactions, with either electricity being an outcome of a particular chemical reaction or vice versa. Similar to just about any chemical reactions, an electrochemical reaction has two or more reactants undergoing an oxidation-reduction (redox) reaction with each other. However, in an electrochemical cell, the two reactants, normally referred to as electrodes, are separated by an ion conducting but electron insulating electrolyte in a liquid or solid phase, while they are also connected by an external electric circuit. The redox reaction between the two electrodes could happen if and only if the current of ions in the electrolyte and the current of electrons in the external circuit flow together. It is due to this separation of electron flow and ion flow that the rate and even the direction of electrochemical reactions can be gauged by controlling current in the external circuit. There are two kinds of electrochemical reactions known as galvanic cells and electrolytic cells as illustrated in Fig. 1.3. In a galvanic cell, the positive electrode has a higher potential than the negative electrode, which causes current in the external circuit to flow spontaneously from the positive electrode to the negative electrode. This corresponds to the discharge process in a battery where energy is released from the reaction and used to power electronics. In an electrolytic cell, by applying an external voltage, current can flow in the reverse direction from the negative electrode to the positive electrode in the external circuit. This corresponds to the charge process in a battery, where external energy is used to revert the electrodes back to their original states before discharge.

Electrochemistry is extremely important for a large variety of applications including but not limited to energy storage (batteries and fuel cells), automobile and manufacturing industries (electroplating, coating), and brine mining (chlorine and sodium hydroxide production). Designing an electrochemical cell for specific applications is a multi-faceted engineering challenge. Key considerations include ion transport inside the electrolyte, electron transport inside both electrodes,

electrode surface area, chemical reversibility, parasitic side reactions that consume the electrodes and electrolyte, and the conductivity and mechanical stability of the reaction products on both electrodes. Therefore the vast design space of architected materials can be explored rationally to improve the performance of specific electrochemical systems and decouple critical trade-offs that are normally correlated.

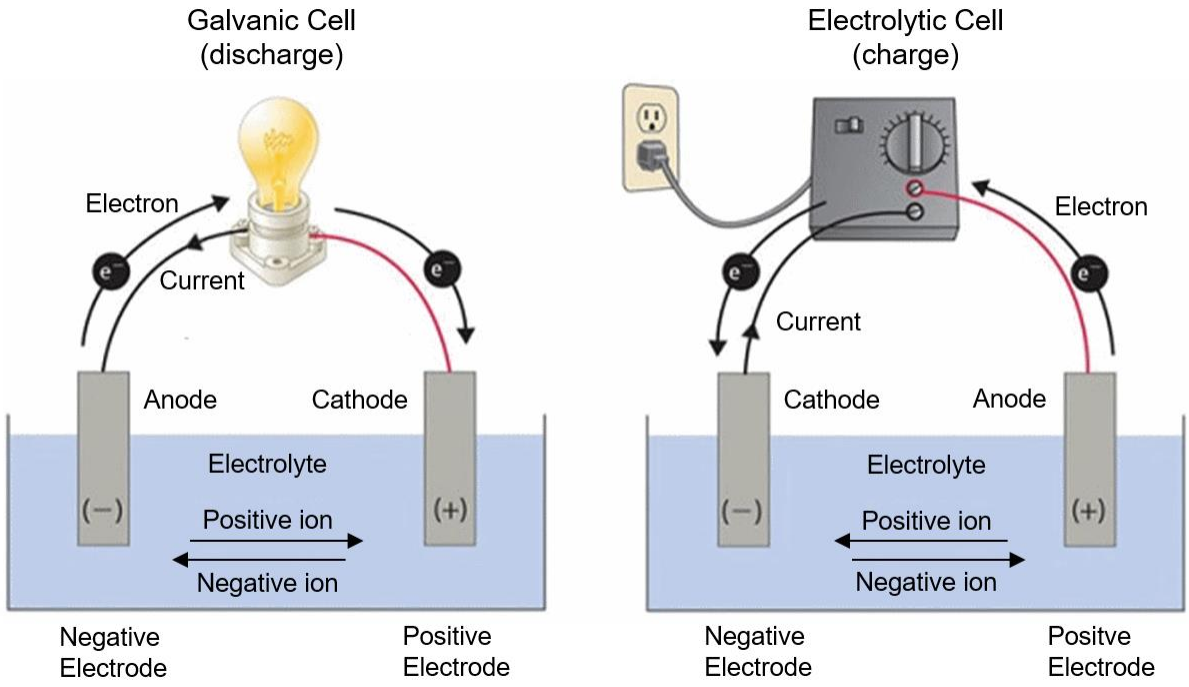

Figure 1.3 Illustration of a galvanic cell and an electrolytic cell. The background image is adapted from [61].

1.5 Thesis Overview

The aim of this thesis is to explore, understand, and eventually design architected materials that exhibit novel properties in electrochemical systems. Specifically, we investigate the dynamic responses of architected materials undergoing electrochemical reactions. The multi-level design freedom of architected materials, including feature sizes, structural geometries, and chemical compositions, resonates with the multi-faceted challenges and trade-offs in electrochemical systems. The first chapter introduces the concept and previous studies of architected materials, and then presents a background of electrochemistry. The second chapter discusses key additive manufacturing and post-processing methods to fabricate architected materials and provides guidelines for rational design of functional architected materials, especially in electrochemical

systems. The third chapter demonstrates an example of how adaptive architected materials could accommodate the severe volume expansion of Si anodes in Li-ion batteries; the forth chapter shows that electrochemistry can also be used to dynamically and reversibly reconfigure the structure and therefore control the properties of architected materials. In the fifth chapter, we summarize the work presented in this thesis by drawing an analogy between the dynamic behaviors of architected materials and those of classical materials. In the end, we discuss open questions and future research directions of architected materials and envision the path towards large-scale production and real-world applications.

Chapter 2

TAILOR-MAKING FUNCTIONAL ARCHITECTED MATERIALS BY DESIGN

2.1 Design of Functional Architected Materials

Despite the fruitful characterization of novel properties in architected materials, practical demonstrations of functional architected materials are still sparse. One key limitation is still the high cost and low speed for manufacturing architected materials at scale, even though significant advancement has been made in the past decade. Therefore, choosing the proper additive manufacturing method with the required spatial resolution, printing size, and speed based on specific applications is of crucial importance. Furthermore, existing additive manufacturing methods, especially those with higher resolutions and relatively lower fabrication costs, are predominantly based on polymer or plastic materials. It is therefore necessary to broaden the material selection to include metals, semiconductors, ceramics and their composites through post-processing treatments such as material coating or conversion. For examples, an effective realization of functional architected materials for electrochemical systems would include a 3D-printable polymer scaffold to define the structural geometry, a conductive layer for electron conductivity throughout the architecture, and another layer of electrochemically active materials for specific redox reactions. It is only after the relevant materials and efficient fabrication techniques are carefully planned that one could design, test, and optimize the architecture design of functional architected materials. Design principles from civil engineering such as truss-based lattices [10,14,20,21] and from materials science such as twinning boundaries and precipitates [62] can be investigated as inspiration even though such analogy only applies to a certain extent. Systematic search algorithms, selective pruning and parameter optimization, and machine learning approaches can be further utilized to explore the unlimited design space.

2.2 Additive Manufacturing Methods for Architected Materials

Additive manufacturing has been more readily adopted in high value-added industries such as aerospace, automobile, and medical devices to custom-make individual parts on demand with a shorter turnaround time. For these applications, metal 3D printing by established methods like powder bed fusion is used to produce certified, high quality parts that are difficult or expensive to machine. However, these methods are too expensive and do not have the required spatial resolution for making architected materials that utilize the additional degree of freedom of the 3D architecture to define novel properties and new functionalities. In this section, we overview three major approaches to 3D print architected materials, and each has its own pros and cons for different applications.

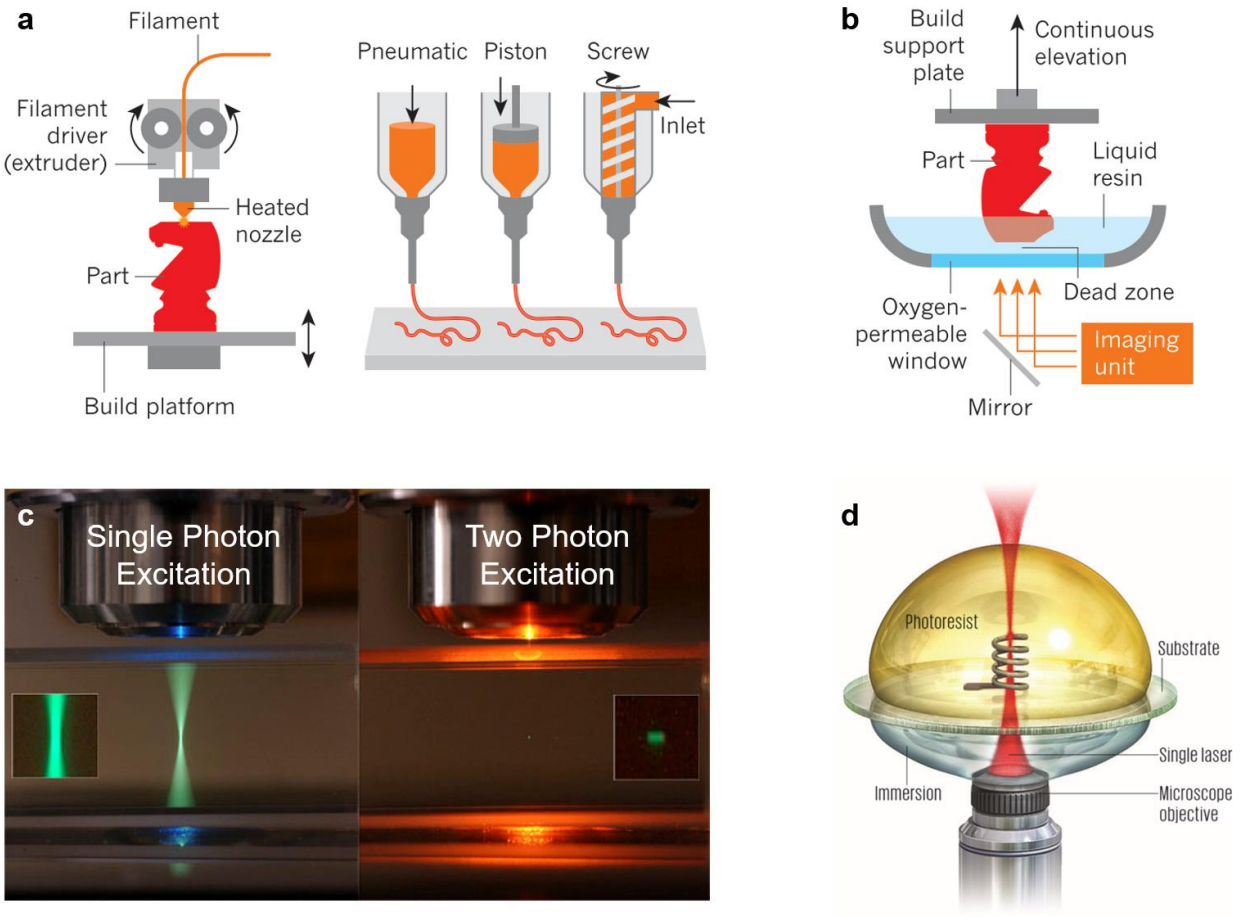

Figure 2.1 Various additive manufacturing methods for architected materials. (a) Extrusion-based 3D printing. Adapted from [63]. (b) Projection stereolithography. Adapted from [63]. (c) Comparison between single photon and two photon excitation. Adapted from [64]. (d) Two-photon lithography. Adapted from [65].

Material Extrusion

Extrusion-based 3D printing is the most versatile and intuitive concept to create structures in 3D. As illustrated in Fig. 2.1a [63], in this method, printing materials are extruded from a nozzle through heating and various ways of pressurizing, during which the nozzle is being translated in 3D relative to the sample stage. The advantage of extrusion-based 3D printing is their low cost, simple control, and the large variety of materials that can be printed including plastics, hydrogel [66], biological tissues [67], and composite materials with embedded metallic [68], magnetic [69], piezoelectric [70], and mechanical [71] fillers. Special techniques can also be used to align these fillers in certain directions to tailor the properties of the composite architected materials [69,71]. The feature size of the printed structure is directly related to the nozzle size of the print head and limited by the viscoelastic properties of the printed material during extrusion so a higher resolution generally leads to a significantly lower printing speed.

Projection stereolithography

Stereolithography uses photo-polymerization chemistry to print 3D objects by cross-linking polymers inside a liquid photoresist vat in a layer-by-layer fashion. The method itself dates back to the 1970s, but significant development has been made in recent years by combining stereolithography with a Digital Light Processing (DLP) unit commonly used in digital projectors to cross-link the whole lateral layer into programmed patterns at once (Fig. 2.1b [63]). Projection stereolithography substantially improves the printing speed by decoupling the lateral resolution with the lateral printing size, although the sample height is still limited by the z-layer spacing and the vertical motion of the sample stage. The lateral printing resolution of a minimum of a few microns [72] is a combined result of the DLP pixel size, magnifying or reducing optics, and the spatial energy confinement of the polymerization chemistry. A critical improvement has been the use of an oxygen permeable window to define a “dead zone” (persistent liquid interface) where photo-polymerization is inhibited between the window and the polymerized part, which allows for continuous writing in the z-direction instead of discrete steps [73]. This new method not only further improves the printing speed, but also significantly increases the surface smoothness of the printed object. However, due to the nature of the well-controlled photo-polymerization chemistry, the printed materials are predominantly polymer except for the recent development of hydrogel-based stereolithography, which is ideal for biological applications [74,75].

Two-photon lithography

Two-photon lithography utilizes the two-photon excitation process to crosslink photoresists sensitive to light with a wavelength of λ via a focused laser that are 2λ in wavelength. Such a non-linear excitation process requires the coincidence of two photons reaching the same crosslinking site so that there is enough energy to induce polymerization. This is a probabilistically rare event with a concentrated energy distribution in a very small focus point in the 3D space, i.e., the so-called voxel on the order of 100 nm as shown in Fig. 2.1c. By moving the voxel with respect to the sample stage, 3D structures with very high spatial resolution can be fabricated (Fig. 2.1d [65]). However, the two-photon excitation process is so rare that it requires a high energy laser to increase the rate of the probabilistic crosslinking events. In practice, in order to maintain a reasonable average laser power to avoid excessive heating, an expensive, high-frequency laser of femtosecond pulses is needed. In this thesis, all architected material samples are fabricated using two-photon lithography for the superior spatial resolution of ~500 nm and the precise geometric control. However, this method suffers from the key drawback of the extremely slow printing speed, which critically limits the total size of fabricated architectures. The printed material is almost exclusively polymer-based.

2.3 Post-processing Methods to Define Functionality

Due to the serious challenges of 3D printing architectures out of monolithic, high-quality non-polymer materials (e.g., metal, ceramic, and semiconductor), we propose a series of post-processing treatments to modify the chemical composition of polymer scaffolds as a practical alternative. In this section, we survey the advantages and disadvantages of various post-processing methods that retroactively modify the chemical composition and define the functionality of architected materials.

Physical Vapor Deposition

Physical vapor deposition (PVD) is a series of vacuum deposition methods that physically convert materials from a condensed phase to a vapor phase and then back to a condensed phase in the form of a layer of thin film coating. Sputtering and evaporation are the two most common PVD techniques that use ionized plasma and heat, respectively, to transfer materials from a target to the sample under high vacuum. The PVD methods have the benefit of working with a large variety of materials (e.g., metal, ceramic, semiconductor, organic, etc.) due to their purely physical deposition mechanisms. A sequence of depositions can be made using different targets on the same sample without transferring

between vacuum chambers, and multiple materials can be co-deposited at the same time for alloying or doping. Even though the PVD equipment is expensive, PVD is widely used in the semiconductor industry so the infrastructure is readily available in university cleanrooms and commercial foundries. The biggest drawback of using PVD to coat architected materials is that it is a "line-of-sight" deposition method so it is impossible to conformally coat complex 3D structures due to the shadowing effect. Sputtering has a relatively better step coverage, and increasing the deposition pressure slightly and rotating and tilting the sample stage during deposition could further improve the coverage for 3D structures, especially for applications that just need a layer of metal for conductivity. However, it is impossible to achieve conformal coating for 3D architectures via PVD, and the coverage for the inside of high relative density architected materials is particularly poor.

Chemical Vapor Deposition

Chemical vapor deposition (CVD) is another class of vacuum deposition techniques that use heat and/or plasma to chemically decompose precursor gases to produce high-quality solid films. A large number of chemistries are widely used in the semiconductor industry especially for silicon-based materials such as crystalline or amorphous Si, silicon dioxide, and silicon nitride. Depending on the reactor design (control of gas flow, temperature and concentration gradient, pressure, etc.), CVD-coated films can be very conformal for planar substrates and have reasonable coverage for complex 3D structures, which is limited by the transport kinetics and the decomposition mechanisms of the precursor gases. Generally speaking, the closer to the outside of an architected sample, the higher the precursor concentration is and the thicker the deposited film is.

Atomic Layer Deposition

Atomic Layer Deposition (ALD) is essentially CVD processes that are broken down into two self-limiting half reactions. During each half reaction A (B), precursor 1 (2) is introduced into the chamber and an atomically thin layer of self-terminating compound A* (B*) is conformally coated throughout arbitrarily porous 3D structures. Any coated surface is passivated and additional layers of the same compound cannot be deposited on top of it. After all surface area is saturated, the precursor gas is switched to the next half reaction as the cycling continues. Due to this unique mechanism, ALD could achieve unparalleled conformal, pinhole-free coverage with uniform thickness on complex nano-architectures [10,14,20,76]. The atomic level thickness control makes

ALD widely adopted in microprocessor fabrication for gate oxides and metal barriers. Ceramics is the most validated class of materials with well-developed ALD recipes, and emerging ALD methods for metals, polymers, and complex inorganic materials such as the solid electrolyte LiPON [77–79] are reported regularly. However, the ALD process is extremely slow at a rate of ~100 nm/hr in order to control the saturation of each half reaction cycle, and the ALD-deposited materials might contain chemical impurities. Overall, ALD is the most ideal method to functionalize complex architected materials through conformal deposition, but it only works with certain reaction chemistries for nanoscale thin films.

Electrodeposition

Electrodeposition or electroplating is the process of using an electrical current to reduce dissolved metal cations to form a thin metal coating on an electrode. This method is widely used in the industry of electronics, automobile, manufacturing and decoration due to its low cost, good scalability, and high degree of control through voltage, current and pulsing. One critical limitation for its application in architected materials is that it requires a conductive surface for the reduction reaction to occur. Fortunately, a variant of electrodeposition called electroless deposition could take advantage of a catalytic surface to induce the reduction of metal ions. Through surface treatment of architected polymer scaffold, electroless deposition of Ni is commonly used to create metallic architected materials [21,72]. Alternatively, a seed layer of metal can also be sputtered on the surface of architected materials before further electrodeposition of a thicker metal layer [80]. Electrochemical deposition could also coat non-metal materials such as ceramics [81–83] and polymers [84–86]. Overall, electrodeposition is the most scalable method to deposit various materials on an architected scaffold, but the academic community is less knowledgeable than the industry in terms of know-hows to achieve a high degree of control and uniformity through specific additives and protocols.

Template Inversion

The above-mentioned methods focus on depositing another layer of functional material on a polymer scaffold as a composite structure, while the polymer scaffold could also be subsequently removed to create a hollow, monolithic structure. Another approach is to 3D print the inverse space of the desired architecture by using a positive-tone photoresist or by directly writing the inverse template, and then infiltrate the pore space and channels with another material. The inverse template will eventually be

removed through selective chemical etching or other processes. This template inversion method has the unique advantage of creating solid, monolithic architected materials made out of metal, semiconductor, or ceramics [18,87]. However, the infiltration and selective etching process is hard to control and only works for a limited number of material systems.

Sintering and Pyrolysis

Finally, a different approach is to change the composition of as-fabricated architected materials through heat treatments such as sintering and pyrolysis. During sintering of structures made out of composite materials, the polymer binder could be reduced or removed, and the ceramic or metal particle fillers could coalesce to increase the structural stability and improve the conductivity [88,89]. During pyrolysis, the constituent material of the 3D architecture undergoes chemical decomposition and is converted into a different material with drastically different properties. For example, metal [90], ceramics [91], and glassy carbon [9] have all been converted from polymer architectures. Meanwhile, the structures also experience significant shrinkage due to pyrolysis, which could lead to finer feature sizes as well as mechanical distortions. Overall, sintering and pyrolysis through heat treatment under various environments are relatively easy to implement, but the challenge lies in the development of photoresists that can be converted into other materials after polymerization.

2.4 Architected Material Design for Electrochemical Systems

In this section, we use electrochemical systems as an example for functional architected material design. As mentioned in the first chapter, designing an electrochemical cell for specific applications requires multi-faceted consideration of oftentimes coupled factors like ion transport inside the electrolyte, electron transport inside both electrodes, electrode surface area, chemical reversibility, parasitic side reactions, and the conductivity and mechanical stability of the reaction products on both electrodes. Here we illustrate the use of rational architected material design to address some of the challenges for the electrodes in electrochemical cells. Similar design thinking and the toolset of various additive manufacturing and post-processing techniques can be applied to architected material design for different applications.

First, we consider an individual beam or building element for non-beam-based architectures. For a polymer scaffold, a conductive layer needs to be coated to facilitate electron transport before coating

the electrochemically active material, if the latter is not conductive by itself. For a metal conductive layer, a thin film of tens of nanometers would be sufficient. For carbon-based electrodes that are intrinsically conductive (for example, synthesized by pyrolysis), extra conductive layer is not necessary. The thickness of the active material layer is determined from the tradeoff between reaction kinetics and surface-to-volume ratio. For a kinetically sluggish reaction, increasing the surface area would increase the reaction rate, but a larger surface area also leads to more parasitic reactions (such as solid-electrolyte-interphase formation) that irreversibly consume the active material. For certain electrode materials, thickness also influences their mechanical stability during cycling. For example, experiments and theories suggest a critical size of ~100-300 nm, below which crystalline Si nanostructures can be cycled without fracturing [92–96]. For certain electrochemical cells such as fuel cells or supercapacitors, the electrode itself doesn't participate in the electrochemical reactions other than conducting electrons. In these cases, it might be beneficial to have a nanoporous surface morphology on the beams to significantly enhance the surface area, but clogging could be a potential issue.

Furthermore, on the lattice unit cell level, the porosity and the structural stability are important. For certain electrode materials, the electrochemical reactions would induce significant volume expansion up to 300% [97] so necessary porosity can be designed in the architecture to accommodate such volume change. The periodic porosity and the low tortuosity of the architecture also provide the pathways for ion transport inside the electrolyte. For certain applications, the mechanical stiffness, strength, and stability could be important, and various lattice geometries can be designed to meet specific demands. On the other hand, the pore space in architected materials inevitably reduce the volumetric loading of the active material. Therefore, the thickness of the active material, the size of the unit cell, and the porosity of the geometry should be carefully designed to optimize the trade-off between reaction kinetics and mechanical stability vs. active material loading and the amount of inactive components (e.g., polymer scaffold).

For device integration or fabrication of individual samples, it is important to consider more practical factors like active material loading per footprint area, packaging method and materials, as well as the time and uniformity for various fabrication techniques. 3D-architected electrodes have the unique advantage of efficient electron and ion transport through the conductive scaffold and the low-tortuosity ion diffusion pathways. Therefore, increasing the areal loading of architected electrodes

by integrating more layers in the z-direction compromises transport kinetics significantly less than increasing the thickness of planar or slurry-based electrodes would. Finally, based on the architecture and composition design, appropriate fabrication methods would be assessed. The active material thickness and the unit cell size would determine the 3D printing method with sufficient spatial resolution such that the polymer scaffold constitutes a small portion of the total mass. For the conductive layer, non-conformal sputtering deposition of metal would be accepted for structures with low relative densities, while eletroless metal plating might be required for denser and taller architectures. Even though ALD provides the most conformal coverage, the slow deposition rate makes it unfeasible for any material layer more than a few hundred nanometer thick. Therefore, ALD is ideal for depositing an ultrathin layer of solid electrolyte that are pinhole-free to prevent short-circuiting while maintaining a short solid-state ion diffusion distance. For the active material layer, CVD and electrodeposition provide a good combination of deposition rate and uniform coverage for films of a few micron in thickness. Based on the limitation of these fabrication techniques, it is normally necessary to re-evaluate the architecture design and make modification due to practical concerns.

In this section, we put forward a list of factors for consideration when designing functional architected materials in the context of electrochemical systems. In the next two chapters, we will demonstrate such design principles with specific examples, namely 3D-architected electrodes for Li-ion batteries and electrochemically reconfigurable architected materials. As research efforts continue, rationally designed functional architected materials could improve and bring new perspectives to a wide range of applications.

Chapter 3

3D-ARCHITECTED ELECTRODES FOR LI-ION BATTERIES

3.1 Redesigning the Battery Architecture

Batteries are electrochemical energy storage systems that not only enable smaller electronics, but also help to create a sustainable future by powering electric vehicles and balancing intermittent renewable energy sources. Li-ion batteries with intercalation electrodes (i.e., graphite anodes and transition metal oxide cathodes) and organic liquid electrolytes have been the main driving force for the energy storage revolution, but they are unable to meet our increasing societal demands. Today's smartphone batteries can barely last through the day and occasionally burst into flames. After decades of intensive research and development, the energy density of state-of-the-art Li-ion batteries has been gradually improved to around 200 Wh/kg, less than half of the theoretical values [98]. Continued yet incremental improvement largely relies on the industry's efforts in perfecting the slurry-based roll-to-roll fabrication method, reducing the ratio of inactive components, and gradually increasing the nickel content in cathode materials. The current Li-ion material platform is not expected to achieve the Department of Energy's electric vehicle battery goal [99] of a volumetric energy density of 750 Wh/L, a gravimetric energy density of 350 Wh/kg, and a power density of 700 W/kg.

On the material level, state-of-the-art electrode materials for both the anode and the cathode have the intercalation-based Li storage mechanism. Atomic Li is inserted into and extracted from the interstitial sites of the host lattice repeatedly during cycling, without disturbing the crystal structure of the electrode active materials. Even though this mechanism provides superior reversibility at satisfactory energy density for Li-ion batteries, it requires at least a couple of host atoms to create one interstitial site for a Li atom (e.g., six carbon atoms for one Li atom in graphite anodes), which fundamentally limits the specific capacity of the electrode materials. To break free from this critical constraint, alloying or conversion based electrode materials such as silicon, lithium metal, and sulfur are being actively investigated by both the academic community and the industry, but large-scale application is still immature. One of the critical challenges is that a large atomic ratio of Li to the

host material (e.g., each Si atom could alloy with up to four Li atoms) not only gives rise to higher Li storage capacity, but also induces significant volume expansion: 300% for Si [100], 80% for S [101], and theoretically an infinite amount for Li metal if no excess Li is used [102]. Such volume expansion and contraction during cycling lead to serious mechanical problems such as fracture and failure, pulverization of active material particles, interfacial delamination, and loss of electrical contact, which all diminish the capacity retention of the cells.

Reducing the dimension of the active materials from micron-sized particles to nanoscale building blocks such as nanoparticles and nanowires has been shown to be an effective method to improve the mechanical stability due to size-induced ductility, built-in free space for expansion, and short diffusion length for a more homogenous swelling [100,103–107]. However, the traditional slurry-based electrode assembly method does not translate the mechanical robustness of these nanoscale elements into superior electrode performance in a practical or commercially applicable way. Such electrodes are made from a slurry mixture of active material particles, conductive additives, and polymer binders, which results in a convoluted internal structure and fundamental performance limitations [108]. As shown in Fig. 3.1a, nano-sizing active material particles means packing orders of magnitude more smaller particles which generally leads to (1) high structural tortuosity and poor electron and ion conductivities, (2) large surface-to-volume ratio with more irreversible solid-electrolyte interphase (SEI) formation, and (3) electrode-wide mechanical degradation. As a result, despite the great promises of nanotechnology, electrodes based on nanomaterials assembled by a slurry-based method are detrimentally limited by the trade-off between low active material loading (i.e., energy density) and poor transport kinetics (i.e., power performance).

A drastically different electrode architecture based on interconnected conductive scaffolds coated with active materials with controlled structure provides an attractive alternative for next generation batteries as illustrated in Fig. 3.1b. Essentially, such 3D-architected electrodes resemble a host structure on the mesoscale that can be more controllably modified based on different chemistries than the host crystal structures for intercalation on the atomic level. While providing efficient conductive pathways for both electrons and Li ions, the electrode architecture can be optimized to maintain the mechanical robustness at the small scale and to afford enough, but not excessive free space (i.e., porosity) for volume expansion. Pioneering works have explored the stochastic foams [109], self-assembled templates [105,110–113], and holographic patterning [114] to define

the electrode architecture. In this chapter, we investigate the potential of using high-resolution additive manufacturing and post-processing depositions to achieve precise structural control for rational electrode architecture design.

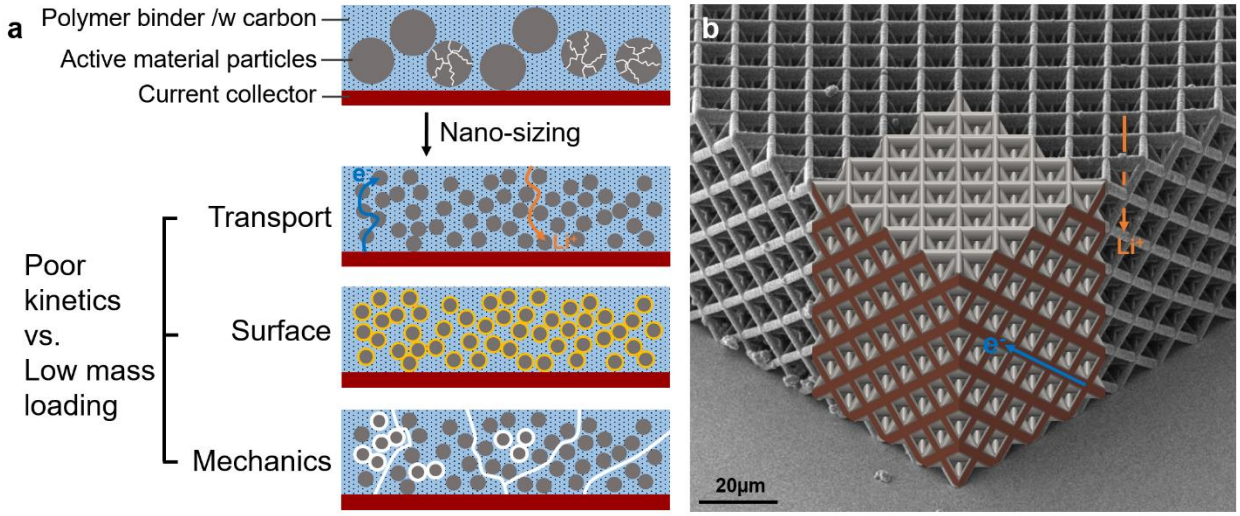

Figure 3.1 Comparison between (a) slurry-based electrodes and (b) 3D-architected electrodes enabled by additive manufacturing.

3.2 Mechanical Challenges due to Volume Expansion in Si-based Anodes

Si anodes for Li-ion batteries have a high theoretical capacity of 3600 mAh/g, an 10X enhancement compared with intercalation-type graphite anodes [100]. The alloying nature of Li insertion in Si allows each Si atom to accommodate up to four Li atoms, but it also causes up to ~300% Si volume expansion and contraction during lithiation and delithiation [100]. These large volume changes induce significant mechanical stresses that make bulk Si crack and pulverize into inactive powders. Fracturing events also expose new Si surfaces to the electrolyte forming more solid-electrolyte interphase (SEI), which reduces the active electrode material that can be cycled reversibly [103]. Nanostructured anodes such as Si nanowires and nanoparticles have demonstrated success in alleviating mechanical degradation in cell cycling tests [100,103–105] and during *in situ* transmission electron microscope (TEM) observations [106,107]. The improved mechanical stability stems from the availability of pore space for Si expansion, a reduced diffusion length that lowers inhomogeneous swelling, and increased ductility in nanoscale, lithiated Si [95,103,115–117]. Experiments and theories suggest a critical size of ~100-300 nm, below which crystalline Si

nanostructures can be cycled without fracturing [92–96]. Amorphous Si (a-Si) is more mechanically robust because of its microstructural isotropy; cylindrical, ~2 μm-diameter a-Si pillars have been lithiated and delithiated with no cohesive fracture [118]. However, when clusters of nanoscale Si are assembled together in a practical electrode, their mechanical and chemical interactions with the surroundings are much more complicated and hardly captured by *in situ* TEM observations of individual nanoparticle or nanowire. Mechanical clamping of Si pillars could alter the reaction kinetics so that preferential lithiation occurs at free surfaces instead of along the thermodynamically favored {110} planes [119]. The slurry method of mixing anode material particles with polymer binder and carbon additives is suitable for intercalation materials with minimal volume expansion; it does not provide efficient and reliable assembly of the nanoscale Si building blocks, in which cycling-induced expansion and contraction lead to an eventual loss of contact with binder and carbon additives [120–122].

The development of three-dimensional, nano-architected electrodes is a promising approach to proliferate the mechanical robustness of nanoscale Si onto device-scale electrodes. Zhang et al. demonstrated that electroplated inverse opal Ni scaffolds coated with 50nm of Si achieved good mechanical stability and electrochemical cyclability for over 100 cycles [105]. The periodic pore space enabled such nano-architected electrodes to accommodate large Si volume expansion, but the active material loading was low and the electrode structure was constrained to the inverse opal geometry. Further investigations are necessary to fully understand the structure and stress evolution during lithiation and to rationally design nano-architected electrodes that are mechanically robust and kinetically agile with higher active material loading.

3.3 Fabrication of Cu-Si Core-shell Nanolattices as Battery Electrodes

In this chapter, we report the fabrication process to create 3D-architected Cu-Si core-shell nanolattices via two-photon lithography [87], which offers precise control over geometry, feature size, porosity, and electrode chemical composition. We demonstrate the structural evolution of the nanolattices during lithiation and delithiation by performing electrochemical cycling inside a scanning electron microscope (SEM). We observed no visible cracks in the lattice beams during the first lithiation and delithiation cycle using solid Li_2O electrolyte, and conducted electrochemical characterization of these electrodes using an ionic liquid electrolyte. Finally, a

coupled deformation-diffusion model was employed to quantitatively capture the stress evolution within the Si shell and to provide useful guidelines for improving electrode design. The high spatial resolution and wide imaging range of SEM make it ideal for observation of the morphological evolution of architected electrodes at multiple length scales–from single lattice beam to one unit cell and the entire nanolattice. Existing *in situ* SEM studies on Si electrodes focus either on individual Si nanowires or nanopillars [109,123,124], where the mechanical and chemical interactions with polymer binder, carbon additives and neighboring Si nano-elements are absent, or on the edge of a planar Si electrode [125–127], which reveals limited information of structural changes inside the electrode. *In situ* SEM observation of Cu-Si nanolattices during lithiation and delithiation at the architecture level provides new insights into binder-free, nano-architected electrodes' ability to proliferate the mechanical robustness of nanoscale Si onto the entire electrode with little unaccounted interactions with the surrounding environment. Such direct observation, combined with finite element modeling of the stress evolution, provides a more complete understanding of the mechanical advantages of nano-architected electrodes.

The fabrication process along with SEM and TEM characterization of the Cu-Si core-shell nanolattices is summarized in Fig. 3.2. First, computer-designed octet lattice was directly written in the positive-tone photoresist on an Au-coated glass substrate via two-photon lithography. The patterned photoresist was used as a 3D template for galvanostatic Cu electroplating. Upon removal of the remaining photoresist, the free-standing Cu lattice scaffold was previously reported to have very high yield strength upon uniaxial compression [18]. Finally, a-Si was deposited by plasma-enhanced chemical vapor deposition (PECVD) with ~250 nm a-Si coating on the Cu lattices and ~750 nm on the flat substrate. A SEM image of a representative Cu-Si core-shell nanolattice with 8 μm unit cell size is shown in Fig. 1b. The Cu lattice beams have an approximately elliptical cross-section with ~0.9 μm minor axis and ~2 μm major axis (Fig. 3.2c). The a-Si shell was investigated using focus ion beam (FIB) and was found to be ~300-500 nm on the surface beams and ~150-250 nm on the inner beams for a 25 μm-sized lattice (Fig. 3.2d). For an octet lattice with an averaged 250 nm Si coating, ~24% of unit cell volume is occupied by Cu and ~19% by Si, which leaves sufficient space for Si to expand by 300% during lithiation. The volumetric Si loading in these samples is ~0.43 g/cm^3, and the areal Si loading is ~0.85 mg/cm^2. The microstructure of Cu, Si and Cu-Si interface was investigated via TEM (Fig. 3.2e). Selected-area diffraction pattern showed that

the Cu region is polycrystalline, and the Si region is amorphous. TEM analysis revealed the presence of a few, 20-30 nm-sized voids located at the Cu-Si interface (Fig. 3.2f), which would likely serve as sites for crack-initiation if delamination were to occur. We measured the root-mean-square roughness of Cu surface before Si deposition to be 22 nm using atomic force microscopy, which reflects the roughness of the Cu-Si interface.

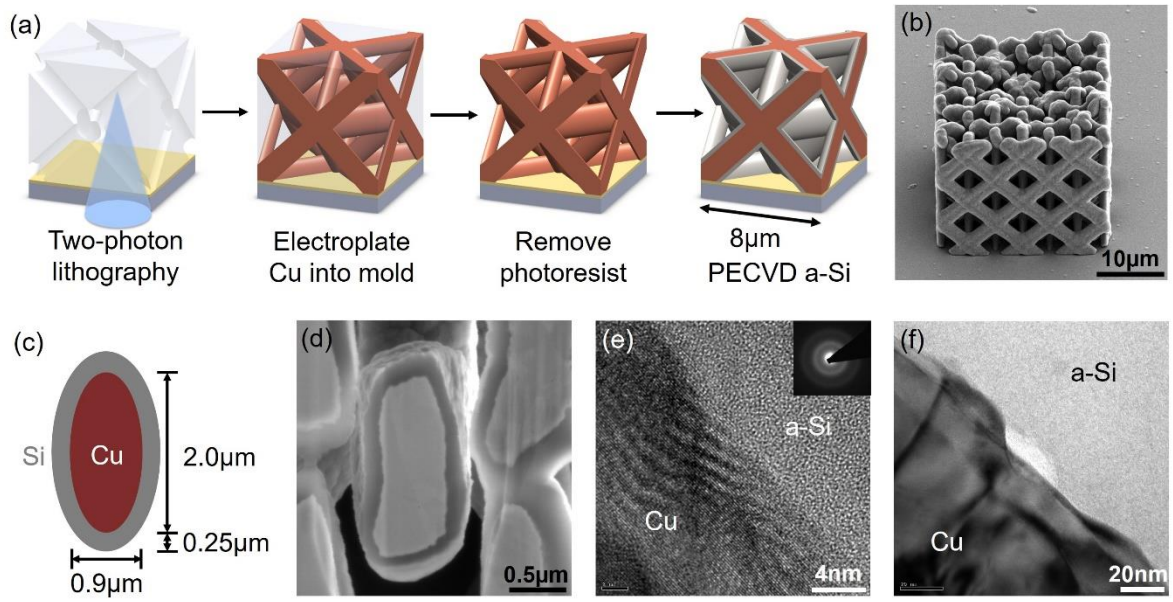

Figure 3.2 (a) Illustration of the fabrication process and (b) SEM image of a Cu-Si nanolattice. (c) Illustration and (d) SEM image of the elliptical cross-section of a Cu-Si core-shell nanolattice beam. (e) High resolution TEM image of the Cu-Si interface, which shows fringes caused by sample bending or thickness variation in the crystalline Cu phase and a smooth interface between Cu and a-Si. Inset: a selected-area electron diffraction pattern with concentric rings characteristic of amorphous microstructure of the a-Si shell. (f) TEM image of a void at the Cu-Si interface.

The detailed fabrication process of Cu-Si core-shell nanolattices is provided below. First, a positive photoresist (Microchem AZ4620) was spin-coated onto a 15 nm Au-coated glass cover slip and cured at 110°C for 3 min. Two-photon lithography (Nanoscribe, GmbH) was used to write the octet lattice structure designed in MATLAB using laser powers in a range of 0.8-1.2 mW and a writing speed of 10 μm/s. The patterned photoresist was developed in a solution of AZ400K: DI water at 1: 4 ratio. Using the remaining photoresist matrix as a 3D template, galvanostatic Cu electrodeposition was conducted in a three-electrode setup with a Cu counter electrode and Ag/AgCl reference electrode. The electroplating bath was composed of 100 g/l $CuSO_4 \cdot 5H_2O$, 200 g/l H_2SO_4, and

commercial Cu electroplating additives (5 ml/l 205-M, 1 ml/l 205KA, and 1 ml/l 205KR, Electrochemical Products, Inc.). After electroplating, the photoresist matrix was removed by soaking in 1-methyl-2-pyrrolidone, leaving the freestanding Cu lattices on a Au thin film on a glass substrate. The Cu lattices had a ~20% variation in beam diameter for the range of lithography laser power used in this work. A layer of a-Si was then deposited on the Cu lattice scaffold by PECVD at 200°C with 5% silane precursor gas at 250 sccm flow rate and 800 mTorr pressure for 30 min.

3.4 *In situ* Observation of Electrode Deformation in a Scanning Electron Microscope

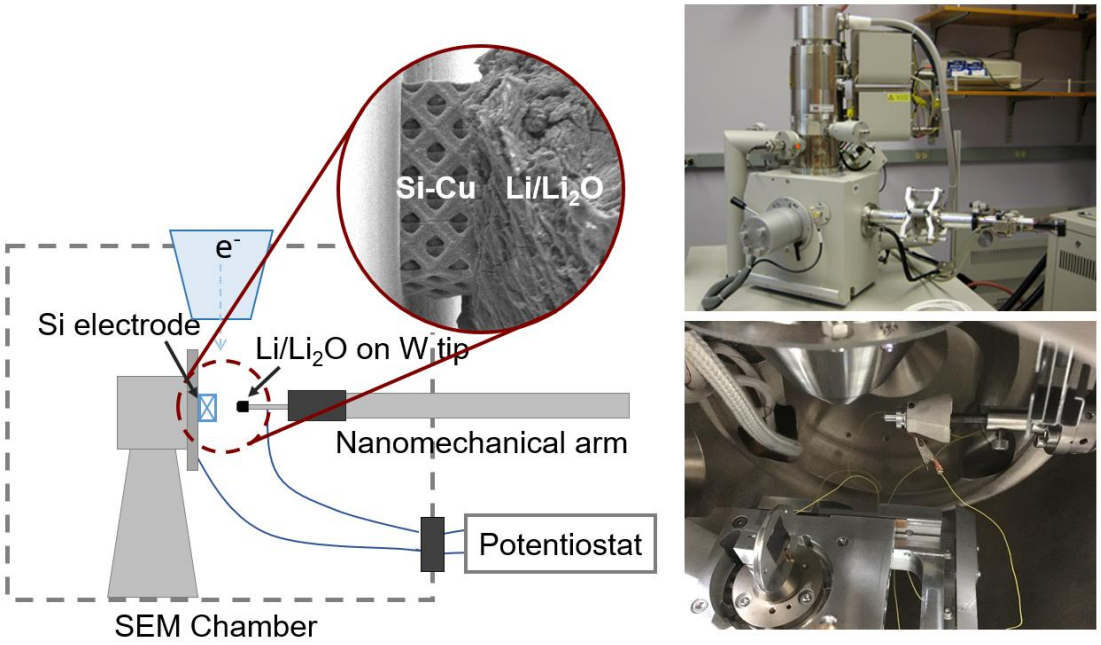

Figure 3.3 Schematic and photos of the *in situ* SEM lithiation setup.

In situ lithiation and delithiation of the Cu-Si nanolattices was conducted using a custom-made electrochemical setup inside an SEM nanomechanical instrument (Quanta 200 SEM, FEI and InSEM, Nanomechanics, Inc.) (Fig. 3.3). The electrochemical cell of a Cu-Si nanolattice and a Li counter electrode was connected to an external potentiostat (SP 200, Bio-Logic Science Instruments). The glass substrate supporting the Cu-Si core-shell nanolattices was held vertically on the side of a SEM sample holder. A ~500 µm–diameter piece of Li was attached to a W tip inside of a glovebox, transferred to the SEM in an Ar-filled container and then quickly mounted onto the nanomechanical arm inside the SEM chamber with less than 10 s exposure in air. The negative electrode of the potentiostat was connected to the Li electrode via the W tip, and the

positive electrode of the potentiostat was connected to the Au film on the sample substrate. We aligned the Li electrode to be positioned directly above the Cu-Si nanolattice in the SEM image. The Li electrode can be lowered to form a half-cell, in which either solid Li_2O or 10 wt% LiTFSI in P_{14}TFSI ionic liquid was used as the electrolyte. The lithiation rate C_{rate} is the rate of discharge defined by the multiplicative inverse of the number of hours it takes to fully discharge an electrochemical cell based on the theoretical capacity of Si (i.e. 0.25C indicates a full discharge in 4 hr).

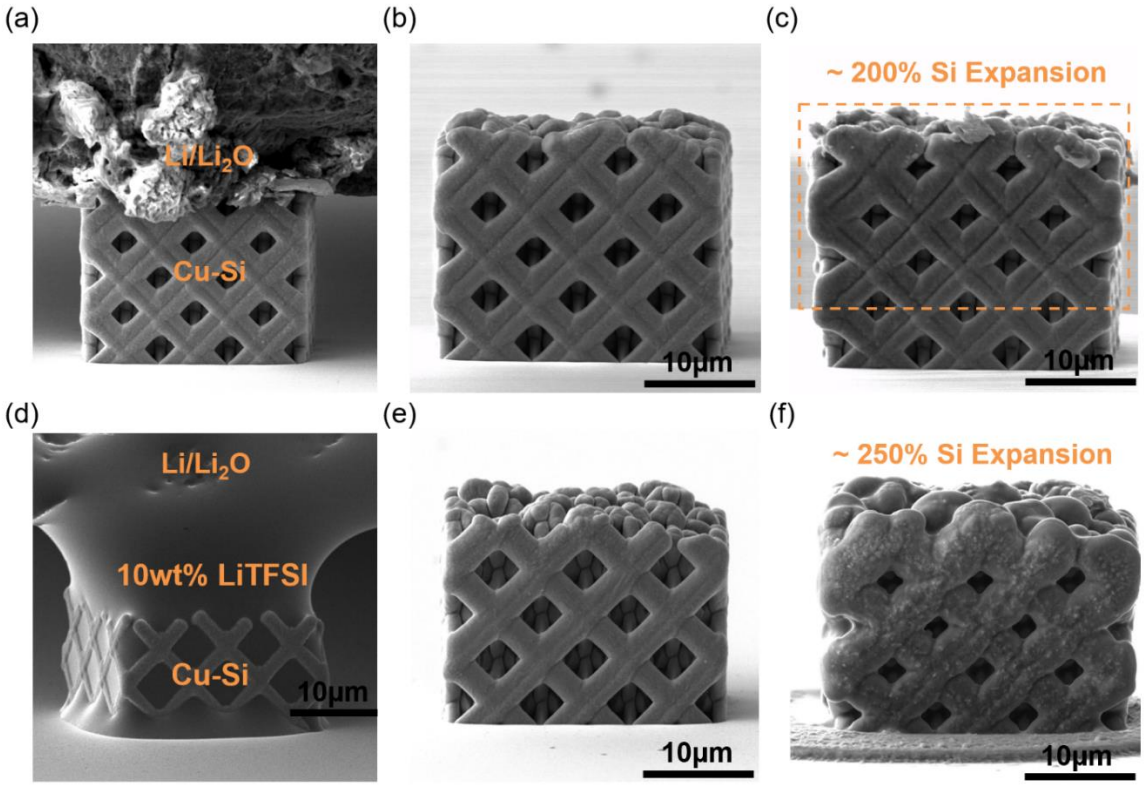

Figure 3.4 SEM images of a Cu-Si nanolattice (a) during, (b) before and (c) after lithiation with solid Li_2O electrolyte. SEM images of a Cu-Si nanolattice (d) in contact with ionic liquid electrolyte before full immersion, (e) before being wetted by ionic liquid, and (f) after lithiation with ionic liquid removed by activated carbon.

We first used the native Li_2O layer formed on Li during transfer as a solid electrolyte (Fig. 3.4a). SEM imaging was used to directly observe the volume expansion of Cu-Si nanolattices during lithiation under -2 V bias versus Li/Li^+. The lithiation video (Supplementary Video 1) shows a lithiation reaction front progressed from top to bottom of the nanolattice, as indicated by change

in SEM contrast and radial expansion of lattice beams, while beams behind the reaction front continued to expand and reached higher states of lithiation. Snapshots of the *in situ* lithiation video is shown in Fig. 3.5. No visible cracks were observed in SEM in seven samples at a lithiation rate of ~0.25C-1C under the applied voltage. The Si shell of the core-shell nanolattices expanded by up to ~214% during lithiation. Delithiation was conducted by applying a 2 V bias versus Li/Li^+, and the lithiated Cu-Si nanolattice beams contracted relatively homogenously, without an obvious reaction front (Supplementary Video 2). The observed volumetric changes imply that not all of the inserted Li was extracted from the Li-Si alloy. It was challenging to maintain consistent contact between the solid electrolyte and the nanolattice because the Li_2O layer was not conformal, the Li piece was porous and soft, and the nanolattice was changing in volume. In some experiments, newly exposed Li was in direct contact with Si as the two electrodes were pushed against each other; sometimes the top of the nanolattice was only partially in contact with the Li electrode. These problems were particularly significant for the delithiation experiments because chemical lithiation and electrochemical delithiation can be in competition and the contact between the nanolattice and the solid electrolyte was easily lost when the beams contracted. These issues prohibited extended cycling of the half-cell.

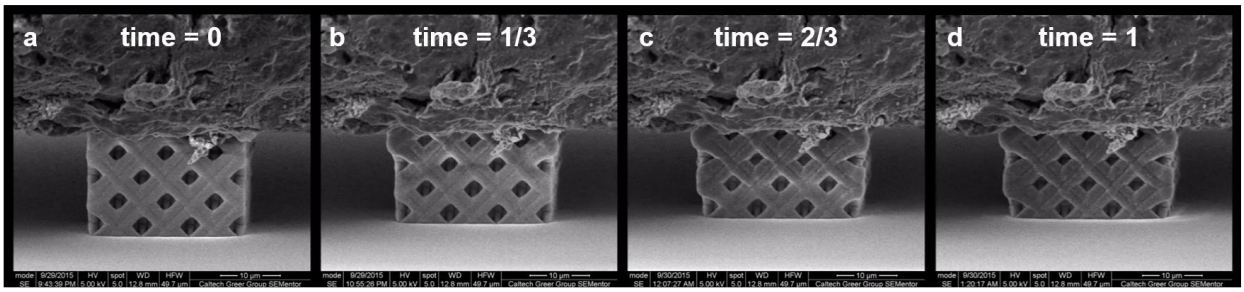

Figure 3.5 Snapshots of *in situ* SEM video of lithiation of Cu-Si core-shell nanolattices

To more faithfully mimic practical batteries in which electrodes are immersed in a liquid electrolyte, we conducted lithiation experiments using an ionic liquid electrolyte (10 wt% LiTFSI in P_{14}TFSI ionic liquid [106]), which can withstand the SEM vacuum environment. The liquid electrolyte entered the pores in the Cu-Si nanolattices, which allowed Li to diffuse from the exterior Si shell surface towards the Cu-Si interface radially for all beams simultaneously. The Li electrode was first dipped in an ionic liquid droplet on the sample holder, and then slowly brought into contact with the nanolattice. The ionic liquid was wicked into the pores of the nanolattice by

capillary forces (Fig. 3.4d). Via the combined motion of the sample stage and the nanomechanical arm, the suspended ionic liquid droplet was fine tuned to immerse the Cu-Si nanolattice structure with minimal contact between the substrate and the ionic liquid droplet in order to reduce the influence of Si thin film surrounding the nanolattice on measured electrochemical behavior. The area of the Si thin film on the substrate in contact with the ionic liquid also participated in the lithiation reaction. We obtained a cyclic voltammogram at a 2 mV/s scanning rate; its shape qualitatively agrees with that of typical a-Si lithiation [100,128] except that the anodic peaks are shifted towards higher potentials, possibly due to the internal resistance of the *in situ* setup and the high scanning rate (Fig. 3.6a). The Cu-Si nanolattice was discharged galvanostatically at 10 nA (~0.25C), and the first discharge capacity was estimated to be ~3280 mAh/g normalized by Si mass, taking into consideration the contribution from the Si thin film on the substrate in contact with the ionic liquid (750 nm-thick Si thin film disk of 70 μm in diameter). Since volume changes of the fully immersed electrode cannot be directly observed, we briefly opened the SEM chamber (<5 s) and mounted a piece of activated carbon on the W tip to adsorb most of the electrolyte away from the nanolattice. Fig. 3.4f shows a lithiated nanolattice, which underwent a volume expansion of ~256% with no visible cracks in SEM. The nanolattice could not be delithiated because the Si film surrounding it and covered by the ionic liquid electrolyte tended to crack and delaminate from the substrate during the early stage of delithiation, which caused the nanolattice to be disconnected from the current collector. This is not surprising because the 750 nm-thick Si film is above the critical thickness reported for a-Si thin film electrodes [93,94,129].

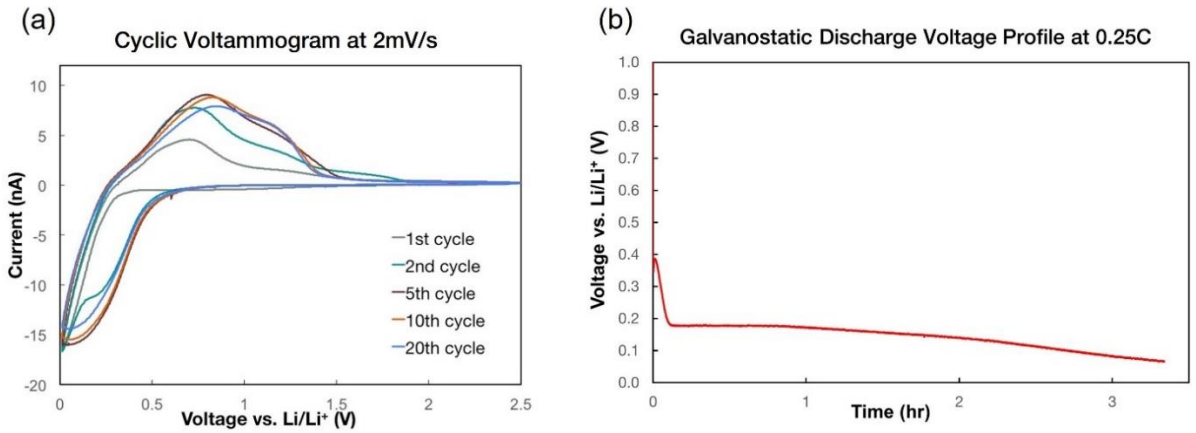

Figure 3.6 (a) Cyclic voltammogram for the *in situ* half-cell with the ionic liquid electrolyte at a voltage scanning rate of 2 mV/s. (b) Galvanostatic discharge voltage profile of the *in situ* half-cell with the ionic liquid electrolyte at a discharge rate of ~0.25C.

This *in situ* SEM setup for electrochemical reactions provides a unique opportunity to probe into the morphological evolution and mechanical dynamics inside batteries that were previously unattainable from *in situ* TEM experiments (which mostly provide atomic microstructure) and *ex situ* sample-scale characterizations. For example, we have extended the *in situ* SEM setup to analyze Li plating and stripping in a solid-state thin film battery through a LiPON solid electrolyte as shown in Fig. 3.7a-d [130]. Furthermore, the high spatial resolution and accurate manipulation allow us to individually study micron-sized electrode particles with solid and liquid electrolyte (Fig. 3.7e, f).

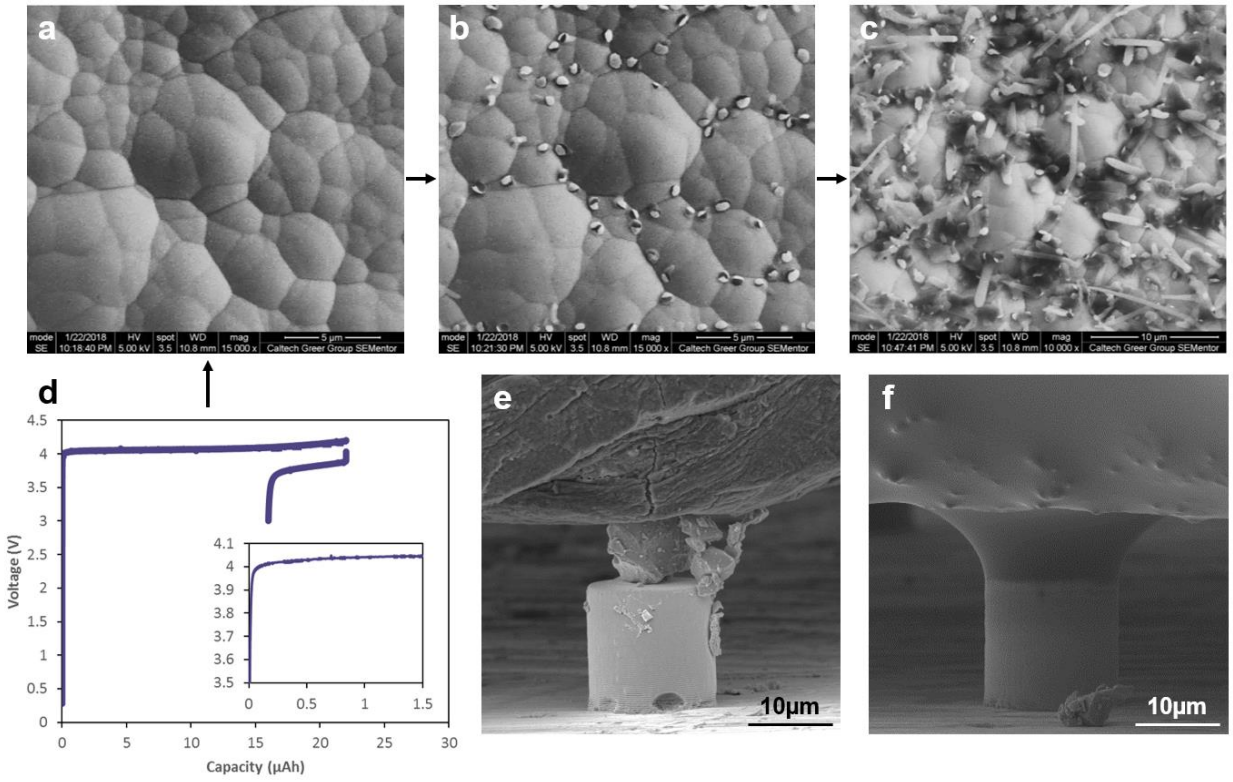

Figure 3.7 (a-c) *In situ* Li plating in a solid-state thin film battery through a LiPON solid electrolyte. (d) Charge and discharge voltage profile of Li plating and stripping in SEM corresponding to the *in situ* experiment in (a-c). (e, f) Single Si_xO particle lithiation with solid and liquid electrolyte in SEM with a 3D printed pedestal coated with Ni.

3.5 Finite Element Modeling of Lithiation-Induced Volume Expansion

To investigate the influence of the lattice architecture on the mechanical stability of the Cu-Si nanolattice electrodes, we applied the theory and numerical capability developed by Di Leo et al. [131] to model the a-Si shell lithiation and to examine the evolution of local stresses in Si and at the Cu-Si interface. This fully-coupled diffusion-deformation theory accounts for the transient diffusion

of Li, large elastic-plastic deformations, the effect of mechanical stress on the diffusion of Li, and Li concentration-dependent yield stress and elastic modulus. Material parameters in the theory were calibrated to match the experiments by Pharr et al. [132] and by Bucci et al. [129] on galvanostatic cycling of an a-Si thin-film anode deposited on a quartz substrate. The core-shell nanolattice beams were modeled as long bars immersed in a liquid electrolyte under plane strain conditions without accounting for the end effects of beam junctions. We prescribed a constant flux boundary condition that corresponds to a lithiation rate of 1C on the exterior Si surface, edge AE in Fig. 3.8a, unless otherwise stated. Simulations were run until an element of the mesh reached the maximum molar concentration of Li in the Li-Si alloy.

Finite element modeling provided the evolution of Li concentration, maximum principle stress, and equivalent plastic strain in the Si shell during lithiation (Supplementary Video 3). Simulation revealed that the maximum principal stress in Si is tensile near the Cu-Si interface and compressive near the exterior Si surface. The maximum principal stress in Si near the Cu-Si interface, as well as the normal and shear stresses at the Cu-Si interface, goes through a maximum during the early stage of lithiation and then decreases after yielding because the emergent plastic deformation facilitates relaxation of the built-up elastic stress. Fig. 3.8b displays the contours of the normalized concentration (top), the maximum principal stress (middle), and the equivalent tensile plastic strain (bottom) at three different times: t = 16 s, 67 s (maximum principal stress at maximum), and 2270 s. Fig. 3.8c, d plot the normal and shear stresses at the Cu-Si interface, as a function of the normalized distance along the interface at t = 16 s, 67 s (interfacial normal stress at maximum), 113 s (interfacial shear stress at maximum), and 2270 s. The stresses in Si and at the Cu-Si interface were non-uniform because of the elliptical shape of the beam cross-sections. Simulations revealed that the highest tensile stress in the Si shell during lithiation is 0.71 GPa. Assuming a pre-existing Si flaw size of the shell thickness and following the approach in [133,134], we estimated the critical stress for crack propagation in Si to be 1.35 GPa based on the analysis by Beuth [135], which is significantly higher than the calculated stress. Hence, we do not expect cohesive fracture to occur in the Si shell during lithiation; a more likely failure mode is interfacial delamination at the Cu-Si interface.

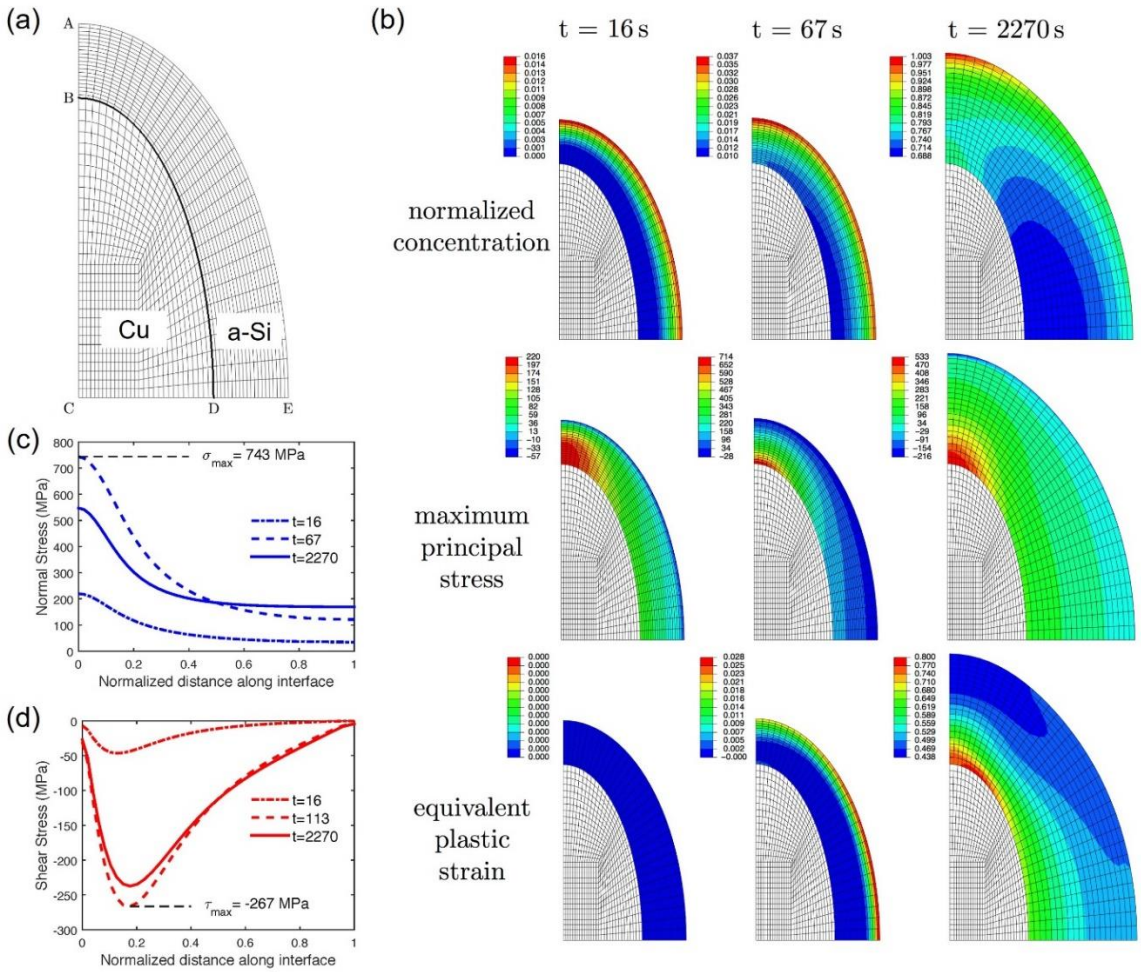

Figure 3.8 (a) Finite element mesh of a quarter of the Cu-Si beam cross-section. (b) Contours of the normalized Li concentration (top), maximum principal stress (middle), and equivalent plastic strain (bottom) of the a-Si shell during lithiation at three different times. Distribution profiles of (c) the interfacial normal stress and (d) the interfacial shear stress at the Cu-Si interface at three different times.

We adopted a simplified mixed-mode interfacial delamination model [136–140] to estimate the critical interfacial flaw size a_c, above which a pre-existing interfacial crack of length 2a would propagate under the simulated maximum interfacial stresses. A simple Griffith model was adopted to estimate the Cu-Si interfacial delamination condition under normal and shear stresses. Suppose an internal crack of length 2a pre-exists at the Cu-Si interface possibly due to Si deposition flaws, the energy release rate G is a function of mode I and mode II stress intensity factor

$$G = \frac{1}{E^*}(K_I^2 + K_{II}^2)$$

where the effective elastic modulus $E^* = 2\left(\frac{1}{\bar{E}_{Cu}} + \frac{1}{\bar{E}_{Si}}\right)^{-1}$. As previously studied by Suo and Hutchinson [136,137], for most bi-layer materials with reasonably small modulus mismatch, the complex stress intensity factor can be approximated as

$$K_I + iK_{II} = (\sigma_{22} + i\sigma_{12})\sqrt{2\pi a}$$

The fracture energy of the Cu-Si interface has been measured to be $\Gamma = 7.9\,J/m^2$ by Maranchi et al. [138]. According to Irwin [139] and Griffith [139], the crack will propagate only if the energy release rate G is greater than the fracture energy Γ. Using the computed maximum normal stress, σ_{max} = 0.74 GPa, and shear stress, τ_{max} = 0.27 GPa, we calculated a_c to be 203nm. TEM analysis of multiple beam cross-sections revealed the presence of some pre-existing flaws with a size of ~20-30 nm (Fig. 3.2f). The order-of-magnitude difference between the calculated critical interfacial flaw size and the size of voids observed through TEM suggests that the Cu-Si core-shell beam is unlikely to delaminate during lithiation.

We also performed a simulation including both lithiation and delithiation steps at 1C. The delithiation step began as soon as any element in the body reached a normalized concentration of one, and proceeded until any point in the body reached a concentration of 1%. Similar to Fig. 3.8c, d, Fig. 3.9a, b show the interfacial normal stress and shear stress at the Cu-Si interface. For the normal stress (Fig. 3.9a), we noted that the interfacial stresses during delithiation are mainly compressive, and hence would not be expected to cause delamination. For the shear stress (Fig. 3.9b), we noted that the magnitude of the maximum interfacial shear stress during delithiation is lower than that during lithiation. This suggests that interfacial delamination is unlikely during delithiation. The maximum principal stress in the Si shell is tensile during delithiation with a larger magnitude towards the exterior surface of the Si shell, and reaches ~1.70 GPa at the end of delithiation (Fig. 3.9c). This value is greater than the critical stress of 1.35 GPa computed in our analysis assuming a pre-existing Si flaw size of the shell thickness. Hence it is possible for fracture to occur inside the Si shell during delithiation. Given the maximum attained stress in Si in our simulation, the critical Si flaw size h_c which would cause cohesive fracture inside the Si shell is 127 nm [133,141]. TEM analysis and *in situ* observations indicated that it is unlikely that the Si shell contains such large flaws, which correspond to roughly half the thickness of the as-deposited Si shell.

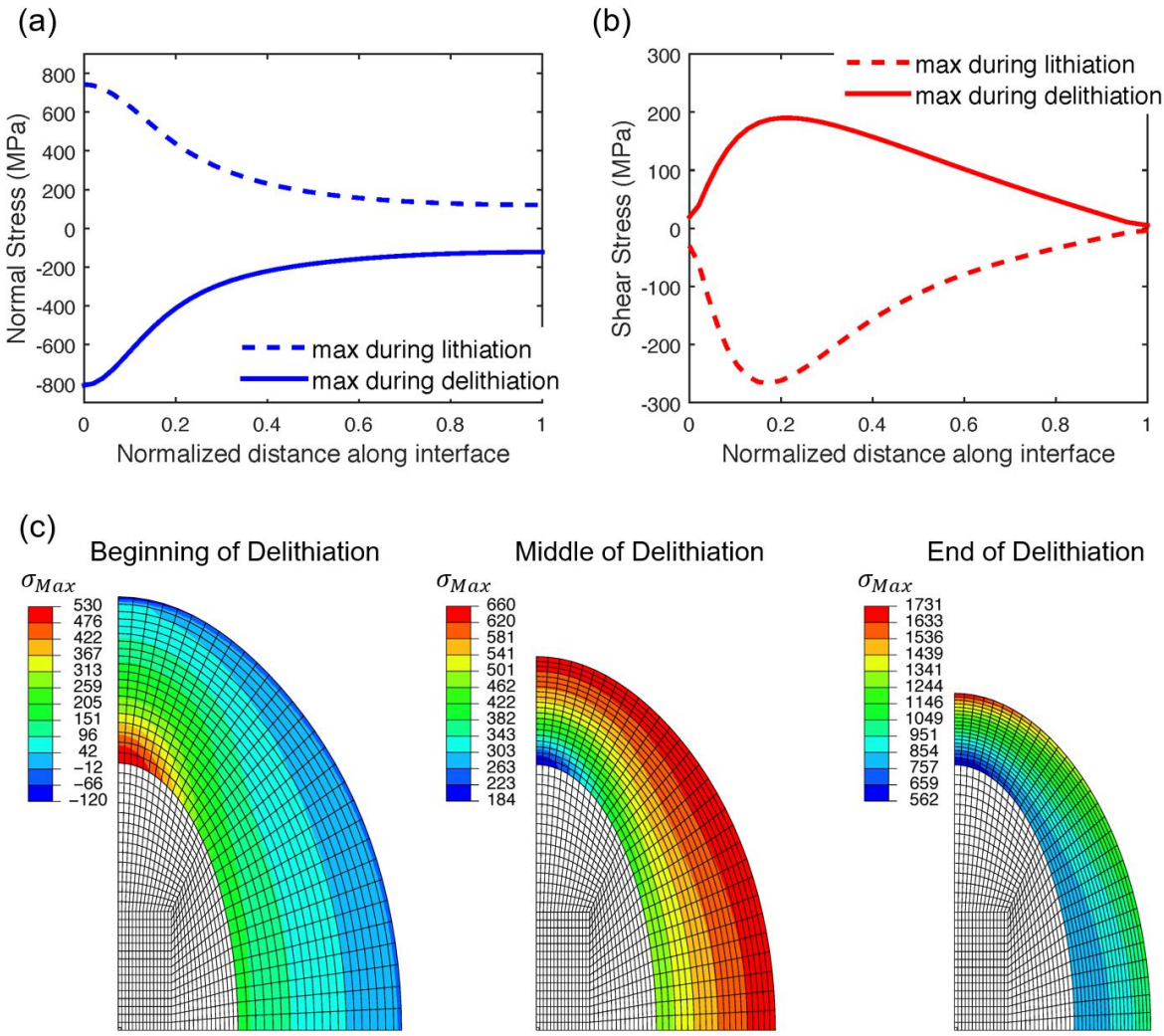

Figure 3.9 Distribution profile of the maximum interfacial (a) shear and (b) normal stress during lithiation and delithiation calculated by finite element modeling. (c) Contours of the maximum principal stress of the a-Si shell in the beginning, middle and final stage of delithiation.

One limitation of the described fabrication method is the elliptical beam cross-section caused by the laser voxel of two-photon lithography. Our simulations suggest that the interfacial shear stress can be completely eliminated and the interfacial normal stress would be uniformly distributed with a 31% lower maximum stress if the nanolattice beams had circular cross-sections. Fig. 3.10a, b show the calculated maximum normal and shear stresses at the Cu-Si interface at the time of maximum stress during lithiation. The reduced stresses in circular beams increase the critical interfacial flaw size a_c for delamination to 467 nm, a ~130% improvement compared with elliptical beams. Moreover, it appears that the lithiation rate also has a significant impact on the developed stresses. Fig. 3.10c, d display the computed maximum normal and shear stresses at the Cu-Si interface at

varying lithiation rates and reveal that the maximum interfacial normal stress increases from 0.57 GPa at 0.1C to 0.74 GPa at 1C and 0.82 GPa at 10C. The maximum interfacial shear stress increases from 0.25 GPa at 0.1C to 0.27 GPa at 1C and remains stable at 0.27 GPa as the lithiation rate increases to 10C. We attribute this rate-dependent characteristic to the strain rate sensitivity of plastic relaxation in the Si shell.

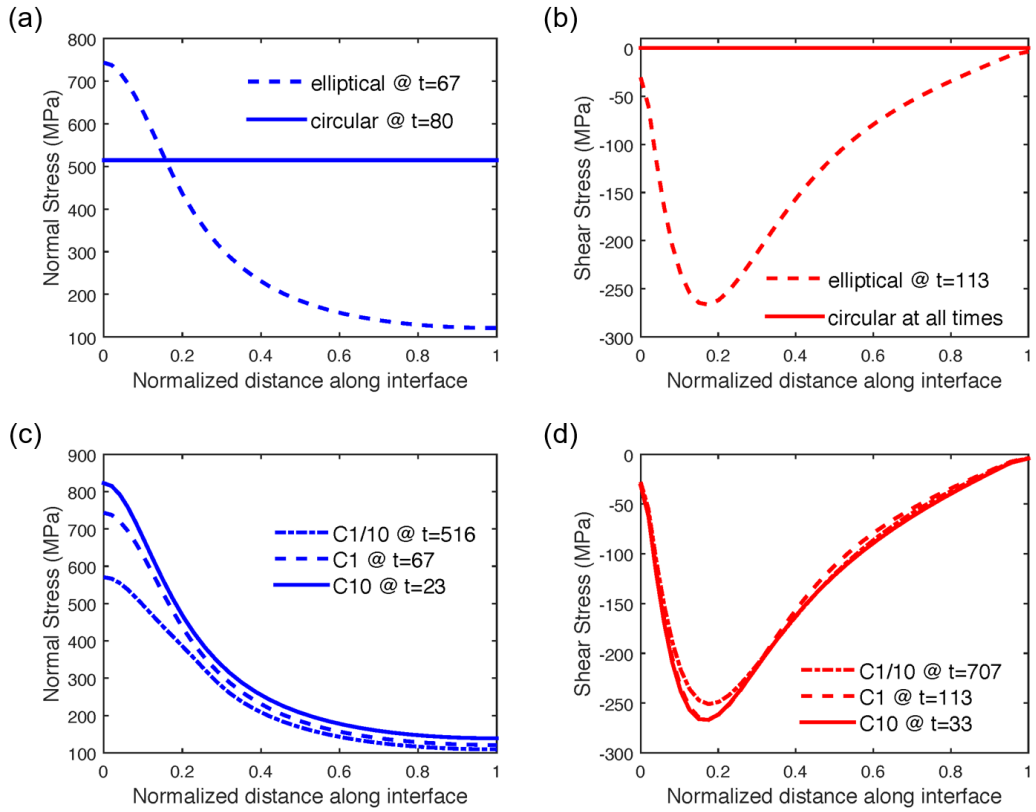

Figure 3.10 (a) Maximum interfacial normal and (b) shear stress attained for elliptical and circular beams. (c) Maximum interfacial normal and (d) shear stress attained at three different lithiation rates for elliptical beams.

3.6 Outlook and Summary

The Cu-Si core-shell nanolattices demonstrate how three-dimensional nano-architecture design could potentially resolve some of the key limitations of high-energy-density electrode materials (e.g. Si, Ge and S) that undergo alloying or conversion reactions upon lithiation: mechanical failure, sluggish kinetics, and low active material loading. For traditional thin film or slurry-assembled electrodes, simply reducing the film thickness or particle size to the nanoscale improves their mechanical stability at the cost of low active material loading and loss of capacity due to SEI formation [104]. For the same amount of electrode material, nano-sizing means packing orders of

magnitude more particles in the slurry, which results in high tortuosity and poor inter-particle transport. Our core-shell nanolattice fabrication method decouples these constraints by designing in different scales from lattice beams to unit cells and device-scale architectures. Via finite element analysis, the critical beam diameter and shell thickness can be calculated for each core-shell beam to maintain mechanical stability while limiting the surface-to-volume ratio to reduce capacity loss due to SEI formation. The unit cell size and geometry can then be optimized to fine-tune the relative density of the active material to increase volumetric energy density while leaving just enough pore space for lithiation-induced volume expansion. In this work, Cu occupies ~24% of the unit cell volume and Si ~19% so after 250% Si volume expansion, ~90% of the unit cell is solid. The solid Cu beams can be replaced with hollow ones [10] to further increase the gravimetric energy density. The electrode mass loading per footprint area, crucial for microbatteries for implantable or on-chip applications, can be easily scaled up by packing more unit cells in the vertical direction, given the good mechanical properties of such lattice structures under uniaxial compression [10,18]. Finally, by the nature of the freestanding core-shell lattice, the transport properties, important for high power applications, are not affected by active material loading, and the need for binder and conductive additives is eliminated. For the Cu-Si nanolattices, the interconnected Cu scaffold and the liquid electrolyte facilitate fast electron and ion transport efficiently throughout the electrode. In addition, compared with slurry-assembled electrodes with convoluted transport pathways, the core-shell nanolattices are more amenable to analyze using computer modeling and theory. Electrode architecture design will potentially enable the fabrication of all-solid-state 3D-architected batteries where the cathode material is inserted into the pores in the nanolattice anode, separated by a conformal layer of solid electrolyte [142,143].

While nano-architected electrodes offer a new perspective to tackle some of the most critical issues associated with high-energy-density battery materials, their manufacturing scalability poses a significant challenge for mass production. Two-photon lithography is ideal for building a fundamental understanding of how rational architecture design could improve battery performance, but its limitation in size and speed makes it only feasible for microbattery applications like micro-electromechanical systems (MEMS) [144] and implantable devices [145]. Fabrication methods based on self-assembly [105] and holographic patterning [114] can produce scalable nano-architectures, but their design space is less versatile. Progress in additive

manufacturing shows promises for large-scale production of architected materials. Zheng et al. recently reported Large Area Projection Micro-stereolithography [72] that can create 5cm-sized hierarchical metamaterials with disparate three-dimensional features spanning seven orders of magnitude by combining a low-cost spatial light modulator with an optical scanning system. We believe continued research and development will eventually bring the cost of nano-architected materials to a commercially viable level for battery applications.

In summary, we fabricated 3-dimensional Cu-Si core-shell nanolattices that serve as mechanically-robust Li-ion battery electrodes. We report architecture-level *in situ* SEM observations of electrode lithiation and delithiation, which demonstrate that the nanolattices can accommodate ~250% volumetric expansion with minimal electrode-wide expansion and no observed cracks. We employed a coupled deformation-diffusion model to quantitatively capture the stress evolution in the nanolattice beams, which attributes the enhanced mechanical robustness of the nanolattice to the plastic deformation of lithiated Si in the core-shell beams. Our work reveals that rationally designed three-dimensional nano-architecture can proliferate the mechanically robust, crack-suppressing characteristics of nanoscale Si onto device-scale, binder-free electrodes. The high degree of control over material architecture is useful for the facile discovery of mechanically robust and kinetically agile electrode materials in energy storage systems and other functional devices in which mechanical and transport phenomena are important.

Chapter 4

ELECTROCHEMICALLY RECONFIGURABLE ARCHITECTED MATERIALS

4.1 Reconfiguration of Architected Materials after Fabrication

Architected materials represent an area of active research because they exhibit exotic properties such as negative Poisson's ratios [1,2] and negative refractive indices [3,4], and decouple material properties that have historically been correlated such as strength vs. density [9,10] and thermal conductivity vs. stiffness [146]. Most architected materials reported to date are passive in the sense that they have a prescribed geometry fulfilling a single functionality. It was recently shown that the structure of architected materials can be reconfigured by mechanical deformation[36] and instabilities [34,37,147,148], hydration-induced swelling [38,71,149,150], as well as magnetic actuation [69]. A few examples are shown in Fig. 4.1. Such smart, multi-functional materials could have a long-lasting impact on implantable, deployable, and dynamically tunable devices if they could overcome the challenges of (1) requiring bulky external control, (2) only toggling between "on" and "off" states, and (3) reverting to the initial structure once the external stimulus is removed. Furthermore, most of these reconfigurable systems are small and idealized; increasing the number of repeating units in periodic architected materials could potentially induce inhomogeneities similar to defects, gradients or grain boundaries [53,151], which govern the properties of classical materials.

In this chapter, we demonstrate a new mechanism to dynamically reconfigure architected materials by exploiting electrochemically driven alloying/dealloying reactions to enable continuous, non-volatile and reversible structural transformations [152]. We used the alloying couple of silicon and lithium as a prototype system because Si is a high-capacity battery electrode material notorious for its ~300% volumetric expansion after full lithiation [103]. Buckling instabilities were observed in Si nanowires [153] and etched honeycomb patterns [154,155] during lithiation, but they have not been systematically investigated as a design tool to achieve structural reconfiguration. Leveraging on the mechanical resilience of Si at small scales [103], we designed and fabricated Si-coated tetragonal microlattices purposely structured to promote lateral in-plane buckling. *In situ* lithiation/delithiation

observations revealed cooperative buckling among neighboring beams that reconfigures the tetragonal unit cells into curved ones with pairwise opposite concavity. Through experiments and finite element modeling, we discovered that the bistability of in-plane buckling leads to the formation of multiple lateral domains separated by distorted domain boundaries, with domain sizes and distribution governed by defects and lithiation rate. We analyzed this phenomenon using a statistical mechanics approach analogous to the Ising model, and further designed artificial defects in Si microlattices to deterministically control buckling directions, which allowed us to effectively program domain boundaries to emerge in prescribed patterns upon lithiation. Understanding and controlling defects provide a pathway to drive the dynamic response of architected materials according to a particular trajectory. This new class of electrochemically reconfigurable architected materials has significant implications as it creates new vistas in designing, for example, battery electrodes with novel stress-relief mechanisms and dynamic mechanical metamaterials with tunable phononic band gaps.

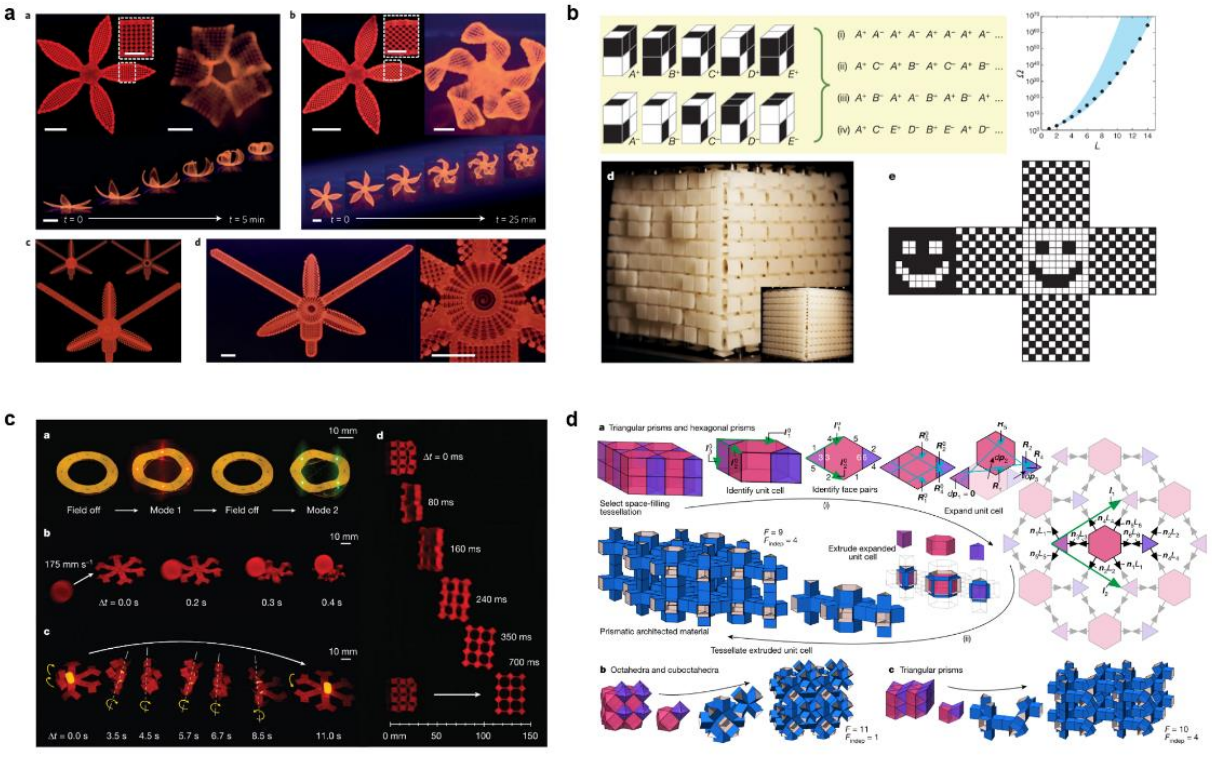

Figure 4.1 Various mechanisms to reconfigure architected materials. (a) Hydration-induced swelling. Adapted from [71]. (b) Mechanical deformation. Adapted from [37]. (c) Magnetic actuation. Adapted from [69]. (d) Algorithm-predicted folding. Adapted from [36].

4.2 Design of Electrochemically Reconfigurable Si Microlattices

To create micro-architectures with a propensity for collective in-plane buckling, we designed a periodic three-dimensional (3D) lattice comprised of tetragonal unit cells with slender horizontal beams connected to stubby vertical posts. Fig. 4.2a shows a schematic of this lattice geometry and the fabrication process. We first printed the polymer tetragonal lattice on a glass substrate using two-photon lithography, then sputtered a ~100 nm-thick Ni conductive layer and deposited a ~300 nm-thick amorphous Si layer onto each beam within the structure using plasma-enhanced chemical vapor deposition (PECVD). Each sample contained 79 (width) ×79 (length) ×5 (height) unit cells, and each tetragonal unit cell had a width of 20 μm (horizontal beam length) and a height of 5 μm (vertical post length) (Fig. 4.2b-e). The horizontal beams had an elliptical cross-section with a vertical major axis of ~2.6 μm and a minor axis of ~1.3 μm; the vertical posts had a circular cross-section with a diameter of ~2.6 μm. A square grid with 5 μm spacing was also patterned on the substrate to prevent delamination of Si thin film underneath the microlattice (Fig. 4.2c). Each sample contained ~8.0 μg of Si as the electrochemically active component, with an areal Si loading of 0.25 mg/cm^2.

Lithiation of Si microlattices inside modified coin cells was conducted galvanostatically at a constant current of 5 μA with a Li counter electrode until the voltage dropped to a cutoff voltage of 0.01 V vs. Li/Li$^+$. This applied current corresponds to a current density of 0.15 mA/cm^2 and a C-rate of ~C/6, where a C-rate of 1C represents the current at which it takes 1 hour to attain the theoretical capacity of the electrode [97]. Under these conditions, an average of ~80% of the theoretical capacity was attained after the first lithiation, which corresponds to ~240% of volumetric expansion in the Si shell [156]. SEM images in Fig. 4.2f-i demonstrate that Si microlattices deformed via cooperative beam buckling to result in an orthogonal sinusoidal pattern with pairwise opposite concavity upon lithiation. Each horizontal beam accommodated the volumetric expansion through radial growth of the cross-sectional area and axial elongation, which prompted in-plane beam buckling. The two ends of each beam were connected to two nearest-neighbor nodes, which rotated in opposite directions in response to buckling-induced torque. We did not observe any cracking or failure of the beams after lithiation, and the lattice remained in this stable, buckled state after removing the applied current. The buckling directions of four horizontal beams connected at a specific node were coupled through the node's rotation, and such

cooperative buckling led to the formation of the ordered sinusoidal pattern in the lateral planes (Fig. 4.2g), which is known for its auxetic behavior [157–159]. The bistability of in-plane beam buckling led to the formation of multiple domains in the microlattice (Fig. 4.2h, i), with the domain boundaries defined by Mode-II buckled beams as labelled in blue in Fig. 4.2h. The buckling pattern transcended vertically across all out-of-plane layers through twisting of the vertical posts (Fig. 4.2f).

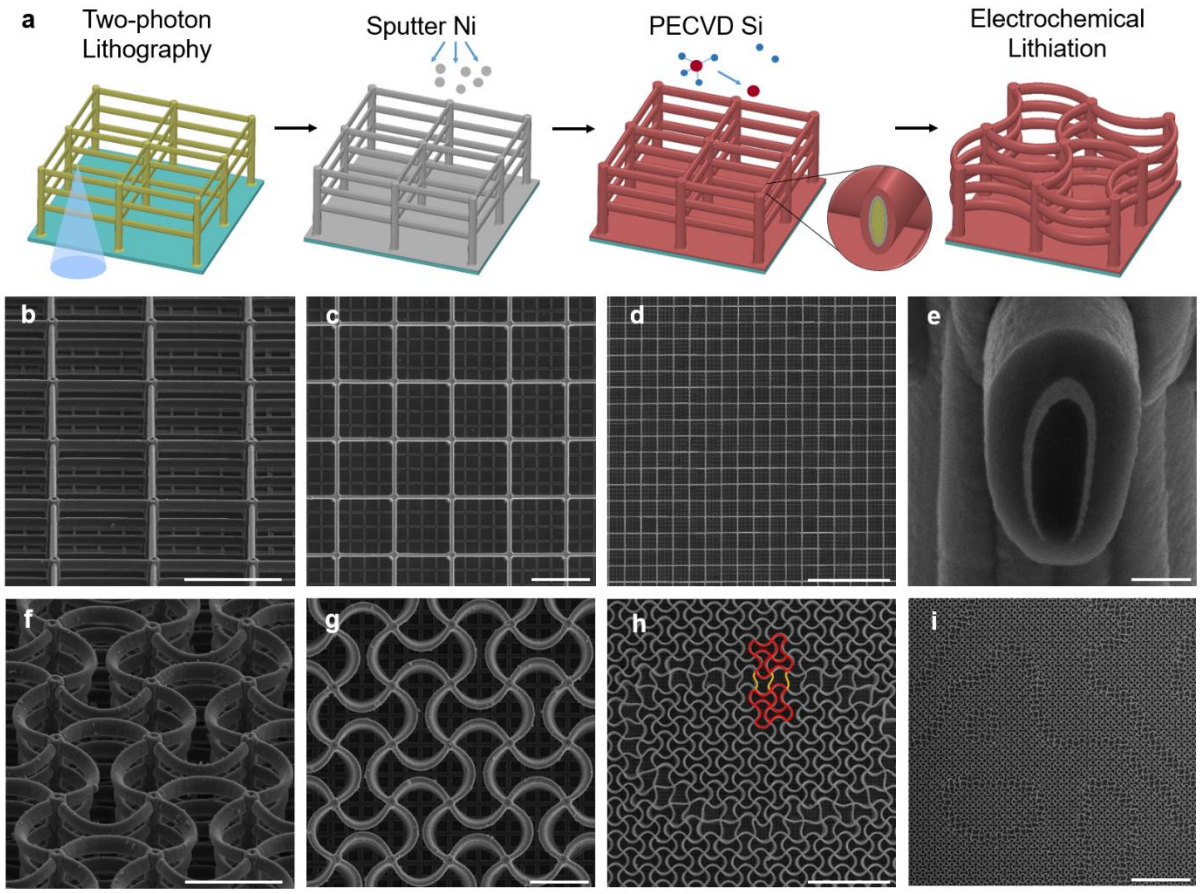

Figure 4.2 Fabrication process and SEM characterization of Si microlattices before and after lithiation. (a) Illustration of the fabrication process of Si microlattices and their structural transformation after lithiation. (b-d) SEM images of as-fabricated Si microlattices at different magnifications and tilts. (e) SEM image of a FIB-milled cross-section of a representative horizontal polymer-Ni-Si beam that shows a slight variation in the Ni and Si layer thickness. (f-i) SEM images of Si microlattices lithiated at a current of C/6 and a cutoff voltage of 0.01 V vs. Li/Li^+ at different magnifications and tilts. (b, e, f) are at a tilt angle of 52°. (c, d, g, j, i) are top-down views. (f, g) show the orthogonal sinusoidal pattern formed via cooperative buckling. (h, i) show multiple bistable domains adjoined by clearly visible boundaries. (h) contains an overlaid illustration of two ordered domains with Mode-I buckled beams (red) connected by Mode-II buckled beams (yellow) at the domain boundary. Scale bars: (b, c, f, g) 20 µm, (d, h) 100 µm, (e) 500 nm, (i) 200 µm.

4.3 Fabrication Method for Si-coated Tetragonal Microlattices

Tetragonal lattices with 20 μm × 20 μm × 5 μm (in x, y, and z-axis respectively) unit cells are designed in MATLAB and imported into a commercial two-photon lithography system (Photonic Professional GT, Nanoscribe GmbH). Each sample is consisted of a 10 × 10 array of stitched smaller lattices written sequentially due to the limited writing area of the two-photo lithography system. Each smaller tetragonal lattice has 8 × 8 × 5 unit cells, and stitched lattices overlap by one unit cell. Therefore, each sample has 79 × 79 × 5 unit cells in total written on a cleaned glass coverslip substrate (18 mm diameter circular No. 2 glass, VWR) with a custom-made photoresist. This negative photoresist is composed of 79.1 wt% Acrylo POSS monomer (MA0736, Hybrid Plastics Inc.), 20 wt% dichloromethane solvent (Sigma-Aldrich), and 0.9 wt% 7-diethylamino-3-thenoylcoumarin photoinitiator (Luxottica Exciton), and it is placed on top of the glass substrate. Immersion oil is used between the 63X objective of the two-photon lithography system and the bottom side of the glass substrate. After two-photon lithography, the sample is developed in PGMEA (propylene glycol monomethyl ether acetate, Sigma-Aldrich) for 25 min and rinsed in IPA for three times before critical point drying. Each polymer sample has elliptically cross-sectioned horizontal beams with a vertically aligned major axis of ~1.8 μm and a minor axis of ~0.5 μm and cylindrical vertical posts with a diameter of ~1.8 μm with small sample-to-sample variations due to two-photon lithography laser degradation. The bottom layer of the vertical post is extended to 10 μm to assist twisting of the vertical posts during lithiation, and in the bottom 3 μm of the vertical posts, the diameter gradually increases to ~3.6 μm to enhance adhesion with the substrate.

The polymer samples are cleaned by oxygen plasma and baked for 2 hr at 250°C in an Ar-filled glovebox before RF magnetron sputtering deposition of ~5 nm of Cr seed layer and ~100 nm of Ni conductive layer on lattice beams (100 W, 20 sccm Ar flow, 5 mTorr deposition pressure, AJA International, Inc.). The sputtered Ni film is thicker at the top of each horizontal beam and thinner at the bottom of each horizontal beam. Next, ~300 nm of amorphous Si (a-Si) is deposited by plasma enhanced chemical vapor deposition (PECVD, Oxford Instruments) at the following conditions: 200°C temperature, 400 mTorr pressure, 250 sccm of 5% silane in Ar precursor gas flow, and 10 W RF power. Finally, ~100 nm of Ni thin film is coated on the back of the sample substrate by sputtering with good electrical pathway to the Ni layer on top of the substrate through good Ni coverage on the edge of the substrate. During two-photon lithography, a 5 μm square grid

is written on the substrate underneath and 180 μm around the lattice (boundary marked by red dotted lines in Fig. 4.3a). A 1.8 mm square shadow mask is used during PECVD to limit the a-Si deposition to only the lattice section within the extent of the square grid to prevent Si thin film delamination on the substrate (mask boundary marked by green dotted lines in Fig. 4.3a, d). Fig. 4.3d shows Si thin film delamination when a section of the square grid is missing due to accident interface finding error during two-photon lithography. Finally, non-contact support structures are added on the outside of exterior vertical posts to prevent them from leaning outwards during Si microlattice lithiation due to the absence of periodic boundary conditions (Fig. 4.3b, c, e, f). The total Si mass loading on each sample is measured by Cahn C-35 microbalance to be 8.0±0.4 μg by mass measurements before and after KOH etching of Si on the lattice. Part of the substrate has to be cut off by a diamond pen to keep the total sample mass within the range with 0.1 μg sensitivity so measuring Si mass for each sample before electrochemical testing is not practical. Variation of Si mass loading is observed across samples due to two-photon lithography laser degradation and PECVD chamber conditions during Si deposition. The areal Si mass loading calculated from the area of the Si deposition shadow mask is ~0.25 mg/cm^2. The theoretical capacity for each Si microlattice sample is ~29 μAh based on Si's theoretical specific capacity of 3600 mAh/g [97].

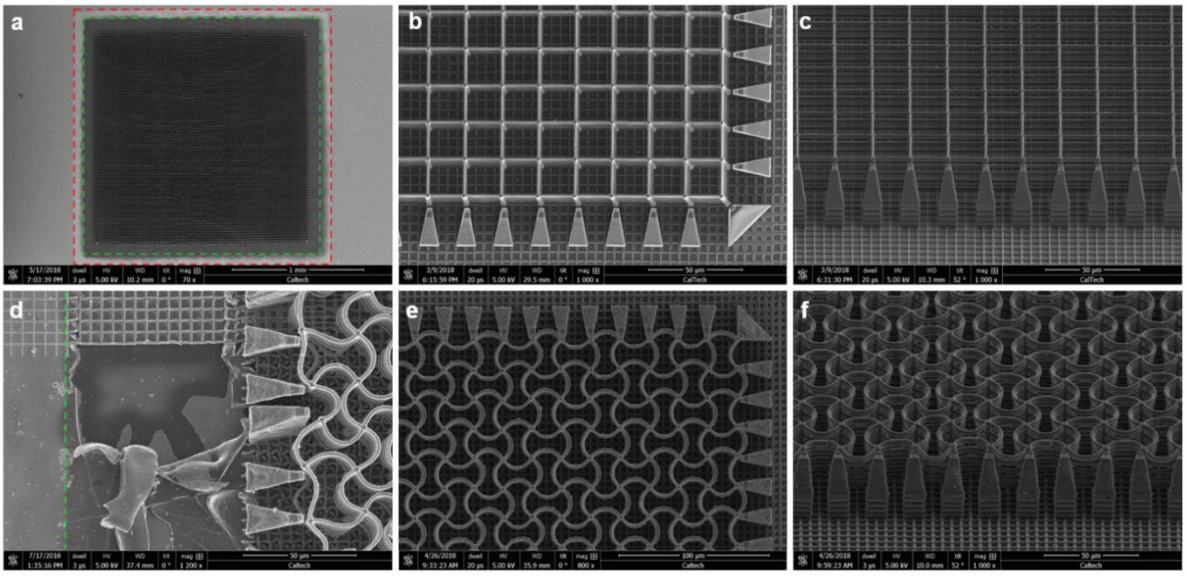

Figure 4.3 SEM images of Si microlattice fabrication details (a-c) before lithiation and (d-f) after lithiation. (a, b) describe the boundaries of the square shadow mask (green dotted lines) used during PECVD is in between the edges of the microlattice and the edges of the square grid on the substrate (red dotted lines). (b,

c, e, f) show non-contacting support structures on the outside of exterior vertical posts that effectively prevent them from leaning outwards during lithiation despite the absence of periodic boundary conditions at the edges.

4.4 Comparison with Lattice Geometries with Higher Symmetry

The rationale for choosing the specific tetragonal lattice geometry is briefly discussed below. The cross-sectional dimensions of individual beams were mainly dictated by the resolution of the two-photon lithography process; we chose the thickness of Si layer to be below the critical length scale for fracture and delamination through so-called size effects in the mechanical properties of Si at small scales during lithiation and delithiation. The elliptical shape of the beam cross-section with vertically aligned major axis constrains the lowest energy buckling modes to be in-plane and also minimizes feature size because the writing voxel in two-photon lithography is an ellipsoid; beams with circular cross-sections require hatching, which expands their dimensions. Horizontal beams with circular cross-sections and similar diameters would still undergo cooperative buckling in a virtually identical way because on the structural level, the in-plane buckling deformation is prompted by the constraints imposed by the vertical posts which are free to rotate but cannot have translational motion laterally. However, the buckled circular beams might bend out of plane slightly especially on the topmost layer. We chose tetragonal lattice geometry (square lattice in the lateral plane) for its simplicity in design and fabrication. We also fabricated other, higher-symmetry lattices with equivalent beam dimensions and similarly adjoined and supported by vertical posts, such as hexagonal and triangular lattices, as shown in Fig. 4.4a-f. Upon lithiation, we found the hexagonal lattice to buckle into an ordered geometry (Fig. 4.4b), closely resembling one reported in [154], and the triangular lattice buckled into a “frustrated” geometry (Fig. 4.4e), similar to what is reported in [38]. We learned that these higher-symmetry lattices were more susceptible to fabrication defects, for example stitching inaccuracies during fabrication, as shown by the periodic distortions in zoomed-out SEM images in Fig. 4.4c, f. This is most probably because the large samples are stitched from smaller lattices during two-photon lithography in x and y directions, the effective defects due to stitching are more pronounced for lattices with higher symmetry with non-orthogonal coordinates. This observation also illustrates the importance of defects in reconfigurable architected materials.

The horizontal beams in tetragonal lattices with wider, 3.8 μm-diameter vertical posts also buckled cooperatively as a result of lithiation, but the domain boundaries had frequent overlaps with

periodic stitching sites (Fig. 4.4i), which indicates that the larger torsional stiffness of the vertical posts exaggerates the influence of stitching inaccuracies. Through empirical, iterative exploration, we found that vertical posts with diameters of 2.6 μm had the best combination of structural stability and minimal stitching influence on domain formation. Narrower vertical posts would actually snap in the bottom layer upon lithiation driven by the greater degree of rotation. The total number of vertical layers and the lateral size of Si microlattices were chosen to optimize the trade-off between higher active material loading and reasonable fabrication time.

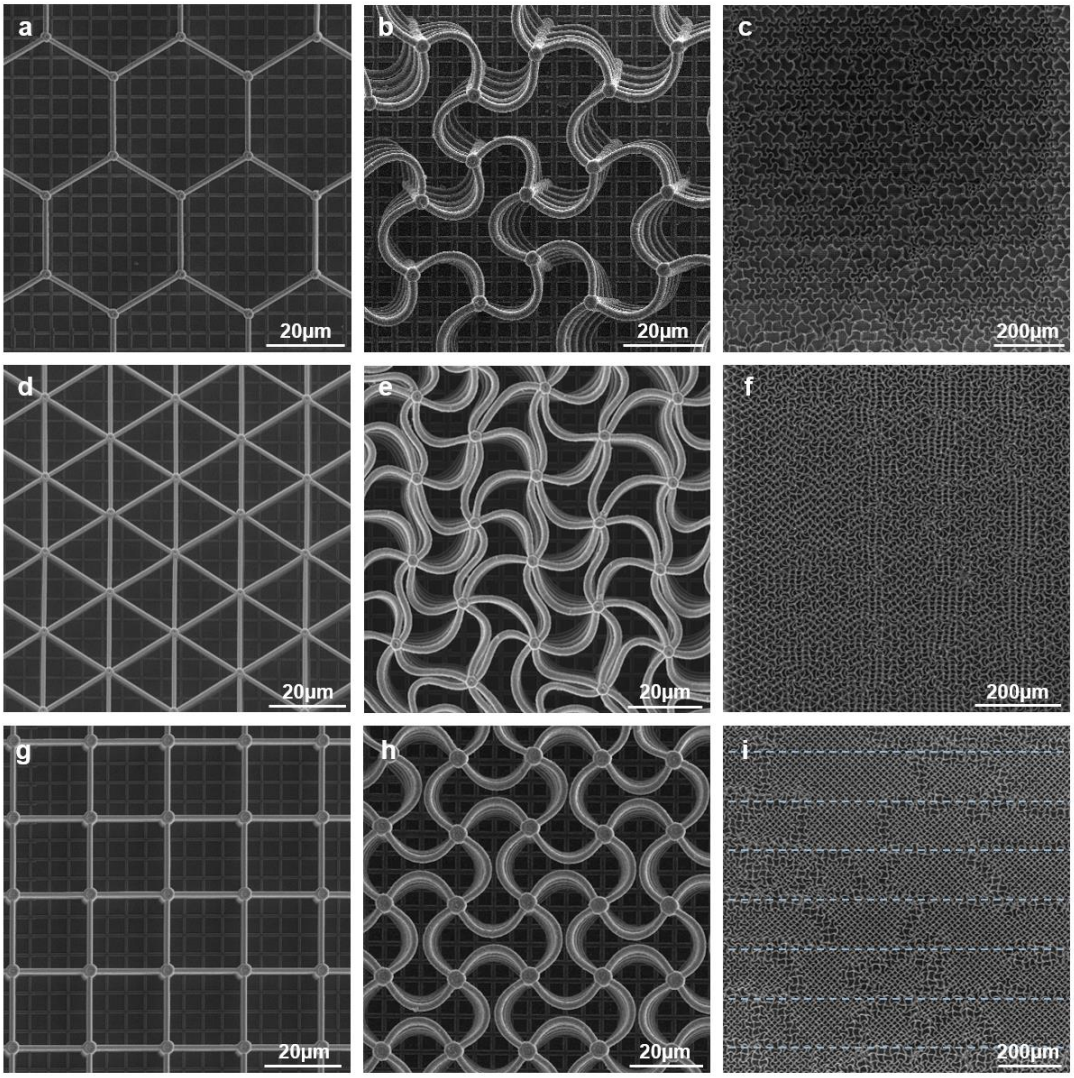

Figure 4.4 SEM images of hexagonal microlattices before (a) and after lithiation (b, c). SEM images of triangular microlattices before (d) and after lithiation (e, f). SEM images of tetragonal microlattices with a larger vertical post diameter before (g) and after lithiation (h, i). Dotted horizontal lines in (i) help to mark the stitching sites that have a strong influence over the domain boundary location when a larger vertical post diameter is used.

4.5 Sn Microlattice Fabrication and Comparison

To demonstrate electrochemically driven cooperative buckling is not specific to the Si-Li alloying chemistry, we fabricated Sn microlattices and observed a similar lithiation-induced cooperative buckling behavior. Approximately 200 nm of Sn is deposited onto the polymer lattice by RF magnetron sputtering (75 W, 20 sccm Ar flow, 5 mTorr deposition pressure, AJA International, Inc.). Due to Sn's low melting temperature, the sputtered Sn film is highly faceted and concentrates on top of the horizontal beams with extruding crystalline grains of ~1 μm in size. In this case, Sn functions as both active material and current collector. Despite significant differences in surface morphology between Sn and Si microlattice beams, the Sn microlattices also buckle cooperatively into the sinusoidal pattern upon lithiation-induced volume expansion (Fig. 4.5). Similar to Si, Sn has many intermetallic alloying phases with Li, and has a theoretical Li insertion capacity of 993 mAh/g-Sn with 244 % volumetric expansion [97].

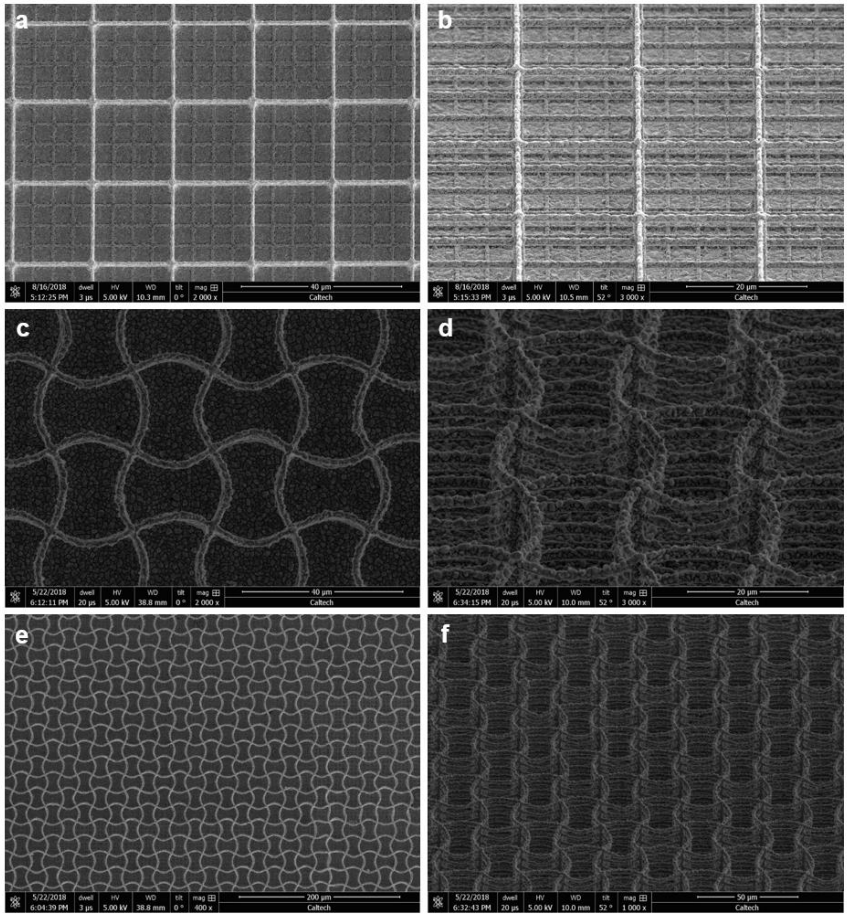

Figure 4.5 (a, b) SEM images of representative as-fabricated Sn microlattices. (c-f) SEM images of representative Sn microlattices after lithiation.

4.6 Electrochemical Testing Method

Modified CR2032 coin cells are used to test Si microlattices for long-term cycling with accurate electrochemical data and minimized side reactions. As shown in Fig. 4.6a, a 0.79 mm thick polyethylene washer is adhered to the sample substrate via re-solidified paraffin wax (Sigma-Aldrich) to create a small leak-free cavity around the Si microlattice, which significantly reduces the amount of electrolyte used and the contact area between electrolyte and Ni thin film on the substrate. Approximately 30 µl of electrolyte is used in each coin cell, and the electrolyte consists of 90 vol% of 1 M $LiPF_6$ in EC/DEC = 50/50 (v/v) (battery grade, Sigma-Aldrich) and 10 vol% FEC additive (BASF). A Li foil counter electrode with a 25 µm-thick separator (Samsung) is placed on top of the polyethylene washer cavity filled with electrolyte. The modified coin cells are sealed by a crimper inside an Ar-filled glovebox before taking out for electrochemical testing. Elevated temperature experiments are conducted inside an environmental chamber using coin cells. For each sample, we wait for 1hr before lithiation after putting the cell inside the environmental chamber at the set temperature for the cell to reach thermal equilibrium.

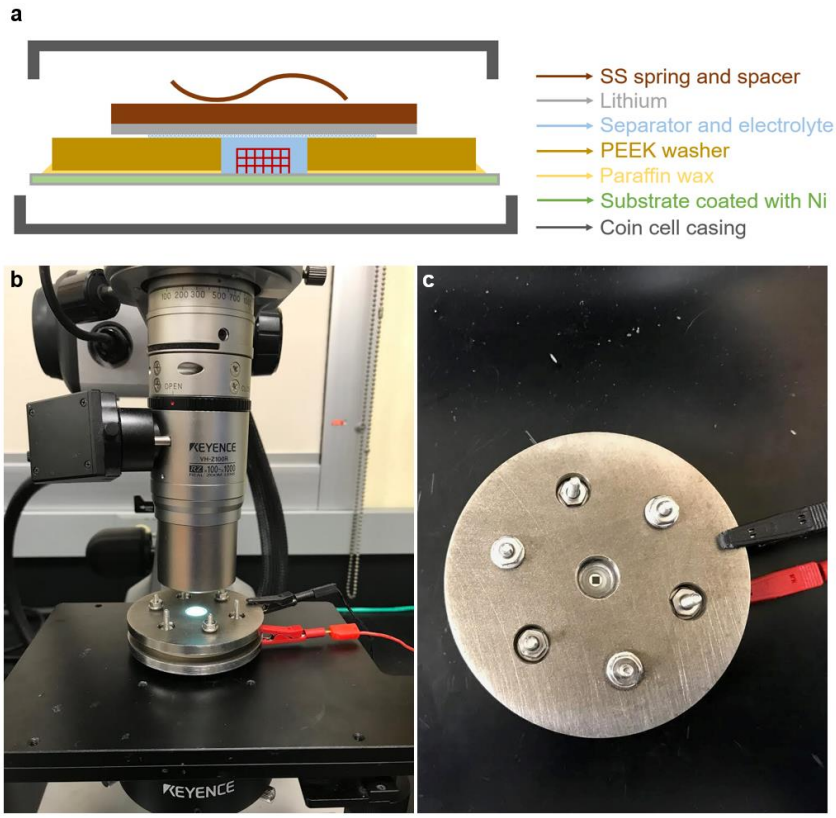

Figure 4.6 (a) Illustration of modified coin cells. (b, c) Images of the *in situ* optical microscopy setup and the custom electrochemical cell with a quartz viewing window.

A custom-made electrochemical cell with a quartz window for *in situ* optical observation is shown in Fig. 4.6b, c. A Li foil is punched into a ring shape to unblock the top-down view of the Si microlattice during *in situ* observation. Approximately 400 μl of 1 M $LiPF_6$ in EC/DEC = 50/50 (v/v) (battery grade, Sigma-Aldrich) electrolyte is used for each *in situ* cell. The large electrolyte amount gives rise to significant side reactions from electrolyte decomposition and impurities like water and oxygen, which leads to larger and inaccurate lithiation capacity. During electrochemical lithiation/delithiation, Keyence VW-9000 digital microscope records the dynamics of cooperative buckling/unbuckling in the Si microlattices.

All lithiation, delithiation and cycling tests are conducted galvanostatically with a constant current using a battery cycler (BCS 805, Bio-Logic Science Instruments) or a potentiostat (SP 200, Bio-Logic Science Instruments) unless otherwise specified. The applied current is quantified by the C-rate, where a C-rate of x·C is defined as the current under which the electrochemical reaction can be completed in 1/x hours based on the theoretical capacity of the active material. The theoretical capacity of the Si microlattice samples is approximated to be 30 μAh when calculating the C-rate. Therefore, a constant current of 5 μA, i.e. a current density of 0.15 mA/cm^2 normalized by the Si coated area, corresponds to a C-rate of ~C/6. For the Si microlattice-Li half cells, the lithiation (discharge) cutoff voltage is 0.01 V vs. Li/Li^+ and the delithiation (charge) cutoff voltage is 1.5 V vs. Li/Li^+ for full delithiation and 0.6 V vs. Li/Li^+ for partial delithiation. The first cycle Coulombic efficiency is ~70 % with the 0.6 V delithiation cutoff voltage, which indicates that about 30 % of inserted Li remains in the Si microlattices. Cyclic voltammetry (CV) is conducted at a scan rate of 0.1 mV/s between 0.01 V and 1.5 V vs. Li/Li^+ in modified coin cells. The shape and the current peaks of the CV plot are consistent with previously published results of various Si anodes [109,160]. It conveys the reversible Si-Li alloying and dealloying reactions indicated by the reduction peaks around 0.03 V and 0.21 V and the oxidation peaks around 0.33 V and 0.49 V respectively. The initial lithiation of pristine Si occurred at a lower voltage around 0.11V, and weak reduction peaks around 0.40 V appeared in the second and third cycles possibly caused by irreversible Li insertion; these features are consistent with reports for various binder-free amorphous Si electrodes [109,113,128].

4.7 *In situ* Observation of Lithiation-induced Cooperative Buckling

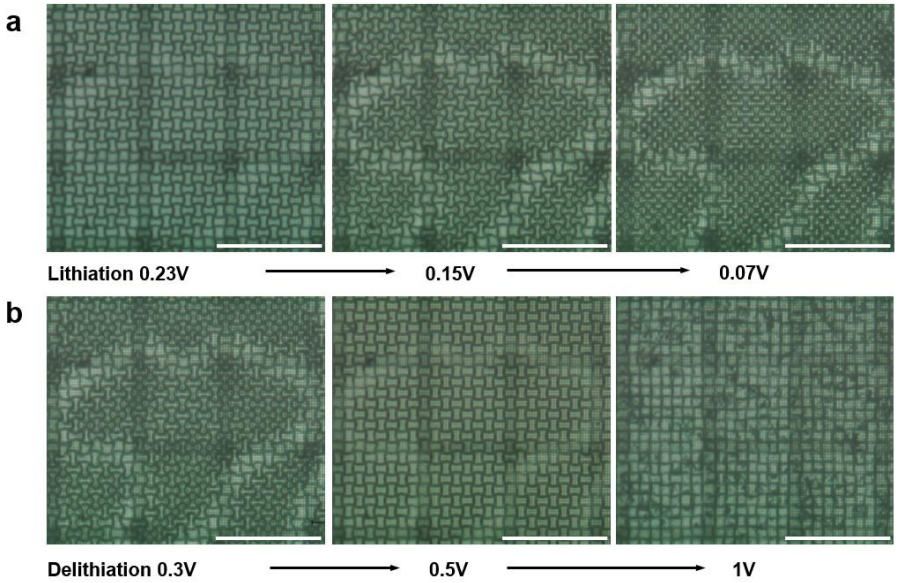

Figure 4.7 *In situ* optical characterization of lithiation-induced cooperative buckling in Si microlattices. Progressive optical snapshots during *in situ* (a) lithiation and (b) delithiation at different voltages that reveal cooperative buckling, unbuckling, and domain formation.

We constructed an *in situ* optical setup to capture the dynamics of cooperative buckling and domain formation in real-time. A custom-made electrochemical cell with a quartz window was used to visualize structural transformations at a constant current of C/6 under a digital optical microscope. Fig. 4.7a, b present real-time snapshots of a typical *in situ* experiment at progressively lower voltages during lithiation (Fig. 4.7a) and at progressively higher voltages during delithiation (Fig. 4.7b). Lithiation was conducted until a cutoff voltage of 0.01 V, and delithiation was conducted until a cutoff voltage of 1.5 V. The corresponding *in situ* lithiation video (Supplementary Video 4) reveals that incipient slight buckling rapidly occurred on all horizontal beams, which continued to buckle simultaneously as lithiation proceeded. Domain boundaries emerged spontaneously between mismatched domains. During delithiation, the horizontal beams almost fully unbuckled, and fracture occurred at the nodes when voltage increased above ~0.6 V (Supplementary Video 5). These two videos are played at a speed of 2700X. The lithiation capacity in the *in situ* cell reached 122% of the theoretical capacity of Si, whereas the first lithiation capacity in modified coin cells is consistently ~80% of the theoretical capacity under the same galvanostatic conditions. The first cycle Coulombic efficiency was 44% compared with that of ~90% in coin cells under the same cycling conditions. These discrepancies demonstrate the significantly larger

side reactions in the *in situ* cell due to the large amount of electrolyte used. Therefore, we refer to different stages of lithiation and delithiation in the *in situ* experiments by the corresponding voltages in Fig. 4.7a, b instead of the attained capacities, and accurate electrochemical analysis and long-term cycling are conducted in modified coin cells. Fig. 4.8 are SEM images of a representative Si microlattice after the first *in situ* delithiation with a 1.5 V delithiation cutoff voltage showing the fractured nodes.

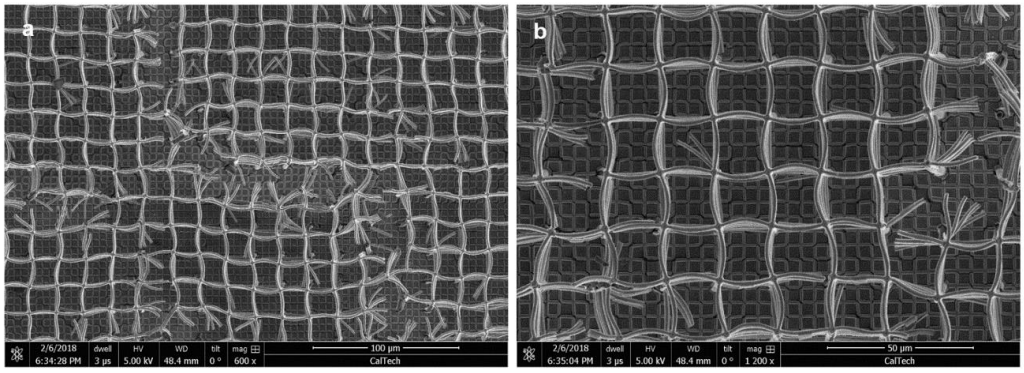

Figure 4.8 SEM images of a representative Si microlattice after the first delithiation with a 1.5 V delithiation cutoff voltage showing the fractured nodes.

Supplementary Video 6 shows lithiation-induced buckling at a playing speed of 150X when a 2000 Ω resistor load was applied between the Si microlattice and the Li counter electrode. The Si-Li alloying reaction is a spontaneous discharge process, which means that the alloy has a lower free energy than that of the two electrodes combined. This implies that the observed lithiation-induced cooperative buckling does not require additional energy supply to be activated or to proceed. Supplementary Video 6 presents thermodynamically driven lithiation and buckling of a Si microlattice drawing current from the alloying reaction for joule-heating of the 2000 Ω resistor. The Si microlattice sample had artificial defects that favor the single-domain buckling configuration. All beams buckled coherently as expected and a single domain was formed.

Supplementary Video 7 shows stable and reversible structural transformations of the 3rd charge, the 4th discharge, the 4th charge, and the 5th discharge at a high lithiation/delithiation rate of the same sample as in Supplementary Video 6 at a playing speed of 150X. The 3rd and the 4th charge were conducted at a constant voltage of 0.6 V with a current cutoff of 10 μA and took ~9 min to complete. The 4th discharge was conducted with a 221 Ω resistor load and a cutoff voltage of

0.005 V, which took ~14min to complete. The 5th discharge was conducted at a constant voltage of 0.01 V with a cutoff current of 20 μA, which took ~15 min to complete. The cutoff current for constant voltage discharge was relatively high because a significant amount of side reactions would continue to sustain the current when the current dropped below 20 μA, which was confirmed in other samples. In these constant voltage and resistor load discharge/charge experiments, the initial currents were very high (above 4C) and gradually slowed down as lithiation/delithiation proceeded so the majority of the buckling/unbuckling deformation happened in the first half of the lithiation/delithiation processes.

4.8 Electrochemical Characterization and Cycling of Si Microlattices

Fig. 4.9e shows a cyclic voltammogram (CV) of the first three cycles by scanning the voltage at a rate of 0.1 mV/s between 0.01 V and 1.5 V in a modified coin cell. It conveys the reversible Si-Li alloying and dealloying reactions indicated by the reduction peaks around 0.03 V and 0.21 V and the oxidation peaks around 0.33 V and 0.49 V, respectively [109,160]. Noticeable current fluctuations occurred during the third delithiation around 0.55 V, which correlates with the local fracture events observed around 0.6 V in the *in situ* delithiation experiment. To investigate if preventing these unstable events could improve cycling reversibility, we conducted galvanostatic cycling tests with two delithiation cutoff voltages of 1.5 V and 0.6 V. Fig. 4.9f compares the voltage vs. specific capacity profiles of the 1st and the 10th cycles for two samples with these two delithiation cutoff voltages; the voltages that correspond to the *in situ* snapshots in Fig. 4.9a, b are also labeled. This plot indicates that restricting the delithiation voltage to below 0.6 V retained ~30 % of the inserted Li during the 1st lithiation inside the microlattice and significantly improved the reversible capacity of the Si-Li alloying/dealloying reactions. SEM images of Si microlattices after the 10th lithiation and the 10th delithiation with a 0.6 V delithiation cutoff voltage in Fig. 4.9c, d reveal the structural integrity and the reversibility of geometric transformations in Si microlattices during stable electrochemical cycling. The Li storage capacity vs. cycle number plot in Fig. 4.9g demonstrates stable lithiation and delithiation cycling of Si microlattices, with a 50th cycle capacity retention of 2010 mAh/g-Si for a 0.6 V delithiation cutoff voltage compared with that of only 1025 mAh/g-Si for a 1.5V delithiation cutoff voltage at a constant current of C/6. Fig. 4.9g also shows the good rate capability of Si microlattices with a specific capacity of 1300 mAh/g-Si at a high cycling rate of 2C.

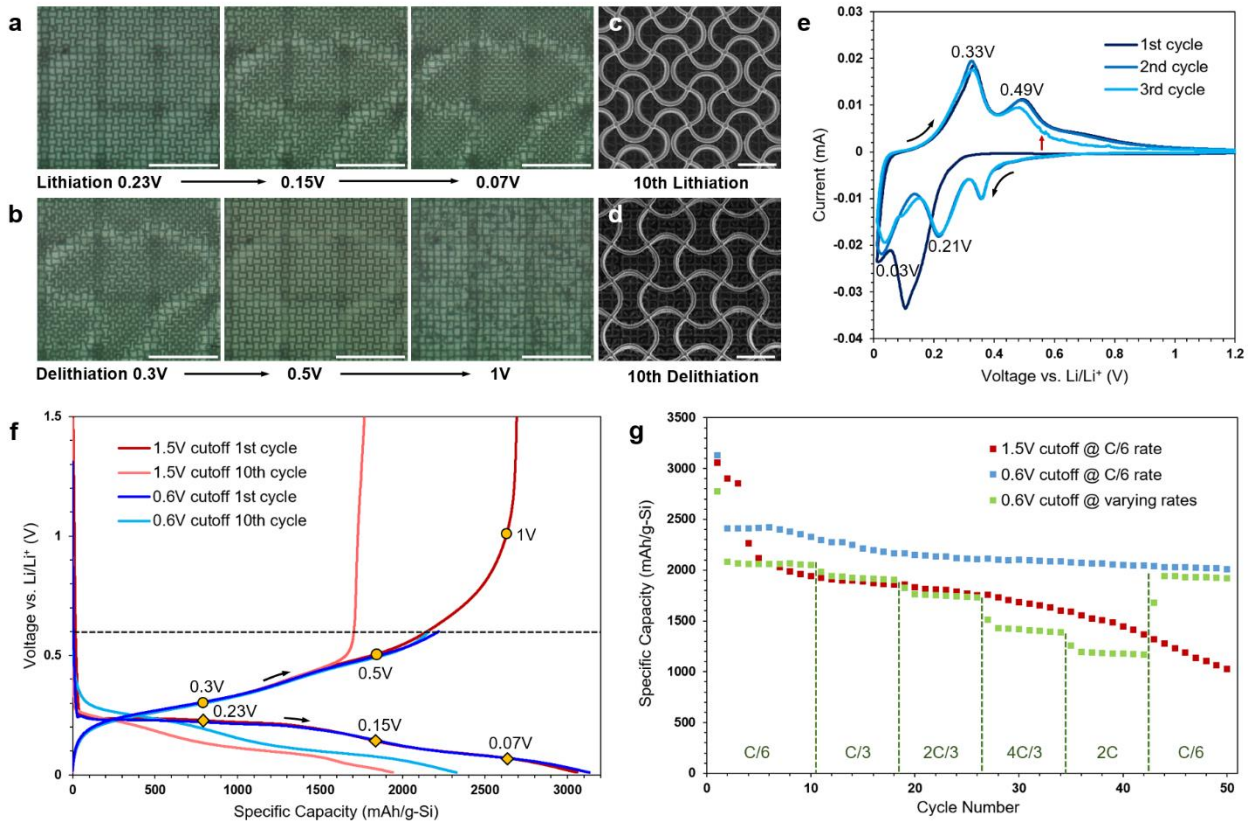

Figure 4.9 *In situ* optical and electrochemical characterization of lithiation-induced cooperative buckling in Si microlattices. (a, b) Progressive optical snapshots during *in situ* (a) lithiation and (b) delithiation at different voltages that reveal cooperative buckling, unbuckling, and domain formation. (c, d) SEM images of Si microlattices after (c) the 10th lithiation and (d) the 10th delithiation in modified coin cells with a 0.6 V delithiation cutoff voltage. (e) A cyclic voltammogram of a representative Si microlattice with a Li counter electrode at a scan rate of 0.1 mV/s between 0.01 V and 1.5 V. The red arrow points out the current fluctuation starting around 0.55V in the 3rd delithiation. (f) Voltage profiles of the 1st and the 10th cycles with 1.5 V and 0.6 V delithiation cutoff voltages in modified coin cells. The theoretical specific capacity of Si is 3600 mAh/g-Si[97]. The voltages labeled in (f) correspond to the voltages shown in (b, c) during *in situ* experiments. (g) Cycling performance of Si microlattices with 1.5 V and 0.6 V delithiation cutoffs at C/6 and at varying rates up to 2C. Scale bars: (a, b) 200 µm, (c, d) 20 µm.

Long-term cycling data of a Si microlattice at C/6 with a 0.6 V delithiation cutoff voltage is shown in Fig. 4.10a. The Si microlattice has a relatively stable capacity above 2000 mAh/g-Si in the first 50 cycles, and then the capacity starts to slowly decrease to 1030 mAh/g-Si in the 100th lithiation. Fig. 4.11 shows SEM images of representative Si microlattices with periodic artificial defects after the 101th lithiation. No fracture or other structural damage is observed in the buckled Si microlattices. The Si beam surface appears to be rougher after cycling with a layer of solid electrolyte interphase (SEI) (Fig. 4.11c, f, h). Focused Ion Beam is used to cut cross-sections of the horizontal beams in the SEM (Fig. 4.11g, h). The buckled beams remain in the same curvature

after being cut in the middle and removed from the boundary conditions at one end, which confirms that the concurrent plastic deformation during lithiation locks in the buckled geometry. Cracks are found in the Ni-polymer core of the beams but not in the Si layer (Fig. 4.11h). The bottom portions of the vertical posts appear to be loosely connected to the substrate, especially in the Ni and Si outer layers (marked by red arrows in Fig. 4.11i). We speculate the repeated twisting of the vertical posts during cycling gradually damages the electrical contact between the Si microlattice and the substrate, which would contribute to the capacity decay during long-term cycling. Other factors leading to the capacity decay include the relatively large side reactions due to the large electrolyte amount compared to the small sample size and repeated SEI formation and damage during each cycle. In all galvanostatic cycling tests, the Coulombic efficiency stabilized around 95% possibly due to the relatively substantial side reactions in the modified coin cells.

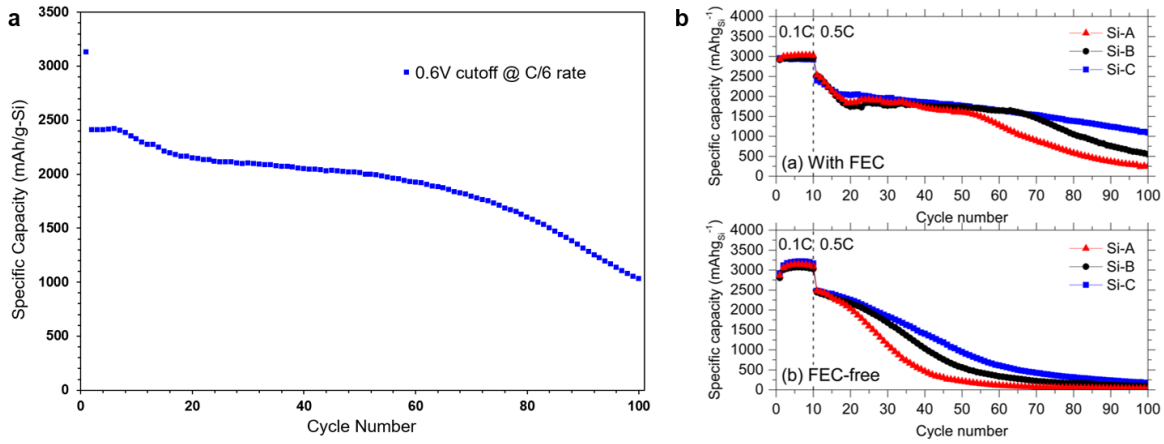

Figure 4.10 (a) Long-term coin cell cycling performance of a representative Si microlattice. (b) Cycling performance of Si nanoparticle electrodes adapted from [161]. Si-A, Si-B, and Si-C electrodes contains nanoparticles of approximately 130 nm, 90 nm, and 60 nm

Even though the cycling performance of Si microlattices is not optimized and limited by the issues mentioned above, it compares reasonably well with the reported Si nanoparticle electrode performance [161–163]. Within the battery community, a variety of results have been reported for Si electrodes, and the cycling performance of such cells strongly depends on the details of the cell assembly including but not limited to Si mass loading, particle size, and electrolyte additives, as summarized in a recent review by Feng et al. [162]. We compared the long-term cycling performance of Si microlattices with two recent mechanistic studies of Si electrode reversibility: one by Samsung Advanced Institute of Technology [163] and another by Argonne National

Laboratory [161]. Both studies attribute the underlying cause of Si capacity decay during cycling to parasitic reactions that generate the crystalline $Li_{15}Si_4$ phase, which is intrinsic to the Si-Li chemistry and not resolvable by any stress-relief mechanisms. As shown in Fig. 4.10b adapted from [161], the specific capacity retention of Si nanoparticle electrodes strongly depends on the particle size with smaller nanoscale particles leading to better cycling performance. However, smaller particles cause other problems, like low Si mass loading, high tortuosity for ion transport, greater surface area for solid-electrolyte-interphase formation, etc. in practical cells. The Si microlattices in this work have a 300 nm-thick continuous thin film Si coating, and their cycling performance compares decently with that of 90-130 nm-diameter Si nanoparticles under similar cycling conditions (Fig. 4.10). Even though this work is not aimed for specific battery applications, it has implications for future battery design by enabling fabrication of lightweight and mechanical robust electrodes whose architectural features can buckle to relieve mechanical stresses that arise from lithiation/delithiation.

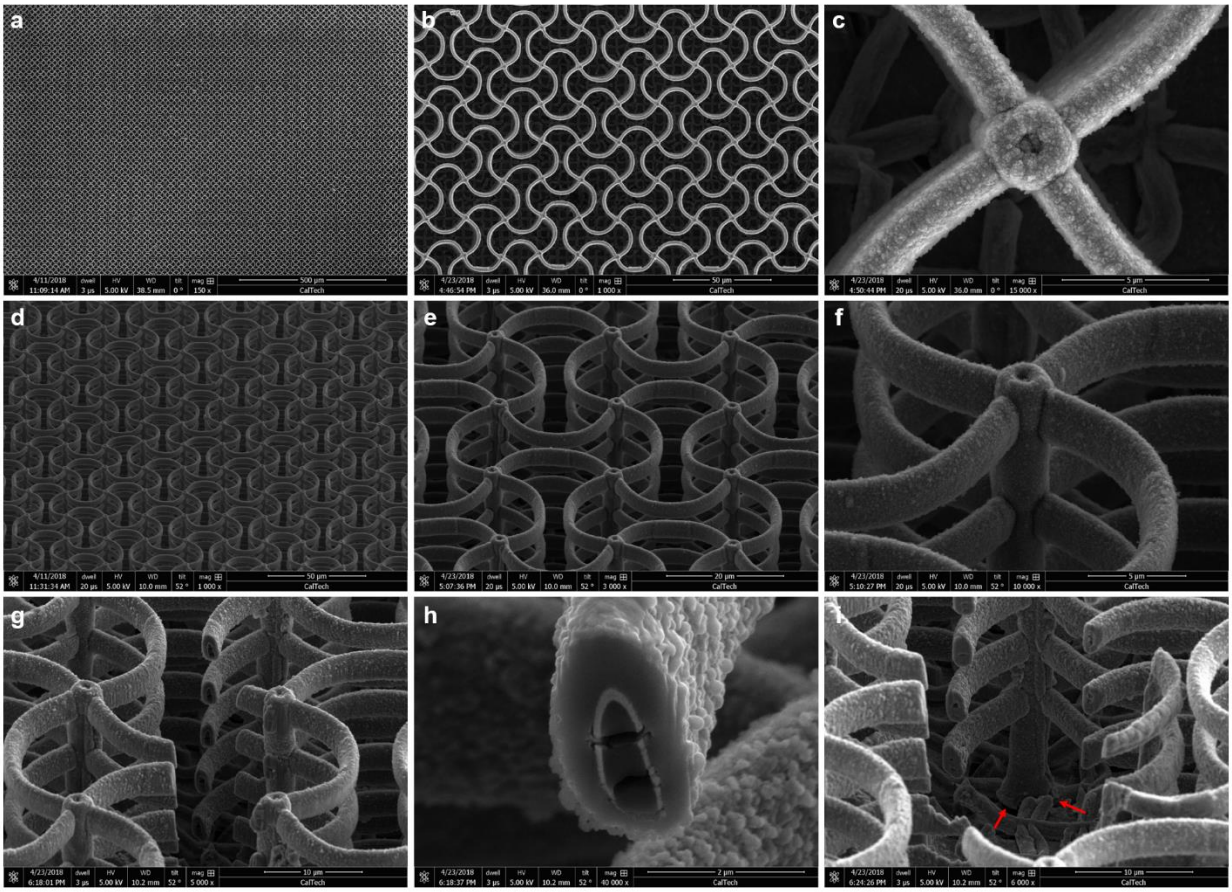

Figure 4.11 SEM images of representative Si microlattices after the 101th lithiation.

4.9 Coupled Chemo-Mechanical Finite Element Analysis of Individual Beams

To investigate the dynamic mechanical behavior of individual beams during lithiation-induced buckling, we employed a fully-coupled chemo-mechanical continuum finite element analysis (FEA) model developed by Di Leo et al. [131] This model accounts for transient and stress-dependent Li diffusion, large elastic-plastic deformations, and Li-concentration-dependent material properties during Si lithiation and delithiation. It was calibrated to experimental results from galvanostatic cycling of Si thin films on glass substrates [129,132] and was demonstrated to capture lithiation-induced deformations of hollow Si nanotubes [164] and Cu-Si core-shell nanolattices [87]. Fig. 4.12a shows a simulated beam, where a quarter of the geometry is discretized due to symmetry. The Si elements obey the constitutive model mentioned above; the Ni layer is prescribed an elastic-plastic behavior, and the polymer core a purely elastic behavior (see Appendix A). To mimic the inevitable fabrication imperfections that cause each beam to deviate from a perfectly straight one, we prescribe slightly different ramping rates of incoming Li flux on the two opposite external surfaces of the beam. Supplementary Video 9 summarizes the simulation results by showing the dynamic evolution of voltage, geometry and contours of local Li concentration and stresses during lithiation and delithiation. Fig. 4.12a presents progressive snapshots of the beam geometry with normalized Li concentration contours at three different times (t_1, t_2, and t_3). This chemo-mechanical model successfully captures the lithiation-induced buckling behavior and reproduces a voltage vs. state-of-charge (SOC) profile at C/6 comparable to experimental measurements (Fig. 4.12b). Fig. 4.12c shows contours of the σ_{zz} component of stress on the mid-span cross-section at t_1, t_2, and t_3 during lithiation and delithiation; Fig. 4.12d plots σ_{zz} vs. SOC at three different locations on the mid-span cross-section, where σ_{zz} is normal to the cross-section. These two plots reveal that during the early stage of lithiation at t_1, the beam elastically buckles with the presence of significant compressive stresses on the concave side of the buckled beam (point A) and tensile stresses on the convex side (point B). It is also apparent that the top of the beam (point C) experiences compressive stresses, which is consistent with the beam having a compressive axial load superimposed with a bending moment due to buckling. With the onset of plastic deformation as lithiation continues, stresses at all three locations become compressive and stay at a level close to the yield stress until lithiation is completed at t_2. During delithiation, the beam contracts and unbuckles significantly resulting in a large tensile stress developing at point A, a smaller tensile stress at point C and a slightly compressive stress at point

B, all of which increase until the end of delithiation at t_3. The development of large tensile stresses during simulated delithiation correlates well with experimentally observed fracture events at later stages of delithiation (Fig. 4.7b).

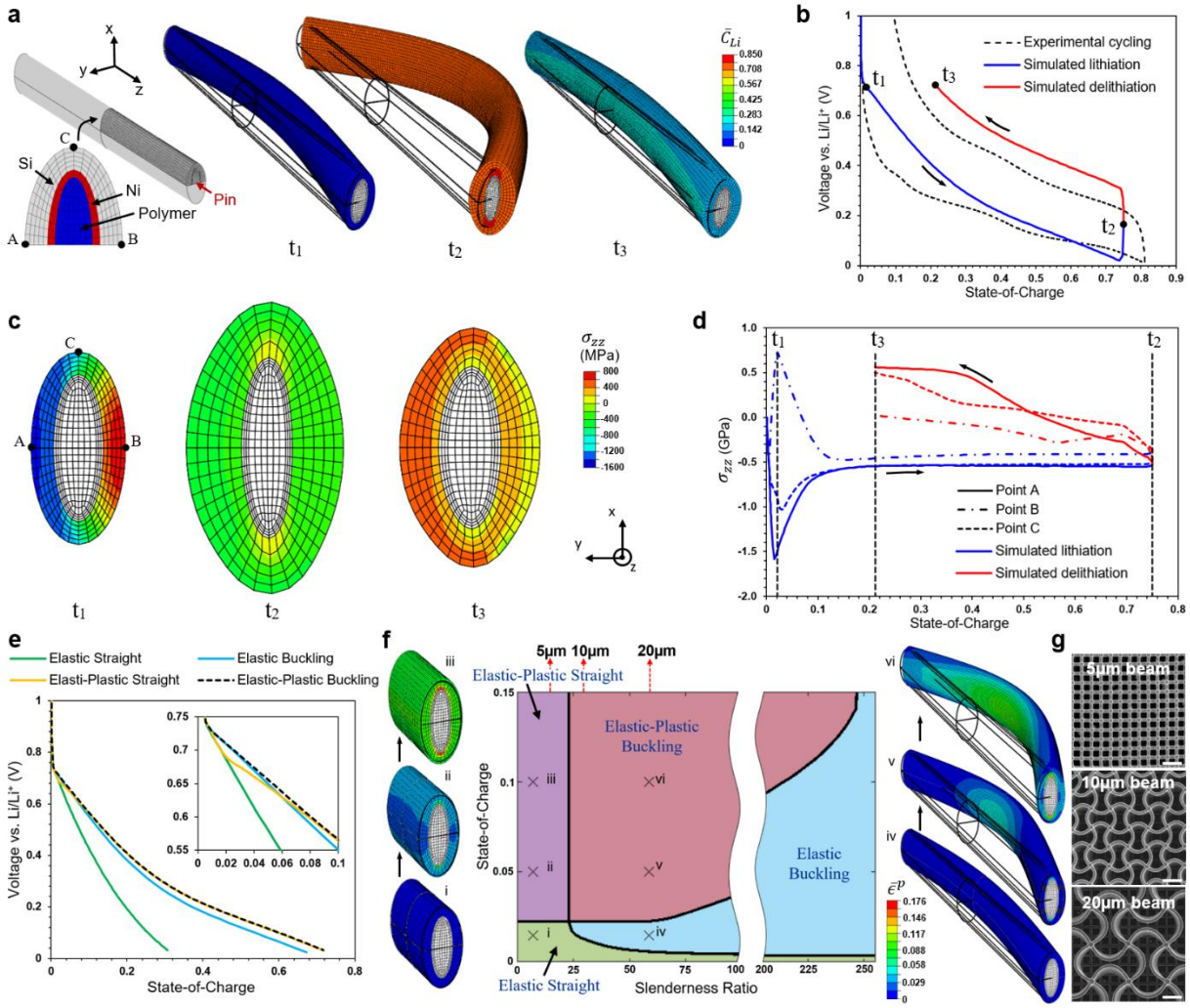

Figure 4.12 Simulation results generated by the coupled chemo-mechanical FEA model of an individual beam. (a) 3D mesh of a quarter of a polymer-Ni-Si beam with mirrored boundary conditions in the center and pinned boundary conditions at the end and simulated beam geometries at different times (t_1, t_2, and t_3) during lithiation and delithiation. Colored contours represent Li concentration normalized by the maximum possible molar concentration of Li in Li-Si alloys based on the theoretical specific capacity. (b) Simulated voltage vs. state-of-charge (SOC) profile during lithiation (blue) and delithiation (red) overlaid with an experimental voltage profile from the second cycle with a 1.5 V delithiation cutoff voltage at C/6 (dashed black). SOC is defined as the attained specific capacity normalized by the theoretical specific capacity. (c) σ_{zz} stress contours at t_1, t_2, and t_3 during lithiation and delithiation on the mid-span cross-section. (d) σ_{zz} stress vs. SOC evolution at three different locations (point A, B, and C) within the mid-span cross-section during lithiation and delithiation. (e) Voltage vs. SOC profiles of four different beam deformation mechanisms comparing their attainable state-of-charge at C/10. (f) Phase map of beam deformation mechanisms as a function of

slenderness ratio and SOC from the reduced-order model. Side: plastic strain contours of a stubby and a slender beam at different SOCs from the FEA model. (i-iii) is the progression of lithiation in a stubby beam at three SOCs, where buckling does not occur. (iv-vi) is the progression of lithiation in a slender beam at the same three SOCs, where elastic buckling precedes plastic deformation. This slender beam has the same dimensions as the horizontal beams in the experiments. Slenderness ratio of a beam is defined as the ratio of its length and its radius of gyration. (g) SEM images of lithiated Si microlattices with different horizontal beam lengths of 5 μm, 10 μm, and 20 μm, which demonstrate that only the 5 μm beam lattice did not buckle as predicted by the phase map with corresponding beam lengths labelled on the top axis in (f). Scale bars: 10 μm.

This coupled chemo-mechanical model demonstrates the interplay among different deformation mechanisms during lithiation and provides insights for lattice architecture design. Fig. 4.12e and Supplementary Video 10 compare the effects of four different beam deformation mechanisms on the lithiation voltage profiles: (1) straight elastic deformation, (2) straight elastic-plastic deformation, (3) purely elastic buckling, and (4) elastic-plastic deformation with buckling. Fig. 4.12e demonstrates that beam-based architectures that allow for buckling, plastic deformation, or the combination of the two could more than double the achievable state-of-charge at C/10 by reducing stresses during lithiation. Straight elastic-plastic deformation results in a slightly higher voltage than elastic buckling except for the short periods before and immediately after the onset of yielding in the beginning of lithiation (inset of Fig. 4.12e). The complete model (elastic-plastic deformation with buckling as plotted in the dashed black line) predicts a voltage profile that follows the trend of the highest voltage for a given SOC. This reveals that the interplay among different deformation mechanisms is dynamic, with the most efficient stress relief mechanism governing the voltage profile during different stages of lithiation. Furthermore, the propensity for buckling instabilities is dictated by the slenderness ratios of the beams and contributes to the dominant deformation mechanism at different stages of lithiation. This is visualized by the phase map of beam deformation mechanisms at different slenderness ratios and SOCs in Fig. 4.12f, which is predicted by a reduced-order chemo-mechanical model. This model is based on assuming a homogeneous concentration field and a uniaxial state of stress and solving for the corresponding behavior of an elastic pin-pin beam undergoing lithiation-induced buckling (see Appendix B). The phase map readily demonstrates that a stubby beam will first deform elastically and then elastic-plastically without buckling; a slender beam with the same cross-section would first deform elastically and then buckle elastically before yielding (Supplementary Video 11). At very large slenderness ratios, it is possible for a beam to buckle elastically only, but local plastic deformation

due to inhomogeneous stresses might still occur, which cannot be captured by the reduced-order model. Finally, we experimentally corroborated the phase map by fabricating and lithiating Si microlattices with different horizontal beam lengths. SEM images in Fig. 4.12g indicate that the transition between straight elastic-plastic deformation and elastic-plastic buckling happens between 5 μm and 10 μm in beam length, as predicted by the reduced-order model.

4.10 Role of Defects in Cooperative Buckling and Domain Formation

Experiments show that cooperative buckling among neighboring beams during lithiation leads to the formation of identical sinusoidal buckling patterns within multiple domains; geometric incompatibilities between separate domains induce Mode-II buckling of beams at the domain boundaries. We hypothesize that local defects influence the buckling configuration of each domain. Two types of defects in as-fabricated Si microlattices are identified: (1) fabrication inaccuracies such as non-uniform film thickness (Fig. 4.2e) and node misalignments during lattice stitching in two-photon lithography (Fig. 4.13c), and (2) random defects such as surface roughness and initial beam curvature due to residual stresses within the Ni and Si layers (Fig. 4.13d). To investigate the role of defects in cooperative buckling, we constructed a 2D chemo-mechanical FEA model of an extended unit cell with appropriate boundary conditions and introduced specific defects, which in simulations are defined as a small pre-existing curvature with a mid-span displacement of 100 nm (Supplementary Video 12).

Fig. 4.13a, b show an overlay of FEA simulations and SEM images of typical cooperatively buckled beams within a domain (Fig. 4.13a) and distorted beams around a domain boundary (Fig. 4.13b). The red-colored beams on the left side of the extended unit cell, illustrated in the inset of Fig. 4a are prescribed coherent defects that would favor node 1 to rotate counterclockwise and node 2 clockwise. The FEA simulation (colored contours in Fig. 4.13a) conveys that the nodes rotate as prescribed, and coherent buckling propagates to the remaining defect-free beams in the extended unit cell through coupling of beams at each node, which drives node 3 to rotate clockwise and node 4 counterclockwise. In this case, all nearest-neighbor nodes rotate in mutually opposite directions, and all beams in the extended unit cell form a coherent sinusoidal pattern with pairwise opposite concavity (Fig. 4.13a). In the second case (Fig. 4.13b), additional defects are prescribed to favor node 3 and 4 to rotate in the same directions as node 1 and 2 respectively, as illustrated by the blue-colored beams in the inset of Fig. 4.13b. The FEA simulation predicts the two defect-

free beams in the center of the extended unit cell to deform via Mode-II buckling due to geometric frustration, which has a higher elastic energy as quantified by the reduced-order model (see Appendix B). These simulated responses to prescribed defects agree with experimental observations, as evidenced by the underlying SEM images of typical buckling patterns within and between domains (Fig. 4.13a, b), with one notable distinction that the vertical posts near domain boundaries in the experiments leaned slightly off-center as a result of imbalanced forces imposed by the horizontal beams. These simulations reveal that fabrication defects influence the nucleation of buckling domains locally during lithiation. The short-range cooperative interactions among the buckled beams drive the propagation of the ordered domains throughout the lattice. When separate domains impinge on one another, they either coalesce to form larger domains if compatible or generate domain boundaries if mismatched, a process similar to the island growth model of metal thin films [165].

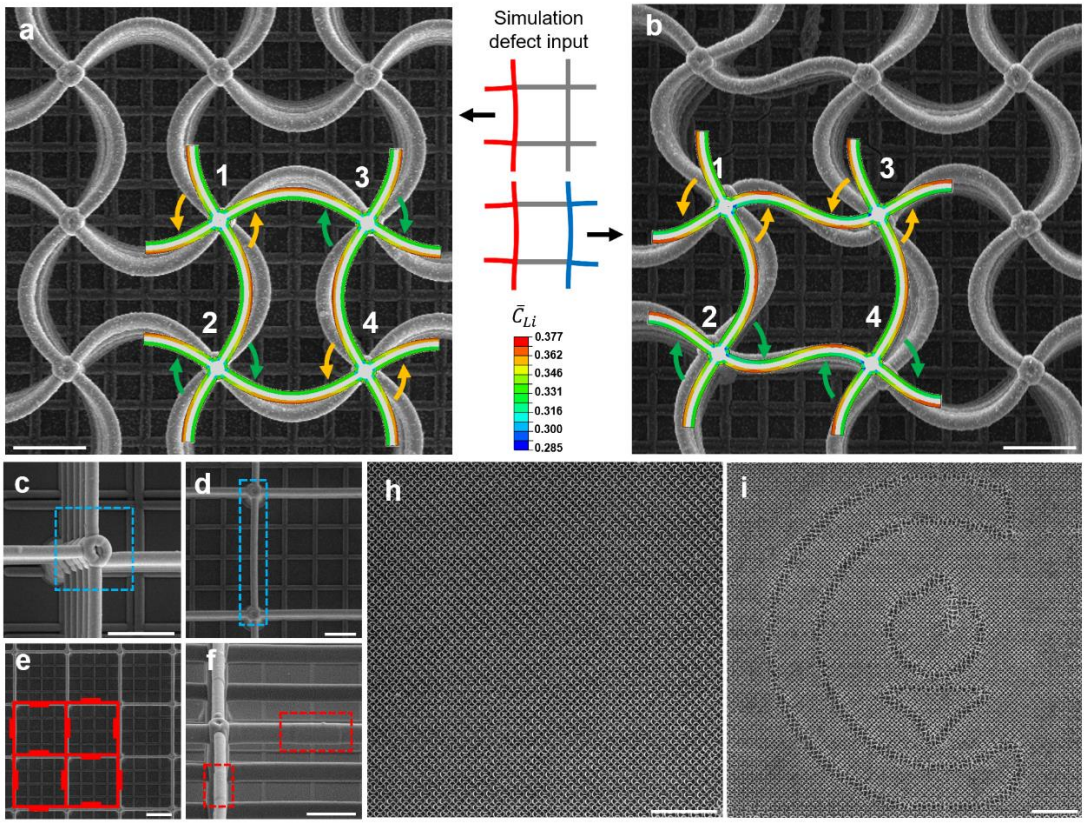

Figure 4.13 Role of defects in domain formation by cooperative buckling. (a) FEA simulation of a 2D extended unit cell with coherent prescribed defects, illustrated in the center inset in red, overlaid onto an SEM image of a typical sinusoidal pattern formed within a single domain. (b) FEA simulation of a 2D extended unit cell with incompatible prescribed defects, illustrated in the center inset in red and blue, overlaid onto a

SEM image of a typical domain boundary. Colored contours in (a, b) represent normalized Li concentration. (c-f) SEM images of typical defects in microlattices: (c) stitching misalignment at a node, (d) pre-existing beam curvature caused by residual stresses, and (e, f) periodically arranged artificial defects of 5 μm-long, 100 nm-thick added patch on one side of the polymer core of the horizontal beams, with Ni and Si layers following the morphology. (h) SEM image of a single-domain sinusoidal lattice formed as a result of defect engineering. (i) SEM image of a Caltech icon outlined by domain boundaries that emerged upon lithiation by pre-designing artificial defects. Scale bars: (a, b, e) 10 μm, (c, d, f) 10 μm, (h, i) 200 μm

Building upon the uncovered mechanism of defect-governed domain formation in Si microlattices, we designed and incorporated a periodic arrangement of artificial defects in Si microlattices (Fig. 4.13e). Each artificial defect was a 5 μm-long, 100 nm-thick added patch on one side of the polymer beam during two-photon lithography (Fig. 4.13f). This is achieved by writing another 5 μm-long beam in the middle of the horizontal beam 100 nm off the center axis so the majority of the two beams overlap producing the 100 nm-thick patch on one side. The subsequently deposited Ni and Si layers follow the surface morphology of the polymer beams. Such artificial defects are demonstrated to cause the beams to buckle towards the side without the artificial defect. Within each unit cell, one pair of opposite beams have artificial defects facing towards each other, causing the beams to buckle away from each other; the other pair of opposite beams have artificial defects facing away from each other, causing the beams to buckle towards each other. Such periodic artificial defects on all layers of the horizontal beams or just the topmost layer overwhelm existing fabrication defects and control buckling directions deterministically. With the help of artificial defects, we can make lithiated Si microlattices in a single domain without any domain boundaries (Fig. 4.13h) or program any pattern to be formed by the domain boundaries (Fig. 4.13i). For the latter case, different sides of the designated domain boundaries are implanted with incompatible artificial defects of the two bistable domain phases and the beams at the domain boundaries are artificial-defect-free so they are forced to deform via Mode-II buckling due to geometric frustration. For example, we processed an image of a Caltech icon (Fig. 4.14a) into a domain map (Fig. 4.14b), and implanted the corresponding artificial defects in a Si microlattice during two-photon lithography. Upon lithiation, a pattern of the Caltech icon emerged spontaneously (Fig. 4.14c). Supplementary Video 8 (at a playing speed of 300X) demonstrates that pre-designed artificial defect could precisely program the domain boundaries to form any pattern. In this case, a Caltech icon emerged during discharge when the Si microlattice-Li cell was supplying current to a 3000 Ω resistor load.

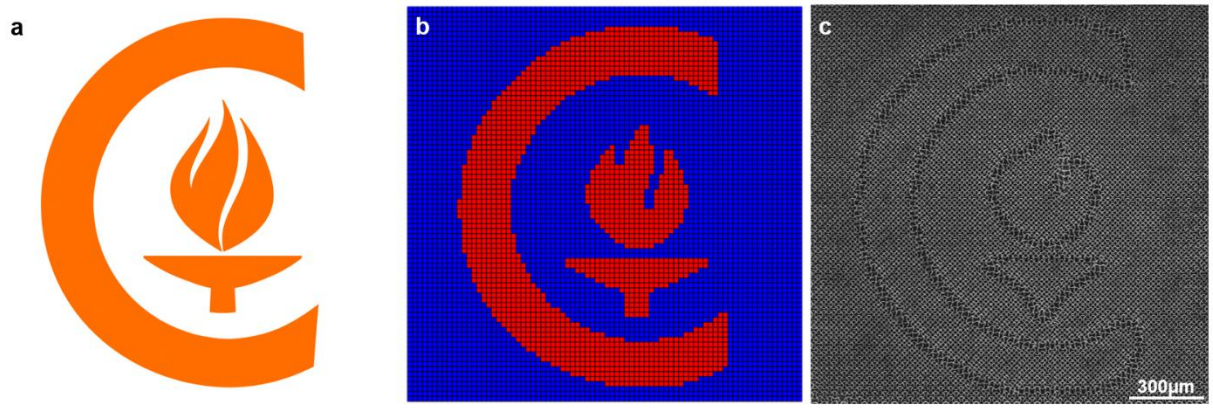

Figure 4.14 (a) Image of a Caltech icon. (b) Processed domain map based on the Caltech icon. (c) SEM image of programed domain boundaries of a Caltech icon shape by pre-designing artificial defects.

4.11 Lithiation Rate Dependence of Domain Size Distribution

To probe into the dynamics of domain formation, we lithiated Si microlattice samples at different rates. SEM images of domain maps formed at different lithiation rates are processed digitally to analyze the correlation between node rotations. As shown in Fig. 4.15a-d, we traced through the Mode-II buckled beams shown in SEM images at the domain boundaries. Then we took the tracing layer of the image (Fig. 4.15d) and used MATLAB to convert it into an 80 × 80 array of nodes showing the distribution of the bistable domains as shown in Fig. 4.15e: within each blue or red domain, all nearest-neighbor nodes rotate in mutually opposite directions and all beams deformed by Mode-I buckling; across the boundary between a red and a blue domain, the interfacing nodes rotate in the same directions with the adjoining beams deformed by Mode-II buckling. Such mathematical representation of the domain map can be further processed to an equivalent array of node rotations s_i of +1 and -1 representing the clockwise and counter-clockwise rotation of the nodes shown by the red and blue square pixels in Fig. 4.15f. Due to the antiferromagnetic-like interactions among the nodes, two nearest neighboring nodes are in the same domain if and only if they have opposite directions of rotation. From this array, we can calculate the correlation [166,167] of pairwise node rotation directions as a function of their separation in terms of nearest integer number of unit cells $C(r) = \langle(-1)^r \cdot s_i \cdot s_{i+r}\rangle$, where $\langle \dots \rangle$ denotes an average for all node pairs with a separation of r. The decay of this correlation function with respect to distance of separation is characteristic of the average domain size in each domain map, where a faster decay indicates a smaller average domain size.

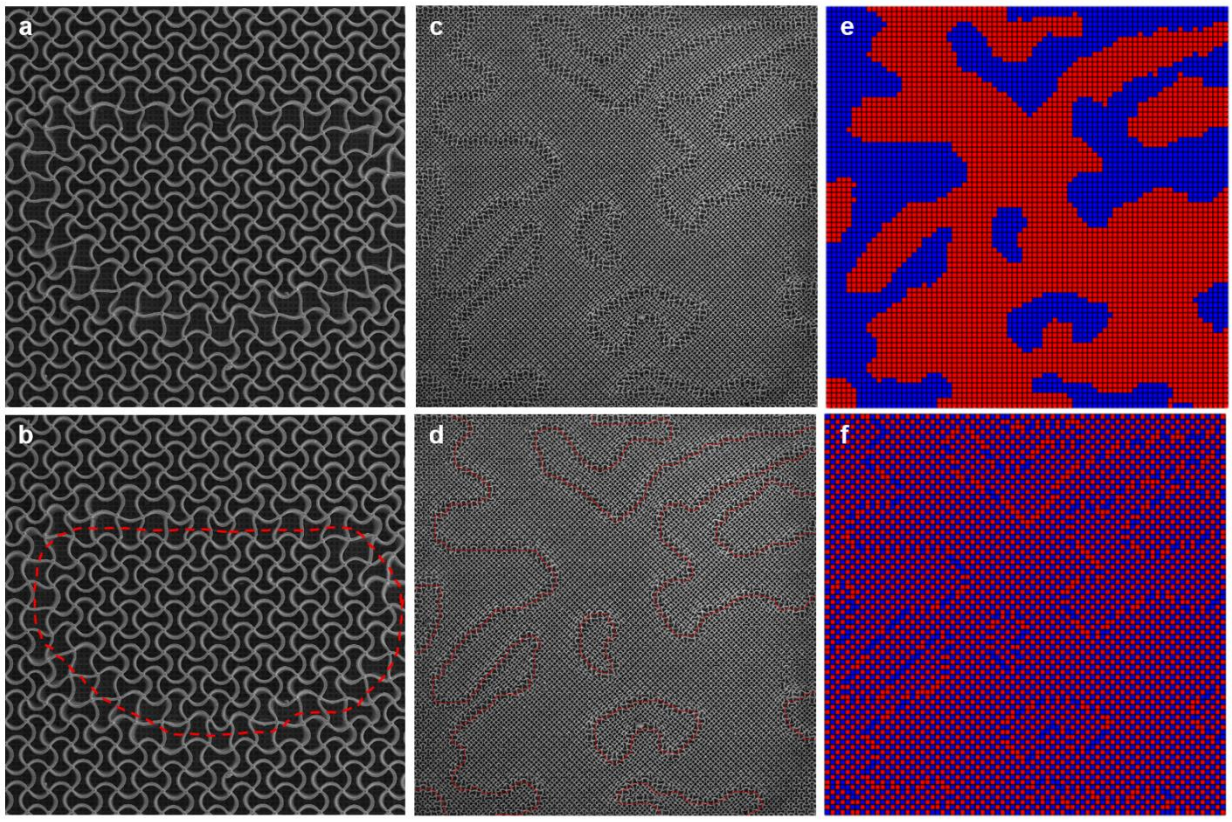

Figure 4.15 (a) SEM image of a representative domain. (b) Tracing of the domain boundary in (a) through the Mode-II buckled beams. (c) SEM image of a representative lithiated Si microlattice sample with bistable domains. (d) Tracing of domain boundaries on the original SEM image. (e) An example of digitally processed domain map with red and blue square pixels indicating each node being in one of the two bistable domain phases. (f) An example of digitally processed node rotation map with red and blue square pixels indicating clockwise and counterclockwise rotation of each node.

Fig. 4.16a-f compile representative domain maps at five different lithiation rates with the original SEM images. Two samples are shown for C/6 to show nominally identical Si microlattices at the same lithiation conditions produce different domain patterns. Despite the arbitrary shapes of the domain maps, a clear trend of a higher lithiation rate leading to smaller domains can be identified. To quantify the average domain size, we computed the correlation function for each domain map. Fig. 4.16g, h are correlation functions at different lithiation rates with two samples per rate at different zooms, which demonstrates despite the significant difference in the shapes of domains across the two samples at the same lithiation rate, the statistical correlation functions are comparable. Fig. 4.16i shows the average correlation functions at different lithiation rates with a clear trend of a higher lithiation rate leading to a faster decay in correlation and therefore a smaller average domain size. Fig. 4.17 presents another set of experimental results for lithiation conducted

at an elevated temperature of 37°C. It shows a qualitatively similar result of a higher lithiation rate leading to a smaller correlation length and therefore smaller domains. However, compared with Fig. 4.16, the domains are larger at the same lithiation rates at 37°C than those at room temperature are. For each averaged correlation function in Fig. 4.16i and Fig. 4.17f, we fitted an exponential decay function $C(r) = A \cdot \exp\left(-\frac{r}{\xi}\right)$ in MATLAB to calculate the statistical correlation length ξ, characteristic of the average domain size, for each lithiation rate. The first ten points in each correlation function plot (distance $r \leq 9$) are used for the fitting due to the large statistical noises at larger distances where the correlation is low.

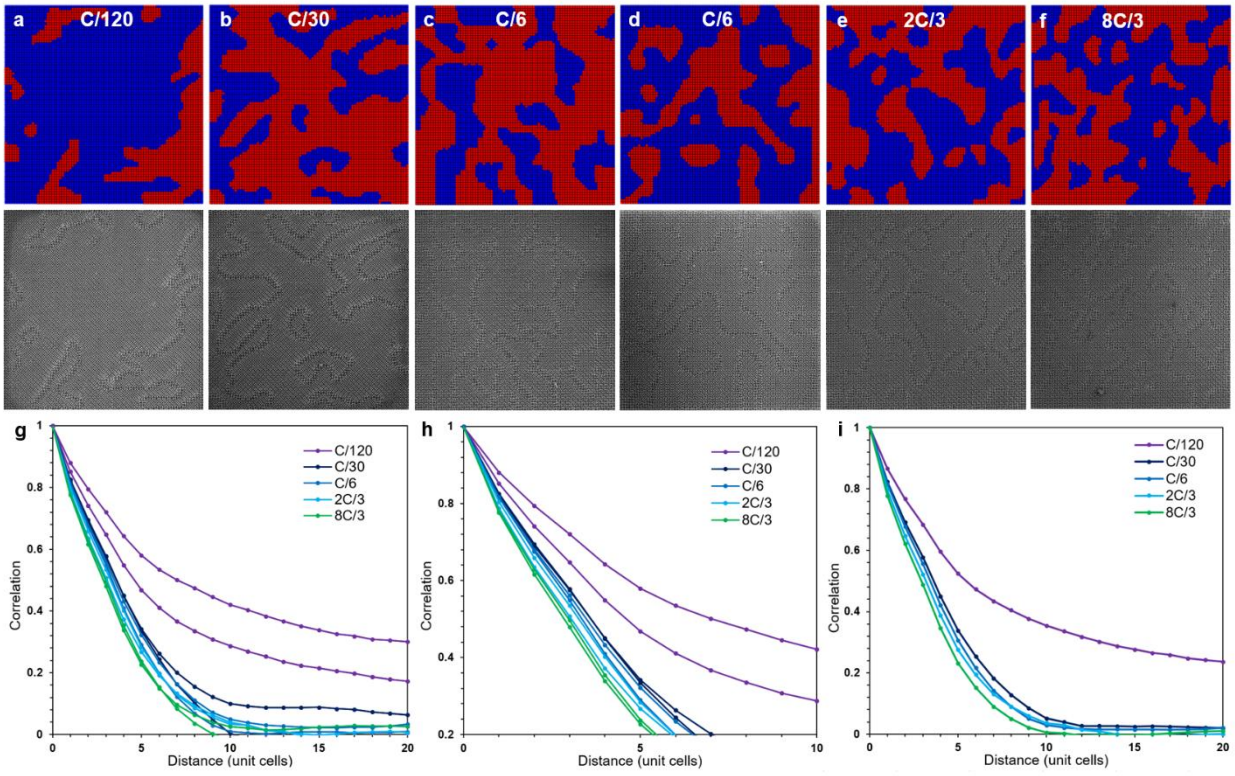

Figure 4.16 (a-f) Representative domain maps and SEM images of Si microlattice samples lithiated at different rates at room temperature. (g, h) Correlation functions at different lithiation rates with two samples per rate at different zooms at room temperature. (i) Averaged correlation function at different lithiation rates from two samples per rate at room temperature.

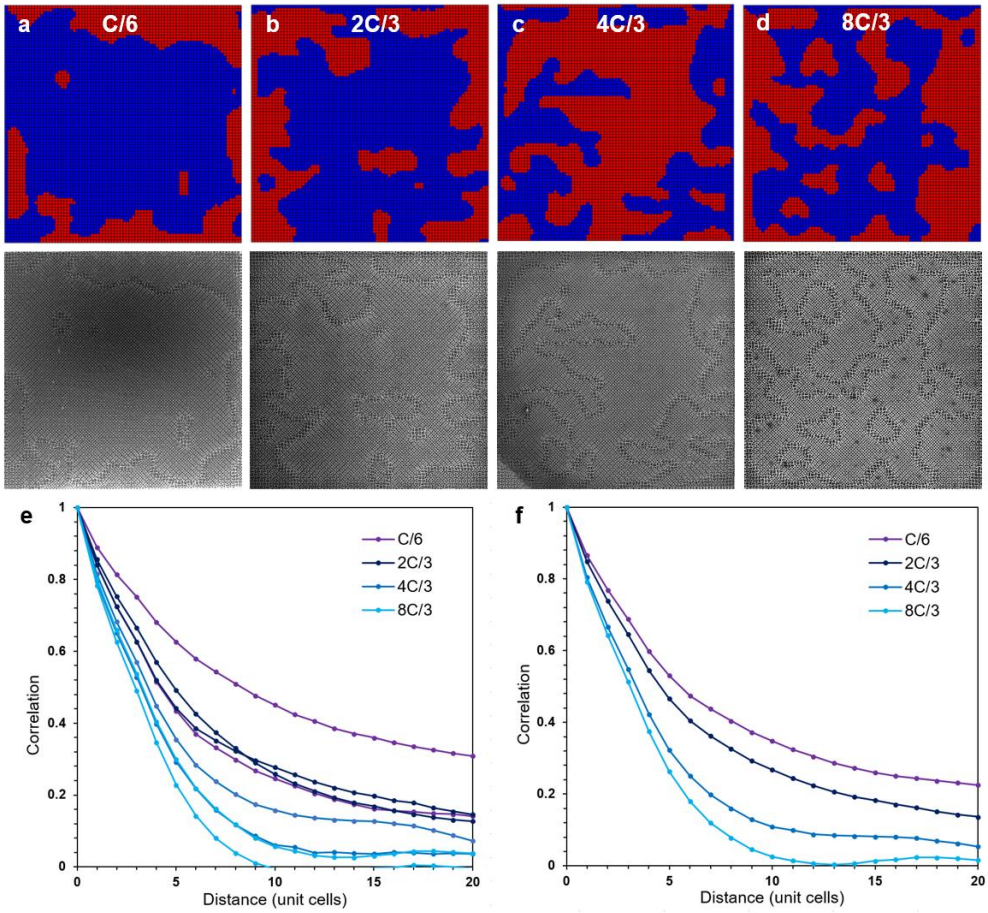

Figure 4.17 (a-d) Representative domain maps and SEM images of Si microlattice samples lithiated at different rates at 37°C. (e) Correlation functions at different lithiation rates with two samples per rate at 37°C. (f) Averaged correlation function at different lithiation rates from two samples per rate at 37°C.

4.12 Statistical Mechanics Analysis of Domain Formation Dynamics

Fig. 4.18i plots the relationship between lithiation rate and correlation length ξ at room temperature (blue) and at 37°C (red). For both temperatures, correlation length decreases as lithiation rate increases, while at 37°C correlation lengths shift larger at the same lithiation rates than those at room temperature. To understand this lithiation rate-dependent domain formation process, we studied the analogy between lithiation-induced cooperative buckling and the square-lattice antiferromagnetic Ising model [166–170]. The simplified statistical mechanics model takes into consideration the following essential aspects: (1) mechanical coupling between neighboring nodes, (2) fabrication defects, (3) energy fluctuations intrinsic to chemical reactions, and (4) the rate of lithiation and deformation. In this conceptual framework, we represent the energy of each microlattice as

$$E(s) = -\sum_{\langle i,j \rangle} J \cdot s_i s_j - \sum_i h_i \cdot s_i \qquad (1)$$

where J is the coupling between nearest-neighbor node rotations, h_i represents the influence of fabrication defects at each node, and $\langle i,j \rangle$ denotes that nodes i and j are nearest neighbors. Fig. 4.18f shows that the coupling between two nearest-neighbor nodes to rotate in opposite directions, as indicated by the elastic energy difference between Mode-I and Mode-II buckling of the adjoining beam (yellow area), increases gradually from zero to a finite value as lithiation progresses, and so does the energy contribution of a fabrication defect (green area). In addition to the mechanical interactions described in Eq. (1), we postulate that there exists an energy fluctuation Q_{EC} in the local electrochemical environment coarse-grained onto each node. Q_{EC} can be understood as the result of a stochastic perturbation of the competing force balance on the two opposite surfaces of a bistable beam due to local lithiation nucleation events before it buckles irreversibly into a particular direction (see further discussion in Section 4.14).

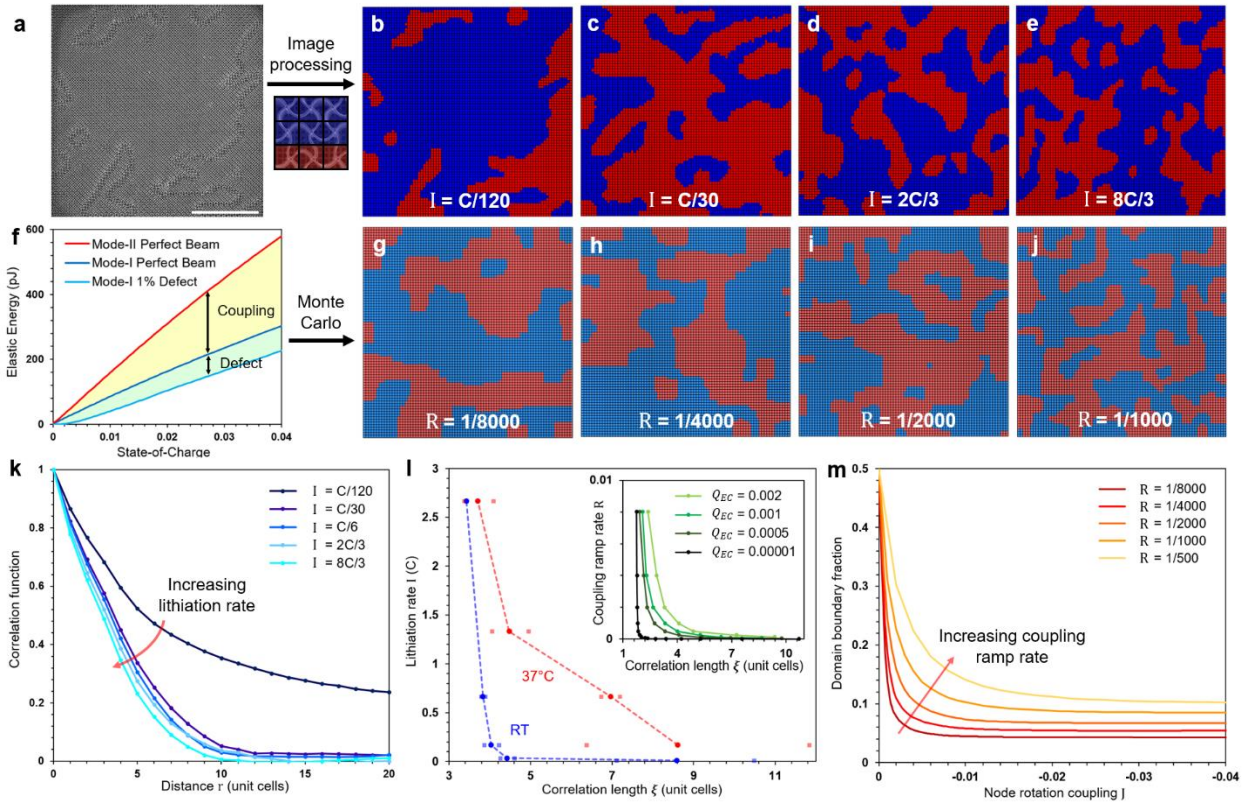

Figure 4.18 Statistical mechanics analysis of bistable domain formation. (a) SEM image of a Si microlattice lithiated at C/120, with the illustration of how the domain map in (b) is generated from (a). Scale bar: 500 μm. (b-e) Computer-processed domain maps of Si microlattices lithiated at four progressively higher rates from

C/120 to 8C/3 at room temperature. Each square pixel in these maps represents a node in the Si microlattice, and interfaces between red and blue pixels correspond to the Mode-II buckled beams that form domain boundaries. (f) Elastic energy calculated from the reduced-order chemo-mechanical model as a function of state-of-charge for three beam geometries: a perfect beam undergoing Mode-II buckling (red), a perfect beam undergoing Mode-I buckling (blue), and a beam with a 1% defect (represented as a slight curvature) undergoing Mode-I buckling (light blue). The difference in elastic energy between Mode-I and Mode-II buckling for a perfect beam (yellow area) defines the coupling of neighboring nodes that favors opposite node rotations. The difference in elastic energy between a perfect beam and a beam with 1% defect undergoing Mode-I buckling (green area) represents the energy contribution of the fabrication defect. (g-j) Representative domain maps generated by Monte Carlo simulations for four progressively higher node coupling ramp rates from 1/8000 to 1/1000 with an electrochemical energy fluctuation $Q_{EC} = 0.001$. (k) Statistical correlation function $C(r)$ of pairwise node rotations as a function of their separation distance r for five different lithiation rates that shows that a higher lithiation rate leads to the formation of smaller domains for experiments conducted at room temperature. (l) Variations in correlation length ξ with lithiation rate I for experiments conducted at room temperature (blue) and at 37°C (red). Circular data points connected by dotted lines are fitted from correlation functions that averaged two samples tested at the same condition. Individually fitted correlation lengths for each sample are also shown as square data points. Inset: simulated variations in correlation length ξ with node coupling ramp rate R in Monte Carlo simulations for four different electrochemical energy fluctuations Q_{EC}. (m) Fraction of domain boundaries, represented by the ratio of Mode-II buckled beams out of all beams, as a function of node rotation coupling J for five different coupling ramp rates R, which conveys that a higher ramp rate leads to a higher stabilized domain boundary fraction indicative of smaller domains.

Monte Carlo simulations of the statistical mechanics model are implemented on a square lattice with random initial node rotations (see details in Section 4.13). We gradually turn on node rotation coupling J from zero to a normalized value of -1, as well as the influence of fabrication defects h_i from zero to a normal distribution with mean of 0 (i.e. equal probability for preference in either direction) and a standard deviation of 0.125, by N_{incr} increments with a linear ramp rate defined as $R = 1/N_{incr}$. At each increment, we evolve the system by a total of 6400 Monte Carlo steps (1 Monte Carlo step/node) using the Metropolis algorithm. In each Monte Carlo step, a random node is chosen and flipped: if the resulting system energy change $\Delta E < 0$, the trial is accepted; if $\Delta E > 0$, the trial is accepted with a probability $P = \exp\left(-\frac{\Delta E}{Q_{EC}}\right)$. Fig. 4.18g-j shows representative domain maps generated by Monte Carlo simulations with $Q_{EC} = 0.001$ at progressively higher coupling ramp rates that result in progressively smaller domains. Fig. 4.18m shows that as the coupling J is turned on in each lattice, the fraction of domain boundaries drops rapidly due to the growth of domains, and stabilize when J is relatively large compared with Q_{EC} but still orders of magnitude smaller than its final value of -1. Fig. 4.18m also shows that at a slower coupling ramp

rate R, domain boundary fraction stabilizes at a lower value indicative of larger domains. The relationship between coupling ramp rate R and correlation length ξ is shown in the inset of Fig. 4.18l for four different Q_{EC} from 0.00001 to 0.002, where each ξ is fitted from correlation functions that average ten simulations. It reveals that higher coupling ramp rates in Monte Carlo simulations leads to smaller correlation lengths for each Q_{EC}, while a higher Q_{EC} shifts this relation towards larger correlation lengths. Extensive simulations with different $Q_{EC} \ll 1$ and $h_i < 1$ are provided in the Fig. 4.19 in Section 4.13 with the same qualitative trends.

The proposed statistical mechanics framework shows reasonable agreements with our experimental results (Fig. 4.18l) and provides valuable insights about the dynamic domain formation process. Monte Carlo simulations reveals that a very small electrochemical energy fluctuation plays an important role in domain growth when the node rotation coupling is turned on gradually. In the Si microlattices undergoing lithiation, the energy fluctuations caused by electrochemistry are orders of magnitude smaller than the stored elastic energy in the beams. In this regime of $Q_{EC} \ll J_{final}$, the final coupling strength becomes irrelevant to domain formation because domain boundaries stabilize at J such that $Q_{EC} < J \ll J_{final}$ (Fig. 4.18m), and only the coupling ramp rate R with respect to Q_{EC} governs the formed domain sizes (Fig. 4.19d). At a lower coupling ramp rate, the system effectively stays longer in an environment where the energy fluctuations are still relevant and therefore relaxes into a lower energy state with larger domains. Increasing the electrochemical energy fluctuations also allows the domains to grow larger by extending the range of coupling strength subject to the energy fluctuations. This rate-dependent interplay between mechanical node rotation coupling and energy fluctuations during the initial stage of lithiation-induced cooperative buckling is impossible to observe experimentally. The discussion here provides a new perspective to utilize statistical mechanics tools to explain and predict such dynamic response of architected materials with defect- and fluctuation-sensitive instabilities. It highlights the intriguing similarities between engineered architected materials and classical materials so that we could potentially draw inspiration from established theories such as phase transformations and metallurgy (e.g., annealing and quenching to control grain size) to guide architected material design.

4.13 Implementation and Details of Monte Carlo Simulations

To understand domain formation dynamics more deeply, we studied the analogy between lithiation-induced cooperative buckling and the square-lattice antiferromagnetic Ising model. Monte Carlo simulations of the Ising model are implemented in MATLAB based on the "Ising Model and Metropolis Algorithm" script provided by MathWorks Physics Team (version 1.2.0.0, available at https://www.mathworks.com/matlabcentral/fileexchange/62194-ising-model-and-metropolis-algorithm). Using the conceptual framework of the Ising model, we represent the energy of each microlattice consisting of an 80 × 80 array of nodes as

$$E(s) = -\sum_{\langle i,j \rangle} J \cdot s_i s_j - \sum_i h_i \cdot s_i$$

where $s_i = \pm 1$ is the direction of node rotation, J is the energy coupling between nearest-neighbor node rotations, h_i represents the influence of fabrication defects at each node, and $\langle i,j \rangle$ denotes nodes i and j are nearest neighbors. Fig. 4.18f compares the evolution of elastic energy of a perfect beam undergoing Mode-I (blue) and Mode-II buckling (red), as estimated by the reduced-order chemo-mechanical model. The difference between the two curves (yellow) reflects the energy penalty of two nearest-neighbor nodes to co-rotate in the same direction, since Mode-II buckling has a higher elastic energy. Fig. 4.18f also shows the difference in elastic energy between a perfect beam (blue) and a beam with a 1% defect (represented as a slight curvature) (light blue), both undergoing Mode-I buckling, which represents the energy contribution of the fabrication defect (green). Fig. 4.18f shows that the coupling between nearest-neighbor nodes, J, and the energetic influence of defects, h_i, both increase from zero to finite values with the progression of lithiation, *a concept that is essential to describe and explain domain formation dynamics*. Based on our understanding of lithiation-induced cooperative buckling through experiments and mechanical simulations, we implement kinetic Monte Carlo simulations in the following way.

(1) In the initial state of the simulation, each node is assigned a random rotation $s_i = \pm 1$. The node rotation coupling, $J = 0$, and the energy influence of defects at each node, $h_i = 0$. This represents the system state before any lithiation-induced deformation of Si microlattices occurs.

(2) In the final state of the simulation, we set the node rotation coupling J to -1 that represents the antiferromagnetic-like interactions between neighboring nodes that favor opposite rotations. The

final state in these simulations does not correspond to the completion of the lithiation process at the cutoff voltage in the experiments; rather, it represents a point in the lithiation process at which the node rotations/the beam buckling directions become irreversible due to, for example, the onset of plastic deformation. In this final state, we set the influence of fabrication defects h_i to a normal distribution $\mathcal{N}(0, 0.125^2)$ with a mean of 0 (i.e. equal probability of preference for either direction) and a standard deviation of 0.125. This defect distribution corresponds to a relatively small random defect field compared with the coupling strength. As shown later in this discussion, the exact value of the standard deviation does not qualitatively change the results of the Monte Carlo simulations.

(3) In between the initial and the final state, we linearly ramp up both J and h_i by N_{incr} incremental steps with the ramp rate defined by $R = 1/N_{incr}$. For each simulation, the final defect field is generated based on the normal distribution $\mathcal{N}(0, 0.125^2)$ in the beginning of the simulation, and individual defect h_i at each node is ramped linearly to its final value. At each increment, we run 6400 Monte Carlo steps using the Metropolis algorithm (1 Monte Carlo step/node). At each Monte Carlo step, a single random node is first chosen and flipped: if the resulting system energy change $\Delta E < 0$, the trial is accepted; if $\Delta E > 0$, the trial is accepted with a probability $P = \exp\left(-\frac{\Delta E}{Q_{EC}}\right)$. In this formulation, Q_{EC} is the energy fluctuation in the local electrochemical environment coarse-grained onto the unit cell surrounding each node, which can be understood to be a result of the stochastic perturbation of the competing force balance on the two opposite sides of a bistable beam caused by local lithiation nucleation events before it buckles irreversibly into a particular direction. We set the initial electrochemical energy fluctuation level as $Q_{EC} = 0.001$, and we will discuss Q_{EC} further at the end of this section. The edges of the 80 × 80 array of nodes are treated as free edges with no periodic boundary conditions to emulate the lack of interactions between opposite edges in the Si microlattices.

For each condition, we run ten separate simulations with individually generated random defect fields following the same distribution and then take an average of the correlation functions and the domain boundary fraction vs. node rotation coupling J relations. Fig. 4.18g-j shows representative domain maps generated by Monte Carlo simulations with $Q_{EC} = 0.001$ at progressively higher coupling ramp rates that result in progressively smaller domains. Fig. 4.18m shows that as the coupling J is turned on, the fraction of domain boundaries drops rapidly due to the growth of

domains, and stabilizes when J is relatively large compared with Q_{EC} but still less than 5% of its final value of -1. Fig. 4.18m also shows that at a slower ramp rate R, the domain boundary fraction stabilizes at a smaller J and reaches a lower value indicative of larger domains. The relationship between coupling ramp rate R and correlation length ξ is shown in the inset of Fig. 4.18l for four different Q_{EC} (0.00001, 0.0005, 0.001, and 0.002). It reveals that higher coupling ramp rates in Monte Carlo simulations lead to smaller correlation lengths for each Q_{EC}, and that a higher Q_{EC} shifts this relation towards larger correlation lengths.

Fig. 4.18l compares the Monte Carlo simulation results directly to the experimental lithiation results. On the experimental side, this plot demonstrates that for both room temperature and an elevated temperature of 37°C, the correlation length decreases as lithiation rate increases, while at 37°C the lithiation rate-correlation length relation shifts towards larger correlation lengths than those at room temperature. Therefore, Fig. 4.18l indicates that the experimental results and the Monte Carlo simulations are in good qualitative agreements. The correlation length decreases similarly with the increase of both the lithiation rate and the coupling ramp rate. Increasing the temperature in the experiments or prescribing larger electrochemical energy fluctuations in the simulations would both shift the rate-correlation length relation towards larger correlation lengths.

Some differences between the experimental results and the Monte Carlo simulations are present. First, in the Monte Carlo simulations the domains are able to reach smaller sizes with a shorter correlation length at high coupling ramp rates. We have not observed this in experiments because of the additional bending distortion of the vertical posts that surround the domain boundaries, which cannot be accounted for in the Monte Carlo simulations. These distortions effectively create additional energy penalty at the domain boundaries that depends on the radius of curvature of the domain boundaries and renders smaller domains unfavorable. Another contribution that cannot be accounted for in the simulations is that at very high lithiation rates, the electrochemical reaction mechanism may not be identical to that for lower lithiation rates, for example in cases where Li ion diffusion inside the electrolyte might become a rate-limiting factor. Second, in the experiments, we observe a stronger edge effect at low lithiation rates due to the additional distortion at the edges resulting from the slight shrinking of the polymer scaffolds during development and the mechanical boundary conditions (Fig. 4.3). The sample-to-sample variation of correlation length at low lithiation rates is greater due to such edge effects as well as larger sampling error when

domains are bigger within the same lattice. Meanwhile, at low lithiation rates, side reactions due to impurities inside the electrolyte also play a relatively more dominant role, which could influence the reaction mechanism.

We would like to emphasize that the analogy between lithiation-induced cooperative buckling in Si microlattices and the simulated antiferromagnetic Ising model is aimed to qualitatively explain the phenomenon of stochastic domain formation and its dependence on lithiation rate. This model is simplified, but it captures the essential aspects of lithiation-induced cooperative buckling: (1) mechanical coupling among each pair of neighboring nodes, (2) fabrication defects, (3) energy fluctuations that are intrinsic to chemical reactions, and (4) the rate of lithiation and deformation. Monte Carlo simulations show that even a very small electrochemical energy fluctuation plays an important role in domain growth when the mechanical coupling is *gradually turned on*. At a lower coupling ramp rate, the system remains longer in an environment where the energy fluctuations are relevant and therefore relaxes into a lower energy state characterized by larger domains. Meanwhile, increasing the electrochemical energy fluctuations allows domains to grow larger by extending the range of coupling strength subject to energy fluctuations. In the simulations, we varied the energy fluctuations Q_{EC} from 0.00001 to 0.002, and the defect distributions h_i from a standard deviation of 0.05 to 0.2, and found that these parameter spans did not qualitatively change the results, as shown in Fig. 4.19a-c. In fact, we discovered that this result holds true for any $Q_{EC} \ll J_{final}$, where the final coupling strength is orders of magnitude larger than the energy fluctuations, a reasonable assumption for the Si microlattice samples because the energy fluctuations caused by electrochemistry are orders of magnitude lower than the stored elastic energy in the beams. In this regime, the final coupling strength becomes irrelevant to the formed domain sizes because domain boundaries stabilize at J such that $Q_{EC} < J \ll J_{final}$, and only the coupling ramp rate R with respect to the electrochemical energy fluctuation Q_{EC} governs the formed domain sizes (Fig. 4.18m). Fig. 4.19d illustrates that if we normalize the coupling ramp rate by the amplitude of energy fluctuations as $R^* = R/Q_{EC}$, the normalized ramp rate follows the same decay curve with correlation length ξ for all Q_{EC}. Therefore, even though it is difficult to have an accurate estimation of Q_{EC}, the qualitative results in our Monte Carlo simulations hold true for any $Q_{EC} \ll J_{final}$.

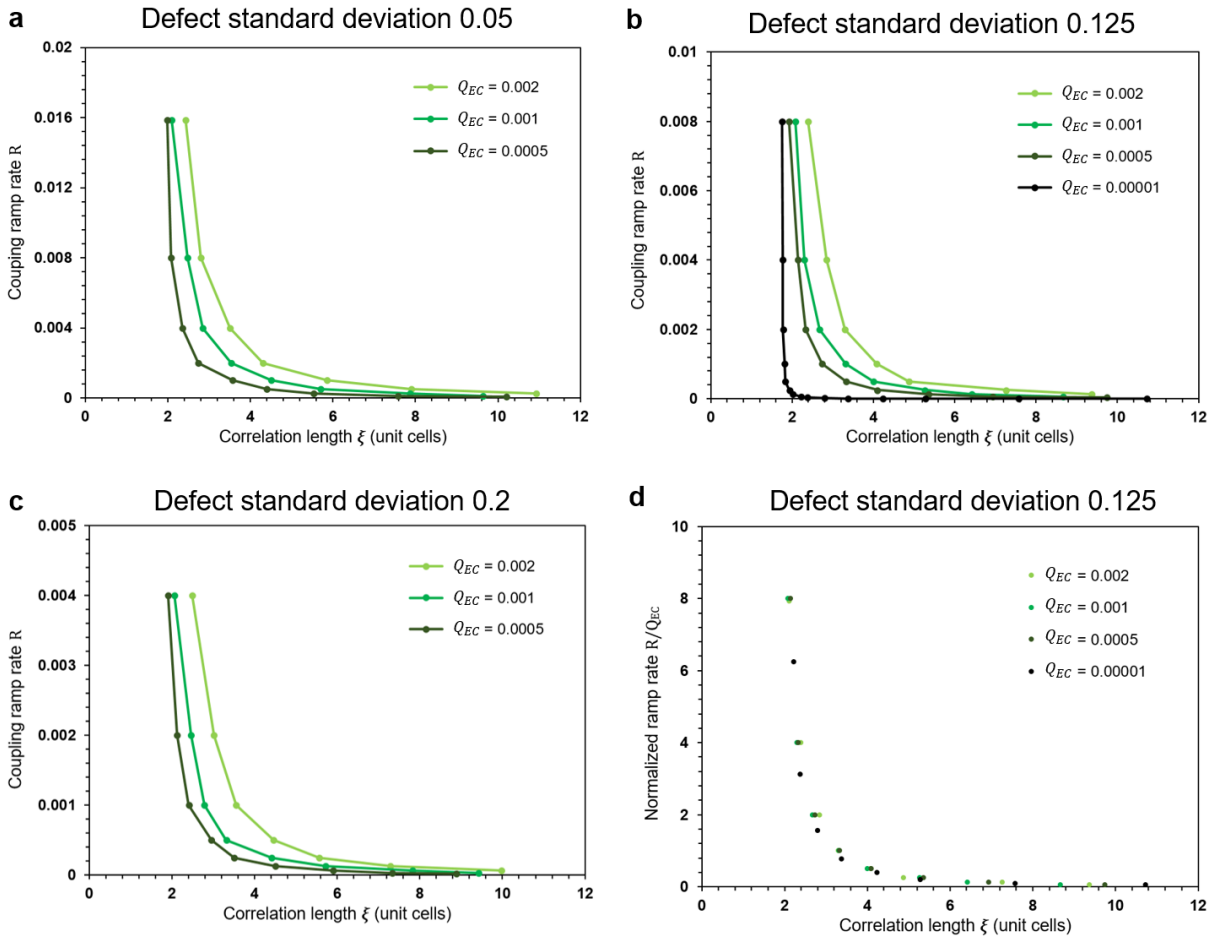

Figure 4.19 (a-c) Variations in correlation length ξ with coupling ramp rate R from Monte Carlo simulations with different energy fluctuations Q_{EC} (from 0.00001 to 0.002) and defect distributions h_i (from a standard deviation of 0.05 to 0.2). (d) Relation between correlation length ξ and normalized coupling ramp rate R/Q_{EC}.

4.14 Origin of Electrochemical Energy Fluctuations

In this section, we would like to discuss the physical origin of the energy fluctuation Q_{EC}. Fundamentally, these energy fluctuations arise from the chemical nature of lithiation. Processes like lithiating a Si thin film or electroplating Li metal onto a conductive substrate are inherently stochastic [171,172] and occur via a thermally-activated overcoming of an energy barrier, described by Arrhenius-type probabilities. It is also influenced and convoluted by the subsequent post-nucleation instabilities, like the resulting inhomogeneities in the local ion concentrations, electrical field, voltage, and stress state of lithiated Si. From the mechanical perspective of a

bistable beam that undergoes buckling upon loading, there is always a competing force balance on the two opposite sides of the beam before it irreversibly buckles in a particular direction. For lithiation-induced buckling of a Si beam, those stochastic local electrochemical nucleation events are occurring on the two opposite surfaces of the Si beam and constantly changing the local stress distribution. This stochastic perturbation of the competing force balance of the two sides of the Si beam during the initiation of the buckling deformation results in an effective energy fluctuation influencing the buckling direction of the beam. On a square-lattice system consisting of an 80 × 80 array of nodes, the energy fluctuation related to electrochemical reactions are coarse-grained onto each unit cell surrounding each node.

The collision theory of chemical reactions suggests that Li ions within the electrical double layer formed on any Si surface stochastically vibrate with a Maxwell-Boltzmann energy distribution. During lithiation, a small fraction of the Li ions colliding with the Si surface have enough energy to overcome the activation barrier for local nucleation of lithiation, which then triggers a series of instability events that lead to local stress changes in Si. Increasing the temperature shifts the energy distribution of Li ions and disproportionally increases the probability for effective collision with Si that leads to a local nucleation event, which provides insights into why Q_{EC} should not scale linearly with temperature. The rule-of-thumb in chemistry for many reactions happening at around room temperature is that the rate of reaction doubles for every 10°C rise in temperature. This agrees with our observations that increasing the temperature in experiments from room temperature to 37°C, which represents a negligible change in terms of absolute temperature, drives a significant change in the formed domain sizes (Fig. 4.18l). Larger temperature changes could also influence the reaction mechanisms especially for solid-electrolyte-interphase (SEI) formation [173] and side reactions, which could give rise to a completely different Q_{EC}. The mechanistic nature of the electrochemical energy fluctuation Q_{EC} should be pursued deeper and it is beyond the scope of this paper. Such temperature-like energy fluctuation has been adopted and measured for various statistical ensembles including granular materials [174–176], colloidal particles [170,177,178], and even population segregation [179]. For the purpose of the discussion here, our only assumption is that there exists an energy fluctuation Q_{EC} related to electrochemical reactions during lithiation-induced cooperative buckling. No matter how small Q_{EC} is compared with the final node rotation coupling J_{final}, as long as J is turned on gradually from zero as lithiation proceeds, Q_{EC} plays an

important and rate-dependent role of relaxing the system into a lower energy state during the initial stage of lithiation where J is still comparable to Q_{EC}.

4.15 Application and Outlook

Lithiation-induced cooperative beam buckling within Si microlattices demonstrates that architecture design and additive manufacturing in concert could pave a novel route for creating next-generation high performance batteries. Current state-of-the-art batteries employ electrodes that are comprised of a slurry mixture of active material particles, conductive additives, and polymer binders, which results in a convoluted internal structure and fundamental performance limitations [108]. Rationally designed 3D-architected electrodes could decouple the trade-off between transport kinetics and active material loading by providing fast electron and ion transport pathways via interconnected conductive scaffolds and low-tortuosity, periodic architectures [108,112]. Optimized porosity [87,109,113] have been shown to accommodate large volumetric expansions associated with beyond-intercalation high energy density electrode materials. In this work, we demonstrated buckling instabilities can be purposefully designed and engineered in architected electrodes as a novel stress relief mechanism. In the presented Si microlattice electrodes, the deformation mechanism includes simultaneous elastic buckling and plastic deformation, which can be tuned by the deformation phase map in Fig. 4.12f. The elastic buckling component is largely independent of the intrinsic post-elastic deformability of electrode materials and is not subject to plastic energy dissipation and strain rate sensitivity, which opens possibilities of utilizing this approach with brittle electrode materials such as sulfur. Optimizing architecture design could increase the energy density and potentially enable multi-functional capabilities for on-chip or implantable energy storage systems.

Furthermore, the demonstrated electrochemically driven cooperative buckling in Si microlattices uncovers a new regime for dynamic structural reconfiguration in architected materials. Most of the existing reconfigurable materials are soft polymer structures that rely on persistent external stimuli to stay in the deformed geometry [2,36,37,69,71,149,158] or are multi-stable in discrete configurations [34,148,180,181]. The Si microlattices in this work are electrochemically lithiated to induce simultaneous buckling and plastic deformation, which enables non-volatile reconfiguration in stiff architected materials. The degree of buckling can be continuously tuned

and even reversed by simple electrical control. Through the interactions among neighboring beams, cooperative buckling transforms a simple tetragonal lattice into a sinusoidal lattice with intriguing mechanical metamaterial properties, which is discussed here as an example of the capabilities of electrochemically reconfigurable architected materials. These buckled structures have been shown to have a negative Poisson's ratio upon lateral deformation [157–159], and deform synclastically upon out-of-plane bending [182]. In the dynamic realm, they provide an efficient platform for designing tunable phononic crystals. To illustrate this point, we constructed a finite element model to examine the change in phononic dispersion relations for in-plane elastic wave propagation in Si microlattices due to lithiation-induced cooperative buckling (see Appendix C). Fig. 4.20a-c and Fig. C.2 demonstrate that lithiation-induced cooperative buckling creates two 6 MHz-wide band gaps centered at 16 MHz and 44 MHz for waves propagating in all in-plane directions. Upon partial delithiation, the center frequencies of the bandgaps shift by 6 MHz and 9 MHz respectively. The formation and the set-and-hold tunability of these band gaps are attributed to both the structural transformations and the changes in material properties due to electrochemical reactions. We envision such tunable phononic band gaps of architected materials combined with the versatility of additive manufacturing could empower novel microelectromechanical systems (MEMS) [183]. Defect engineering, as demonstrated in this work, allows for accurate programing of distorted domain boundaries between ordered domains in which elastic wave propagation at certain frequencies is forbidden. This opens up opportunities to trap and control phonon modes inside the domain boundaries, which could potentially enable topological metamaterials [184,185]. Moreover, complex, tailor-made reconfigurability can be designed for non-periodic architectures by controlling the relative ratio of the polymer scaffold and the active material as well as mechanical constraints. Fig. 4.20d-k illustrate exemplar building blocks with rotational, bending, out-of-plane buckling, and expansive degrees of freedom induced by electrochemical lithiation. Even though the material systems used in this work are air-sensitive, other alloying systems and redox couples with compatible phase diagrams and realistic diffusion kinetics can be explored in aqueous electrolytes [186] or even body fluids [187,188]. For electrochemical discharge reactions like Si-Li alloying, the structural reconfiguration process releases energy in the form of electrical current, which can be used for simultaneous heating or communication. Therefore, bio-implantable applications and self-deployable devices are of particular interests because of the requirements of

large geometric transformations and the constant body environments that are insensitive or unreachable to external stimuli.

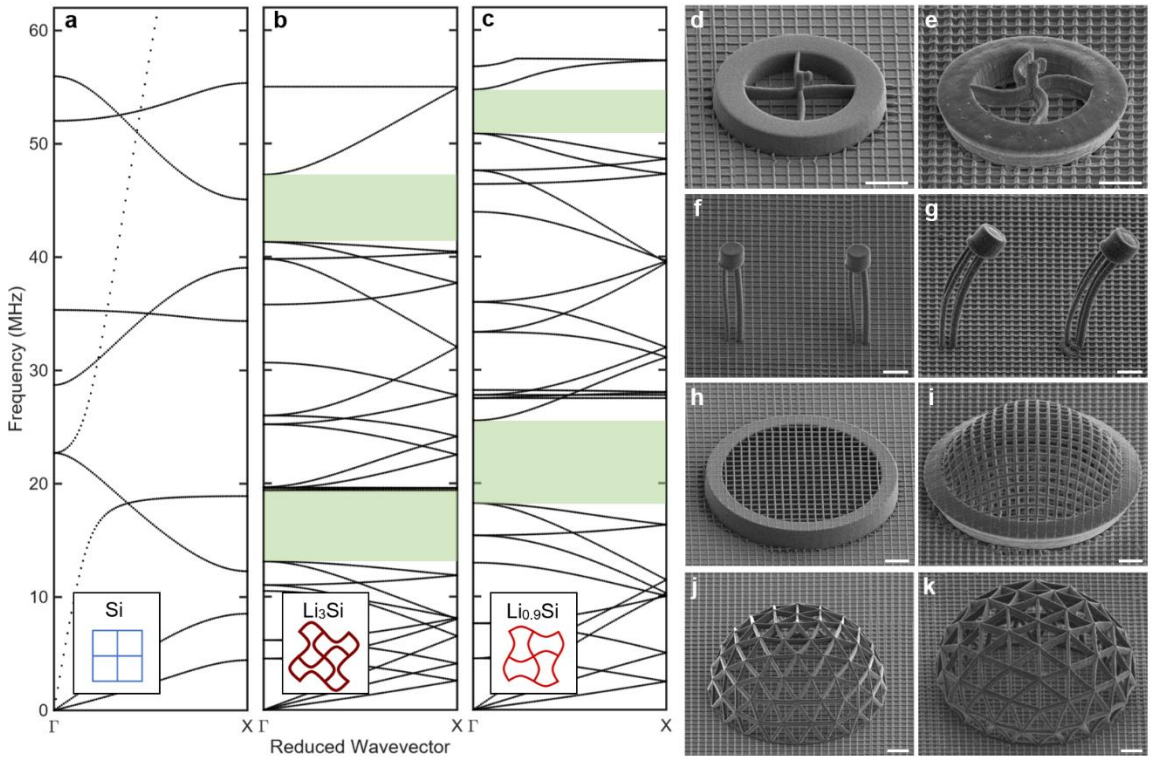

Figure 4.20 Outlook for electrochemically reconfigurable architected materials. (a-c) Simulated phononic dispersion relations of (a) as-fabricated Si microlattices, (b) lithiated Li3Si microlattices and (c) partially delithiated Li0.9Si microlattices using Bloch boundary conditions. Reduced wavevectors represent specific locations of the irreducible Brillouin zone in the reciprocal space. Point Γ to point X corresponds to waves propagating in the x or y direction (due to symmetry) of the microlattices. Extended dispersion relations provided in the Appendix C show that the band gaps, colored green in (b, c), exist in all in-plane directions. (d-k) Examples of electrochemically-driven microarchitectures whose reconfigurational degrees of freedom include (d, e) rotation, (f, g) bending, (h, i) out-of-plane buckling, and (j, k) structural expansion in response to lithiation. SEM images were taken at a tilt angle of 52°. Scale bars: 15 μm.

4.16 Comparison of Reconfiguration Mechanisms for Architected Materials

In this section, we compare the merits of electrochemically reconfigurable architected materials to those with other reconfiguration mechanisms in the literature. We do not intend to provide an exhaustive literature review but aim to put key features of various reconfigurable systems in perspective. Three major reconfiguration methods were previously reported: hydration-induced swelling, magnetic actuation, and various ways of mechanical deformation. In this work, we

proposed and demonstrated the use of electrochemical reactions to reconfigure architected materials. The key findings of the comparison are summarized in Table 4.1.

Reconfiguration mechanism	Continuous modulation	Control method	Remote control	Mechanical properties	Stability w/out stimuli	Response time	Feature size	Unit cell number	References
Swelling	No	Environment	No	Soft	No	5-15min	2.5μm-1mm	100	13, 14
Magnetic field	No	Magnetic field	Yes (w/ strong field)	Soft	No	0.1s	400μm	30	17
Mechanical deformation	Yes	Force or displacement	No	Soft	Discrete	10s	500μm-5cm	20	8, 9, 10-12
Electrochemical reactions	Yes	Voltage or current	Yes (in electrolyte)	Stiff	Yes	5min	1.3μm	6000 (laterally)	This work

Table 4.1 Comparison of reported reconfiguration mechanisms for architected materials.

Mechanical deformation and electrochemical reactions can modulate the degree of structural transformation continuously by applying a prescribed function of varying force/displacement and voltage/current; swelling and magnetic actuation are controlled by the surrounding environment in a more binary fashion toggling between “on” and “off” states. Electrochemically reconfigurable architected materials have the unique advantage of being electrically controlled and thus directly compatible with miniaturized electronic circuits. For example, they could be remotely programmed and deployed, as long as they operate in an ion-conducting electrolyte environment, which can be readily available in biological systems, for example in blood or urine [188]. A variety of aqueous redox chemistries (such as those of conjugated polymers) can be used for electrochemical reconfiguration in those environments. Another unique aspect of the electrochemical reconfiguration mechanism is that it operates even on stiff architected materials, such as Si, while other mechanisms generally work for soft polymers and hydrogels.

The most distinctive advantage of electrochemically reconfigurable architected materials is the stability and retention of their structural transformation upon the removal of external stimuli. Such non-volatility is also achieved in multi-stable mechanically deformed systems but only at pre-programmed, discrete increments, and the stored elastic energy is subject to external perturbation. One limitation of the electrochemical reconfiguration mechanism is the relatively slow response time, on the order of minutes, which can be shortened, if needed, by reducing the dimensions and the diffusion length of the chosen architecture. In terms of implementation, the electrochemically reconfigurable architected materials in this work have feature sizes on the order of 1 μm and contains a significantly larger number of repeating unit cells (see Table 4.1), which gives rise to

the intriguing stochastic domain formation process during structural transformation. Lastly, an alternative approach to achieve structural transformation in materials is through the use of actuators, such as piezoelectric transducers, operating at a high working frequency in the kHz-MHz range. These types of devices are limited by having to be modulated using a high voltage (kV), and the bias-induced deformation is generally a few percent strain as summarized by Acerce et al. [189]. The discussion here highlights the novelty of electrochemically reconfigurable architected materials presented in this work, that offer the possibility to dynamically control material architecture in a continuous, non-volatile and reversible fashion, which opens doors for numerous applications in the future.

4.17 Summary

In summary, we designed and fabricated a new class of reconfigurable architected materials based on electrochemically driven cooperative beam buckling. The large volumetric expansion and contraction of electrochemical alloying and dealloying reactions served as the driving force for stable, continuous, and reversible structural transformations through coupled mechanical instabilities. Accurate chemo-mechanical models revealed the dynamic interplay among different deformation mechanisms and provided design guidelines to control the instability of individual beams. We discovered and demonstrated that defects play a governing role in nucleation and growth of transformed domains during cooperative buckling, analogous to polycrystalline metal thin film growth. We utilized statistical mechanics tools to analyze the stochastic domain formation process and implanted artificial defects to precisely program the shape of domain boundaries. This framework of designing, fabricating, modeling, predicting and programing dynamic architected materials could inspire new pathways toward smart, multifunctional materials

Chapter 5

SUMMARY AND OUTLOOK

5.1 Summary

This thesis probes into the dynamic behaviors of architected materials undergoing electrochemical reactions and aims to provide an in-depth understanding of the underlying mechanisms as well as design principles generalizable for other functional architected material systems. We start by introducing a toolset of state-of-the-art techniques to fabricate rationally designed architected materials of intricate geometries and diverse chemical compositions. These additive manufacturing and post-processing methods are being improved incrementally and new fabrication routes being developed, but the most crucial key lies in the mindset of utilizing hierarchical architecture design to decouple critical trade-offs in complex systems with multi-faceted challenges. In batteries, the trade-off is between energy density and power density [108]; in conversion or alloying-based electrodes, the trade-off is Li storage capacity and mechanical stability [103]; in structural mechanics, the trade-off is between strength and density [9,10]; for thermal insulation, the trade-off is between thermal conductivity and stiffness [146]. The ability to design across multiple length scales with selected chemical compositions allows functional architected materials to break free from these constraints and occupy previously unreachable territories within the material property space. In this thesis, we illustrate such design principle through the example of 3D-architected Si electrodes. At the beam level, size-induced ductility and designed buckling instability work together to relieve lithiation-induced stresses enhancing the electrode material's mechanical robustness. At the lattice level, designated porosity could provide just enough space to accommodate the volume expansion of the active material without compromising the volumetric energy density. At the electrode level, the interconnected conductive scaffold and the low-tortuosity architecture facilitate efficient electron and ion transport throughout the electrode providing superior power performance even at a high active material loading. Even though such 3D-acrhitected electrodes are still at an early stage of development, they demonstrate the unprecedented control and rational design that architected materials could potentially enable in the future.

On a more fundamental level, the adaptive and reconfigurable architected materials examined in this thesis reveal the intriguing analogy between architected materials and classical materials. Current Li-ion batteries are based on the intercalation mechanism in which Li atoms can be reversibly inserted into and extracted from the interstitial sites of crystal lattices of the electrode materials, which requires a certain number of host atoms to accommodate each Li atom. For beyond-intercalation electrode materials like Si, the atomic ratio of the host material and Li is reversed with each Si atom alloying with up to four Li atoms, which inevitably causes significant volume expansion. 3D-architected electrodes essentially create "meta-lattices" that accommodate such volume expansion in the pore space within each unit cell in a similar way as the interstitial sites of crystal lattices. Meanwhile, purposely designed microlattices with coupled mechanical instabilities could also accommodate the volume expansion through cooperative buckling, which transforms the lattices' geometry to a different symmetry group. This phenomenon is analogous to how $LiMn_2O_4$, a cathode material with a cubic spinel crystal structure, undergoes a first-order phase transformation to a tetragonal spinel structure ($Li_2Mn_2O_4$) upon lithiation [190–192]. Furthermore, during lithiation-induced reconfiguration of these microlattices, local defects plays an important role in the formation of bistable buckling domains separated by distorted domain boundaries in a process similar to the island growth model of poly-crystal metal thin films. Such domain boundaries, consisted of Mode-II buckled beams with a higher elastic energy, introduce a degree of disorder to the cooperatively buckled lattices, just like grain boundaries do in crystalline materials. Finally, we demonstrate, through the comparison with the square-lattice antiferromagnetic Ising model, that the dynamic domain formation process during lithiation-induced cooperative buckling is subject to energy fluctuations intrinsic to the electrochemical environment, as manifested by the lithiation rate dependence of the domain size distribution. In the framework of statistical mechanics, a high lithiation rate is analogous to rapid quenching of a molten crystal system that results in smaller grains and a higher internal energy. Therefore, we believe these dynamic responses of architected materials undergoing electrochemical reactions uncover the underlying connections between architected materials and their classical counterparts, with profound implications on how we think about architected materials and how we could design them based on established materials science theories such as phase transformation and metallurgy.

5.2 Open Questions and Future Work

The field of architected materials is highly inter-disciplinary by nature and still at its infancy of development. More advanced fabrication techniques, further developed theory and modeling frameworks, and *in situ* and multi-physics characterization methods would all contribute immensely to understanding and designing architected materials with superior and more diverse properties. One important aspect that requires more attention and research efforts, I believe, is to demonstrate the functionalities as well as the limitations of architected materials in the practical context of potential applications. In this section, I discuss a few promising directions for suitable application of functional architected materials, which I hope to pursue in the future if the opportunity arises.

3D-Architected Solid-State Li Batteries

All-solid-state Li batteries, with a solid electrolyte instead of a liquid one, provide a very promising path for next generation energy storage systems. The most important advantage of solid-state batteries is that they enable high energy density electrode materials such as Li metal anodes and high-voltage metal oxide cathodes with a significantly reduced fire hazard. The intrinsic chemical stability of solid-state electrochemical reactions leads to the unprecedented cycling reversibility of 10000 cycles with 90% capacity retention [193] in prototypical solid-state Li batteries. The first rechargeable solid-state Li battery at room temperature was Li thin film batteries with sputtered LiPON (lithium phosphorus oxynitride) solid electrolytes [194] developed at the Oak Ridge National Lab in the 1990s. Despite continued research and development, it is still the best and arguably the only functional solid-state battery with a Li metal anode, reasonable Li utilization, and a stable cycle life [195]. Li thin film batteries demonstrate the vast potential of solid-state battery systems, but they also reveal three critical challenges. Frist, Li ion conductivity is generally 2-4 orders of magnitude lower in solid electrolytes than in liquid electrolytes. Li thin film batteries overcome the sluggish kinetics problem by decreasing the film thickness, which sacrifices the amount of energy that can be stored on a given area and requires layer-by-layer high vacuum vapor deposition that is inefficient and costly to scale up. Second, mechanical stability becomes a vital issue for an all-solid-state system, which is more susceptible to mechanical fracture and delamination with increased risk of internal shorting and loss of interfacial contact due to electrode volume expansion and contraction during cycling. Finally, the requirements for a solid electrolyte are so demanding that LiPON, which can only be produced in the thin film format, is still the best

overall performing material in terms of Li ion conductivity, chemical stability, and mechanical robustness due to its amorphous structure. Therefore, despite the unparalleled performance of Li thin film batteries, these challenges have limited them to niche applications such as bio-implantable devices.

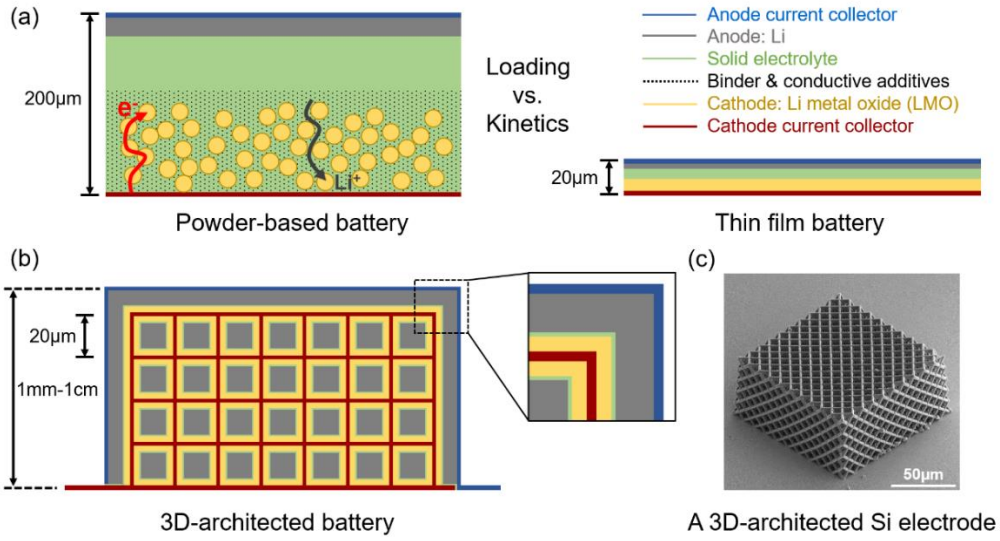

Figure 5.1 (a) Comparison between powder-based and thin film batteries. (b) Cross-sectional illustration of 3D-architected solid-state batteries with each color representing the same component as in (a). (c) Example of a 3D-architected Si electrode on a Cu scaffold.

To overcome the limitations of solid-state Li batteries, it is important to examine the two major types of electrode internal structures: powder-based electrodes and thin film electrodes. In a powder-based electrode which is widely used in Li-ion batteries, active material particles are embedded in an electrically and ionically conductive matrix through mixing with conductive carbon additives, polymer binder, and liquid or solid electrolyte (Fig. 5.1a left). In this configuration, Li solid diffusion in electrode materials—generally the rate-limiting factor in batteries—is limited to the particle size (1-10 μm). By controlling the Li solid diffusion length, powder-based electrodes can load more active materials on a given electrode area at the cost of a smaller volumetric packing density and slower transport kinetics due to the convoluted conductive pathways in the surrounding matrix with high tortuosity. Alternatively, if the electrodes are very thin, they can be made out of a monolithic, dense active material thin film (Fig. 5.1a right). In the so-called thin film batteries, transport kinetics is very good, but areal active material loading is severely limited by the film thickness. This fundamental tradeoff between areal active material

loading and transport kinetics in powder-based batteries and thin film batteries is illustrated in Fig. 5.1a. Because of solid electrolytes' low Li ion conductivity, the thin film configuration has a significant advantage for solid-state batteries. However, the detrimentally low areal active material loading makes Li thin film batteries impractical for most applications. Their volumetric energy density is further compromised because the battery packaging materials could easily be ten times thicker than the battery materials. Stacking individual thin film batteries layer-by-layer is possible, but the large number of layers required to reach a reasonable areal capacity makes it prohibitively difficult and extremely inefficient.

To preserve the exceptional performance of Li thin film batteries and resolve the areal mass loading problem, I propose a new design of 3D-architected solid-state Li battery to decouple the tradeoff between material loading and transport kinetics (Fig. 5.1b). Essentially, the 3D-architected solid-state battery "stacks" a thin film battery onto a 3D scaffold to increase the mass loading. The 3D-architected battery will start with an architected cathode, in which a layer of lithium metal oxide is coated on a conductive, interconnected scaffold with a periodic lattice structure. An example of such architected electrodes is shown in Fig. 5.1c. Next, a thin layer of solid electrolyte will be conformally coated on the architected cathode, and Li metal will fill the remaining pore space in the 3D lattice to function as the anode. Finally, electrical leads will be connected to the substrate for the cathode and to the top of the Li-filled lattice for the anode. In this way, we could build a fully interdigitated anode and cathode network where Li diffusion length is limited by the unit cell size and the areal active material loading is determined by the overall lattice height. Additive manufacturing provides independent control over the unit cell size and the lattice size, and thus decouples the critical tradeoff between material loading and transport kinetics. Rational architecture design also enables us to ensure matched capacities between the two electrodes and minimize the inactive scaffold volume. The self-supported lattice architecture can improve the mechanical stability during Li expansion and contraction. During discharge as Li is inserted into the cathode, pore space is created in the center of each unit cell without influencing the global lattice size; during charge, Li is electroplated back into the pore space. By modeling the optimal arrangement of 3D integration with 50% excess Li loading, I estimate the 3D-architected solid-state batteries could achieve a volumetric energy density of 1250 Wh/L, a gravimetric energy

density of 460 Wh/kg, and a power density of 1000 W/kg compared to that of 700 Wh/L, 250 Wh/kg, and 300 W/kg for state-of-the-art Li-ion batteries.

Other Directions of Interests

While electrochemically reconfigurable architected materials open up doors for a variety of applications, one readily relevant field is deployable biomedical implants such as coronary stents. Biological fluids such as blood and urine have been shown to function as the aqueous electrolyte for redox reactions of conjugated polymer actuators [188]. Integrated micro-devices with designed mechanical properties and structural transformations can be implanted through a minimally invasive procedure and deployed slowly or by programmed physical, chemical, or electronic triggers. Ultralow-power circuits with integrated sensors can be sustained by a small percentage of the stored electrochemical energy and be used to control the reconfiguration by reducing the electrical resistance and thus increasing the rate of the electrochemical reactions. Such biomedical implants based on additively manufactured architected materials can be customized to individual patients and deployed at places previously difficult to reach.

Another interesting application for architected electrochemical systems is electrochemically gated artificial neural networks for neuromorphic computing. Artificial intelligence and deep learning algorithms are extremely energy-inefficient to implement on computers with the conventional von Neumann architecture that runs computations in a mostly sequential fashion. Neuromorphic computing, first proposed by Caltech professor Carver Mead, aims to achieve highly efficient neural network computation through hardware-level emulation of the biological neural network of brain in which chemical fluxes are used to modulate the synaptic weight between connected neurons. Recently, a polymer-based electrochemical memristor device with hundreds of non-volatile conductance states within a ~1 V range and extremely low switching energy are developed [196] and implemented in a crossbar array for parallel programming [197]. 3D architectures of such electrochemical processing units with individually programmable synaptic weights could potentially open a path towards higher-order interconnectivity comparable to the human brain.

Lastly, a scalable, mask-based additive manufacturing method with a resolution less than 10μm and a printing size more than 10cm is crucial for building proof-of-concept devices of functional architected materials. Projector-based stereolithography technologies have tremendously expedited

industrial usage of 3D printed parts and materials. This method uses a projector's imaging unit to dynamically define 2D photomasks to polymerize a 3D object layer by layer. However, its printing area and resolution are limited by the tradeoff between the projection area and the pixel size. Meanwhile, for applications like batteries and vibrational or thermal control, simple periodic structures are sufficient, and potentially large production quantity favors template-based methods. Although the porous 3D micro-architecture forbids the use of physical molds, a photomask-based template could store the 3D geometric information for large-scale additive manufacturing. For example, to 3D print a cubic lattice in a way similar to projection stereolithography, only two types of cross-sectional photomasks are necessary. If the geometric information of the two cross-sections can be stored within one mask and alternates during photo-polymerization, large-scale, high-resolution 3D printing can be achieved. Possible solutions include transformable masks, multi-color masks, and optical meta-surface masks. Such mask-based 3D printing system could enable large-scale, high-resolution additive manufacturing at the cost of a reduced geometric freedom, which is a rational compromise for a variety of applications.

Appendix A. Coupled Chemo-Mechanical Finite Element Analysis of Si Microlattices

This section is adapted from [152] written by my collaborator Dr. Claudio V. Di Leo.

(i) FEA Modeling of a 3D buckling beam

We consider a single three-dimensional beam under pin-pin boundary conditions, the simulation domain of which is shown discretized in Fig. A.1a. Here, we discretize only a quarter of the full-geometry of a single beam. Mirror boundary conditions are applied about the center yz-plane at the face defined by finite element nodes ABEF and about the xy-plane at face defined by finite element nodes ABC. In order to apply pin-pin boundary conditions with zero moment about the x-axis we use a rigid analytical surface (not shown) which contacts the surface defined by finite element nodes EFG with a frictionless tangential behavior. The analytical surface is then constrained to have zero displacement and zero rotations about the y-axis and z-axis, thus allowing only for a pin-like behavior with free rotation about the x-axis. To prevent sliding with respect to the rigid analytical surface we constrain the nodes along the line defined by finite element nodes HG to have zero displacement in the y-direction. The finite elements discretizing the a-Si shell obey the material behavior described in the main portion of this work and in [131], while the polymer core is prescribed a linear elastic material behavior with Young's Modulus of $E = 5GPa$ and Poisson's ratio of $\nu = 0.38$.

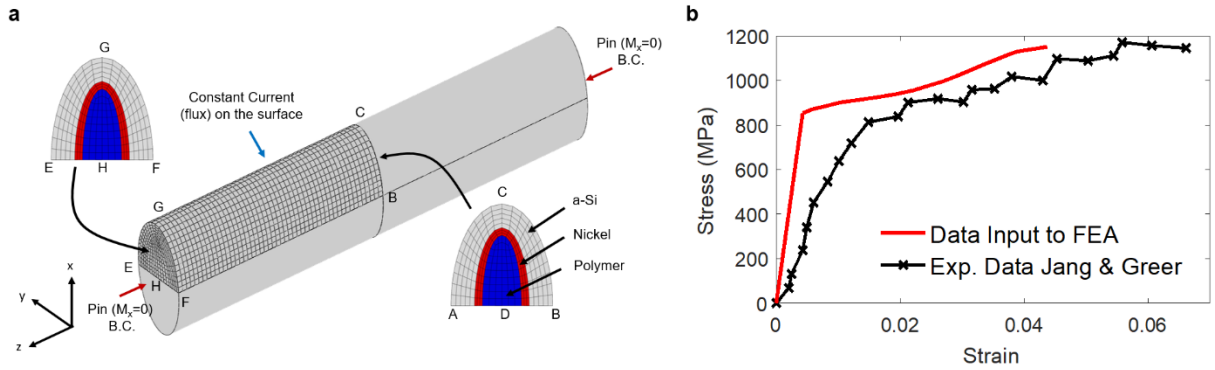

Figure A.1 (a) 3D mesh of a quarter of a Si-Ni-polymer beam with mirrored boundary conditions in the center and pinned boundary conditions at the end. (b) Stress-strain behavior of the Ni layer used in FEA compared with experimental results in [198].

The Ni layer in the three-dimensional beam simulations obeys the stress-strain behavior shown in Fig. A.1b. The elastic stiffness of $E = 200GPa$ is chosen from Luo et al. [199] while the plastic

yield stress and hardening behavior is extracted from the nano-pillar compression experiments of Jang et al. [198]. For plastic strains above those shown in the data below, the Nickel material is prescribed to behave perfectly plastic.

A constant flux (current), determined by a desired C-Rate, is prescribed on all the elements along the exterior surface of the beam. The flux is related to C-rate through the simple relation $j = -\left(V/A_{surf}\right)c_{max}(C_{rate}/3600)$, where V is the volume of a-Si, A the area over which the flux is applied, c_{max} the maximum molar concentration of Li in Si-Li alloys. The flux is ramped linearly from an initial value of zero to a final value t_{ramp} at which point it is held constant. In order to introduce an imperfection to the beam, we use different ramp times for the flux applied to the elements on the surface defined by FBCG and the elements on the surface defined by EACG. The flux on the surface FBCG reaches its stabilized value at $t_{ramp} = t_1$, while the flux on the surface EACG reaches its stabilized at $t_{ramp} = t_2$. The difference, $\Delta t_{ramp} = |t_2 - t_1|$, defines the degree of imperfection in the finite element simulation. It is important to note that we use the term "buckling" and "post-buckling" interchangeably. We do not here consider a perfect system and numerically compute the presence of an instability, rather we focus on the post-buckling behavior through simulation of a system with an imperfection. The simulated lithiation is stopped at a cutoff voltage of 0.03V. The simulation reproduces a voltage vs. state-of-charge (SOC) profile at C/6 comparable to experimental measurements as shown in Fig. 4.12b. Here we compare the simulation results with the experimental voltage profiles of the second cycle of 0.01 V-1.5 V cycling of a typical Si microlattice in a modified coin cell. We choose the second cycle in the experiment for comparison because the initial lithiation of pristine Si electrodes generally involves a different reaction mechanism due to surface passivation layers, solid-electrolyte interphase formation, and other parasitic reactions as indicated by the cyclic voltammogram in Fig. 4.9e. We choose the 1.5 V full delithiation cutoff voltage in the experiment for comparison because partial delithiation up to 0.6 V would retain 30 % of the inserted Li during the first lithiation inside the Si microlattice, which would be different from our simulation conditions.

In Fig. 4.12c-d, we chose to show the σ_{zz} component of stress since it captures both the development of tensile and compressive stresses at the mid-span of the beam. An alternative choice is to show the maximum principal stress σ_1. The maximum principal stress can more accurately

describe the formation of large (possibly tensile) stresses in the beam which can lead to fracture, however the direction of stress is not clear from contours of σ_1. Fig. A.2 shows simulation results of the first three half-cycles (first lithiation, first delithiation with a 0.6 V cutoff voltage, and second delithiation) using the maximum principal stress. At some instance in time the maximum principal stress can coincide with σ_{zz} but generally they are not the same. This is illustrated in Fig. A.2b below where we compare σ_{zz} and σ_1 for three points at the mid-span of the beam. Clearly we can see that at some instances in time, σ_{zz} is below σ_1 and the direction of maximum principal stress is not the same as that of the axial σ_{zz}, however at very large tensile stresses the σ_{zz} stress component agrees well with the maximum principal stress, demonstrating that this stress component is significant as a measure of maximum tensile stresses developing at the mid-span of the beam.

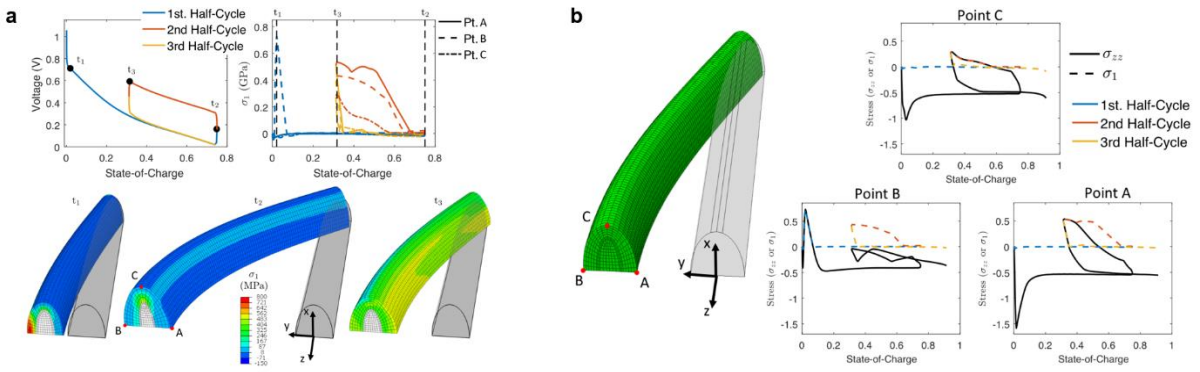

Figure A.2 (a) Simulation results for a 20 μm elastic-plastic beam with buckling for the first three half-cycles showing stress vs. SOC profiles and colored contours showing maximum principal stress $\boldsymbol{\sigma_1}$. (b) Comparison between stress vs. SOC profiles for $\boldsymbol{\sigma_{zz}}$ and $\boldsymbol{\sigma_1}$ at point A, B and C. We can observe that generally $\boldsymbol{\sigma_{zz}}$ captures the maximum tensile stresses developing at the cross-section for points A and C. At point B, $\boldsymbol{\sigma_{zz}}$ captures the compressive stress in that particular direction but there are also tensile stresses developing which are not in this direction and hence $\boldsymbol{\sigma_1}$ and $\boldsymbol{\sigma_{zz}}$ do not coincide.

(ii) Comparison with Experiment and Impact of the Polymer Core

The FEA model accurately captures the dynamic mechanical response of the Si-Ni-polymer beams with insightful spatio-temporal details as they are being lithiated. Fig. A.3a compared the deformed geometry of a simulated beam with a top-down SEM image of a lithiated Si microlattice, which shows excellent agreement.

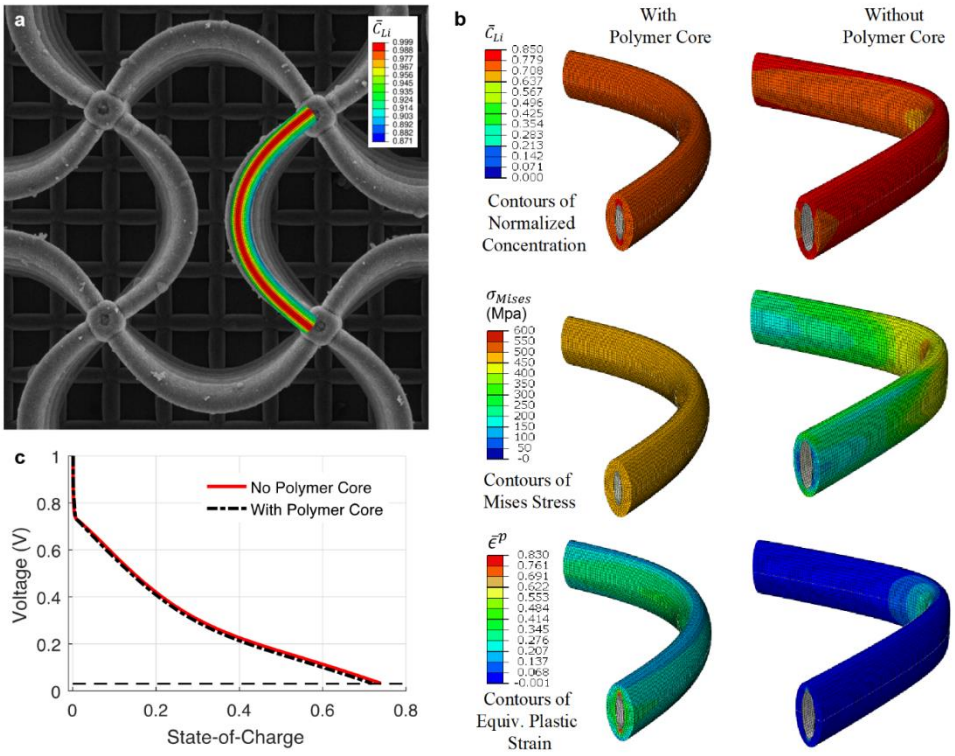

Figure A.3 (a) Comparison between the deformed geometry of a simulated Si-Ni-polymer beam after lithiation with a top-down SEM image of a lithiated Si microlattice, which shows excellent agreement. (b) Comparison of the simulation results of a Si-Ni-polymer beam with one without the polymer core showing that the absence of the polymer core would localize buckling deformation at the mid-span of the beam effectively forming a kink. (c) Simulated voltage vs. state-of-charge relations during lithiation at C/10 showing the polymer core has a negligible influence on the voltage response.

A relevant concern that is difficult to probe experimentally is whether decohesion of the Si/Ni layers from the polymer core significantly impacts the behavior of the system. In order to probe this we performed simulation at the extreme condition where the entire core is decohered and modeled this simply as an FEA simulation as described in section (i) above but without the polymer core. Fig. A.3b shows simulation results including the polymer core (left column) and without the polymer core (right column). The rows show contours of normalized concentration (top row), contours of Mises equivalent stress (middle row), and contours of equivalent plastic strain, (bottom row). As can be seen from the figure although all beams buckle and have stress and plastic strain contours of similar magnitudes, the shape of the buckled beam differs with the presence of the polymer core. Due in particular to its high volumetric stiffness, the polymer core prevents the buckling from localizing at the mid-span of the beam and effectively forming a kink, as is occurring in the simulations on the right column. In Fig. A.3a, we do not observe the kink-like

behavior shown in the simulation without the polymer core. Therefore, we believe the polymer core is adhered to the Si/Ni layers and contributing to the stiffness of the overall beam. While the overall distribution of equivalent stress and equivalent plastic strain varies slightly as shown in Fig. A.3b, the overall voltage vs. state-of-charge behavior as shown in Fig. A.3c remains largely unchanged as the stresses in the beams remain of similar magnitude.

(iii) FEA Modeling of Domain Interface Formation in 2D

We now turn our attention to the formation of different domains as has been experimentally observed. First, we study the manner in which incompatible defects in a lattice can cause the formation of domain boundaries where beams buckle in a Mode-II configuration. To study this problem, for computational efficiency, we make use of a two-dimensional plane-strain simulation as shown in Fig. A.4a. The simulation domain is composed of a cell of four nodes and connected by beams of length $L = 20\,\mu m$. The nodes along edges marked A are prescribed zero displacement in the x direction, while nodes on edges marked B are prescribed zero displacement in the y-direction. All edges A and B have zero flux while all other exterior edges are prescribed a constant flux equivalent to a C-Rate of C/10. Simulations are run until any node in the domain reaches the maximum normalized concentration of one. Normalized Li concentration is defined as the fraction of the maximum molar concentration c_{max} of Li in Li-Si alloys based on the theoretical capacity. Certain beams have imperfections in the form of an initial curvature with a mid-span displacement of $0.1\,\mu m$. As shown in Fig. A.4b, we perform two simulations. In the Mode-I set-up, the beams on the left-hand side are given initial imperfections which would cause the two nodes on the left to rotate in the compatible fashion shown, all other beams are straight. In the Mode-II configuration, the left hand side beams have the same imperfection while the right hand side beams are also given an initial imperfection which would cause the nodes on the right to rotate in an incompatible fashion with those of the left hand side.

The results of the two simulations are shown in Fig. 4.13a, b where contours of normalized concentration are shown over the deformed simulation domain (see Supplementary Video 12). In the Mode-I configuration (Fig. 4.13a), we get the expected result that the initial imperfections on the left hand side of the beam cause the entire domain to deform in a compatible fashion with all beams buckling in a Mode-I configuration. In essence, the imperfections on the left hand side

dictate the rotation of all nodes in the simulation domain. In the Mode-II configuration (Fig. 4.13b) the imperfections from the left hand side cannot overcome the initial imperfections of the right hand side and a domain boundary forms in the center beams where beams buckle in a Mode-II configuration. This simulation mimics the meeting of two domains with incompatible node rotations which subsequently causes the formation of a domain boundary with Mode-II buckled beams. In Fig. 4.13a, b, we overlay our simulations with the experimental images and observe good qualitative agreement in the numerically predicted and experimentally observed formation of domain boundaries. The finite-element simulations support the hypothesis that formation of domain boundaries in these microlattices is due to the meeting of two domains whose initial imperfections have caused them to buckle in two incompatible directions.

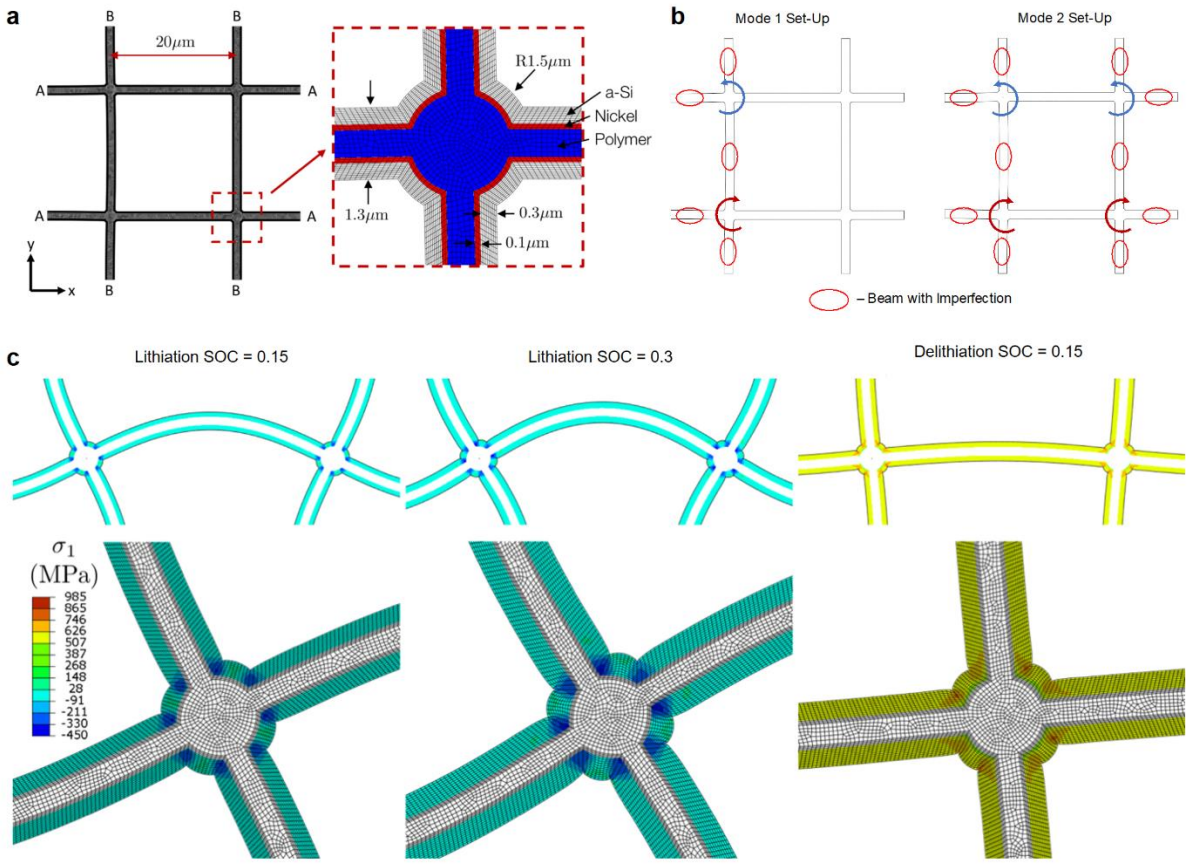

Figure A.4 (a) Simulation domain and finite-element mesh for 2D domain formation simulations. (b) Set-up of imperfections for Mode-I and Mode-II domain formation simulations. (c) Maximum principal stress in 2D Mode-1 Domain formation simulations. Contours are shown during lithiation at SOC = 0.15 and SOC = 0.3 and during delithiation at SOC = 0.15. Again we can clearly see the development of large tensile stresses during delithiation and a stress-concentration at the nodes.

In addition, Fig. A.4c shows the evolution of maximum principal stress σ_1 for the Mode-I domain simulations during lithiation at an SOC of 0.15 and 0.3 and during delithiation at an SOC of 0.15. Here too we capture the generation of large tensile stresses in the beam during delithiation. Importantly, we can also capture the presence of a stress concentration at the nodes as can be seen in all images. This agrees well with experimental results that have observed failure of the beams occurring at the nodes, where FEA simulations predict the largest maximum principal stresses occur.

Appendix B. Reduced-Order Chemo-Mechanical Model of Si Microlattices

This section is adapted from [152] written by my collaborators Arman Afshar and Dr. Claudio V. Di Leo. In the reduced-order model, we consider a pin-pin beam of length L which undergoes lithiation induced deformation. An imperfection is introduced by considering a pin which is offset by an amount e/L from the center of the beam. The beam is assumed to lithiate homogeneously with a uniform normalized concentration $\bar{c}$ of lithium in the material and under a uniaxial state of stress.

(i) Detailed development

The reduced-order model is based on a pin-pin beam with composite beam cross section as shown in Fig. B.1a below. A uniform in space and steady state in time concentration of Li is applied to the beam, resulting in volume expansion in the longitudinal and lateral directions. Because of the pinned ends at both sides a compressive axial force will develop in the beam which can eventually cause buckling. While bending of the beam is assumed to be governed by Euler-Bernoulli beam theory, a finite deformation modification is included to account for changes in the overall beam length, area and post buckled force.

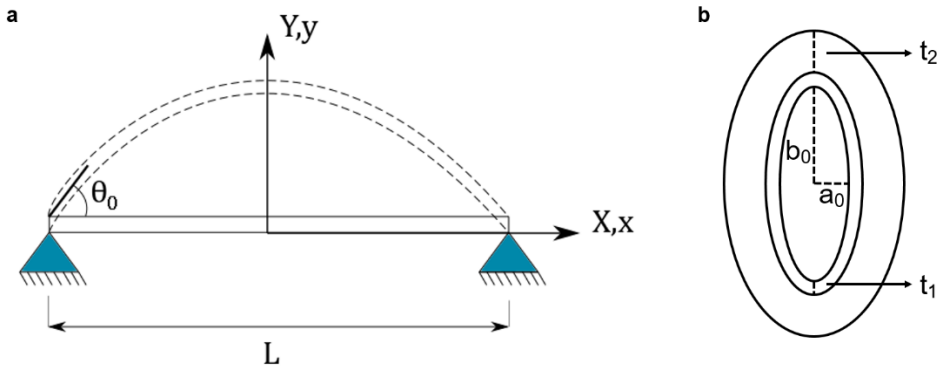

Figure B.1 (a) Schematic geometry of a pin-pin beam. (b) Composite cross-section with polymer core, Ni interlayer and outer a-Si shell.

The composite beam cross section is assumed to be made of three concentric ellipses, with an inner polymer core with dimensions of $a_0 = 0.25\,\mu m$ and $b_0 = 0.9\,\mu m$, an outer Ni shell with thickness $t_1 = 0.1\,\mu m$, and a-Si shell with thickness $t_2 = 0.3\,\mu m$, as shown in Fig. B.1b. For future use, these dimensions lead to an approximate radius of gyration of

$$r_g = \left(\frac{EI}{EA}\right)^{1/2} = \left(\frac{(EI)_{\text{Polymer}}+(EI)_{\text{Nickel}}+(EI)_{\text{Silicon}}}{(EA)_{\text{Polymer}}+(EA)_{\text{Nickel}}+(EA)_{\text{Silicon}}}\right)^{1/2} = 0.34\ \mu m, \quad (1)$$

where for the areas and material properties we used the reference values at zero lithiation. Each term in Eq. (1) is computed as follows:

$$(EI)_{\text{Polymer}} = 5 \times 10^3 \frac{\pi}{4} a_0^3 b_0 = 55 \text{ GPa } \mu\text{m}^4$$

$$(EI)_{\text{Nickel}} = 200 \times 10^3 \frac{\pi}{4}((a_0 + t_1)^3(b_0 + t_1) - a_0^3 b_0) = 4.5 \times 10^3 \text{ GPa } \mu\text{m}^4$$

$$(EI)_{\text{Silicon}} = 80 \times 10^3 \frac{\pi}{4}\left((a_0 + t_1 + t_2)^3(b_0 + t_1 + t_2) - (a_0 + t_1)^3(b_0 + t_1)\right) = 1.95 \times 10^4 \text{ GPa } \mu\text{m}^4$$

$$(EA)_{\text{Polymer}} = 5 \times 10^3 \pi a_0 b_0 = 3.53 \times 10^3 \text{ GPa } \mu\text{m}^2$$

$$(EA)_{\text{Nickel}} = 200 \times 10^3 \pi\left((a_0 + t_1)(b_0 + t_1) - a_0 b_0\right) = 7.9 \times 10^4 \text{ GPa } \mu\text{m}^2$$

$$(EA)_{\text{Silicon}} = 80 \times 10^3 \pi\left((a_0 + t_1 + t_2)(b_0 + t_1 + t_2) - (a_0 + t_1)(b_0 + t_1)\right) = 1.25 \times 10^5 \text{ GPa } \mu\text{m}^2$$

Using this radius of gyration, we can define a slenderness ratio in the following manner

$$\lambda = \frac{L}{R_g} = L\left(\frac{\overline{EA}}{\overline{EI}}\right)^{1/2}.$$

Here, R_g is the radius of gyration in which $\overline{EA}$ is the axial stiffness of the composite beam, and $\overline{EI}$ is the bending stiffness of the composite beam. For the computation of R_g we take both $\overline{EA}$ and $\overline{EI}$ as constants and compute them for the undeformed beam.

(ii) Post-buckling of beam under pin-roller boundary conditions with finite diffusion induced deformations

Following the derivation by Cedolin [200], classical Euler-Bernoulli beam theory is used in this work to analyze the instability problem. The moment M and curvature κ in each section of the beam related through

$$M = EI\kappa^2, \tag{2}$$

with EI is the composite Polymer-Nickel-Silicon section bending stiffness. Since small deformations are important, we consider the exact definition of curvature given by

$$\kappa = \frac{x'y'' - y'x''}{(x'+y')^{\frac{3}{2}}} \tag{3}$$

where x and y are the coordinates of the deformed beam, and the prime superscripts denote derivatives with respect to the parametric variable describing the curve. The initial undeformed coordinate of the beam is chosen as the parametric variable in this work. It should be noted that in Eq. (2) the Young's modulus is concentration dependent and changing during lithiation according to

$$E = aE_{\text{Li}} + (1-a)E_{\text{Si}}, \text{ and } \nu = a\,\nu_{Li} + (1-a)\nu_{Li} \tag{4}$$

where the fraction of lithium a is defined as

$$a = \frac{x_{\max}\,\bar{c}}{1 + x_{\max}\,\bar{c}} \tag{5}$$

with $x_{\max}$ the maximum stoichiometric amount of Lithium in the compound Li_xSi, and $\bar{c}$ denotes the normalized concentration of Lithium. In Eq. (2) the moment of inertia I will also evolve as the deformation changes. The elastic properties for the silicon shell are given by

$$E_{\text{Li}} = 5.0 \text{ GPa}, E_{\text{Si}} = 80.0 \text{ GPa}, \nu_{\text{Li}} = 0.36, \nu_{\text{Si}} = 0.22, x_{\max} = 3.75. \tag{6}$$

and for the Polymer-Nickel core

$$E_{\text{Ni}} = 200.0 \text{ GPa}, E_{\text{Polymer}} = 5.0 \text{ GPa}, \nu_{\text{Nickel}} = 0.30, \nu_{\text{Polymer}} = 0.38 \tag{7}$$

As in classical elastica solutions, in order to obtain the total force in the beam, one considers first moment equilibrium at an arbitrary point in the beam where using (2)

$$M = -Pw = EI\kappa = EI\frac{d\theta}{ds} \tag{8}$$

where w denotes the beam deflection. It should be noted that this is the total force in the beam, including the forces carried by the Silicon shell and the Polymer-Nickel core. Then taking a derivative and using the relation $dw/ds = \sin\theta$, we arrive at

$$-P\sin\theta = EI\frac{d^2\theta}{ds^2} \tag{9}$$

which can be solved analytically by multiplying both sides by $d\theta/ds$ and integrating which yields.

$$\frac{EI}{4P}\left(\frac{d\theta}{ds}\right)^2 = -\sin^2\frac{\theta}{2} + c^2\,. \tag{10}$$

Here c is related to initial slope Θ_0 (that is the slope of the beam at the pin-pin ends), the load P, and the imperfection (eccentricity) e through

$$c^2 = \frac{P}{EI}e^2 + \sin^2\frac{\theta_0}{2}\,. \tag{11}$$

Next, separation of variables leads to

$$\frac{d\theta}{\sqrt{c^2-\sin^2\frac{\theta}{2}}} = 2\sqrt{\frac{P}{EI}}\,ds. \tag{12}$$

This equation may be solved by employing a change of variable of the form

$$sin\frac{\theta}{2} = c\sin\phi, \quad \text{which yields} \quad d\theta = \frac{2c\cos\phi d\phi}{\sqrt{1-c^2\sin^2\phi}}. \tag{13}$$

Substituting (13) into (12), one can analytically find the solution with the use of elliptic integrals. Exploiting symmetry and integrating from one end of the beam $\phi = \pi/2$ to mid-length $= 0$, we arrive at the following equation for the reaction force

$$P = -\frac{4EI}{l^2}\int_0^{\pi/2}\frac{d\phi}{\sqrt{1-c^2\sin^2\phi}}. \tag{14}$$

Critically, (14) depends on the deformed length l of the beam which will be related to the amount of lithium in the system. For a given length l, (14) yields a family of solutions with a number of possible values of P and their corresponding deformed shapes.

For a given force P, we may compute the corresponding shape of the beam. For every point along the beam length, parameterized through the slope $-\theta_0 < \theta < \theta_0$, we define an angle α_j through

$$\alpha_j = \sin^{-1}\big(\sin(\theta_j/2)/c\big). \tag{15}$$

Then for point of the beam, the x and y coordinates can be calculated from

$$x_j = \sqrt{\frac{2EI}{P}} \int_{\alpha_j}^{\pi/2} \sqrt{1 - c^2 \sin^2 \phi}\, d\phi - \sqrt{\frac{EI}{P}} \int_{\alpha_j}^{\pi/2} \frac{d\phi}{\sqrt{1-c^2 \sin^2 \phi}}, \tag{16.1}$$

and

$$y_j = 2c \left(\sqrt{\frac{EI}{P}} \cos \alpha_j - \sqrt{\frac{EI}{P}} \cos \alpha_0 \right). \tag{16.2}$$

The stress state in the beam is assumed to be a combination of bending and compression, with all stresses zero except T_{11}, where T indicates the Cauchy stress in the silicon layer:

$$T_{11} = E_{\mathrm{Si}}\left(\frac{P}{EA} + \frac{M(b_0+t_1+t_2)}{EI}\right) \tag{17}$$

We now turn our attention to the deformed length l in (14) which must be prescribed before solving. Employing the decomposition of total stretch into elastic and swelling stretches yields

$$\lambda = l/l_0 \; = \lambda^e \lambda^s, \tag{18}$$

where l_0 is the original undeformed length of the beam. The elastic stretch is related to the axial load through the following constitutive equations:

For silicon:

$$P_{\mathrm{Si}} = EA_{\mathrm{Si}} log(\lambda^e). \tag{19.1}$$

And for the core:

$$P_{\mathrm{core}} = (EA_{\mathrm{Poly}} + EA_{\mathrm{Ni}}) log(\lambda). \tag{19.2}$$

with $A_{Si} = A_{Si,0}(\lambda^s)^2$ the current deformed area of the a-Si shell of the beam.

The swelling stretch λ^s is related to the concentration through

$$\lambda^s = (1 + \bar{\Omega}\bar{c})^{1/3} \tag{20}$$

where $\bar{\Omega} = \Omega c_{max} = 2.625$, with Ω the partial molar volume of Li in Si, and $c_{max} = 0.295 \times 10^6\ mol/m^3$ the maximum molar concentration of Li in Si. Using cross-sectional equilibrium and (19), we may rewrite (14) as a function of total stretch

$$\lambda^2\left(EA_{\mathrm{Si}} log\left(\lambda\lambda^{s^{-1}}\right) + (EA_{\mathrm{Poly}} + EA_{\mathrm{Ni}}) log(\lambda)\right) = -\frac{4EI}{l_0^2} \int_0^{\pi/2} \frac{d\phi}{\sqrt{1-c^2 \sin^2 \phi}} \tag{21}$$

For a given normalized concentration $\bar{c}$ (or equivalently swelling stretch), equation (21) may then be solved numerically using a non-linear solver to yield a family of solutions. Each solution has a unique total stretch, initial slope and hence a corresponding deformed shape. Fig. B.2a shows three such solutions for a particular concentration. It should be noted that in Eq. (21), the force in Nickel is assumed to be elastic until the stress reaches the Nano-crystalline Nickel yield stress, which is assumed to be $Y = 850$ MPa, after which a constant stress is used in the simulation.

We have now found a family of solutions for a pin-roller beam buckling under an applied load as shown in Fig. B.2. We now iterate over the deformed configurations (by iterating over the slope Θ_0 at the boundary conditions) until we find a solution which has zero displacement of the roller, this solution corresponds to the solution of a pin-pin beam undergoing lithiation induced buckling. For example, in Fig. B.2a, for the case of $l/l_0 = 1.3$, the middle solution is the correct solution. Fig. B.2b shows three solutions to the pin-pin lithiation induced buckling problem for various concentrations. We note that these drawings are actual solutions from our algorithm.

Having calculated the force and hence the stress, the energy of the beam can be calculated from the contributions of the axial deformation, the bending deformation, and the initial imperfection as follows

$$\Pi = \frac{1}{2}\int_0^l \left(\frac{AT_{11}^2}{E}\right)_{\text{Si}} dx + \frac{1}{2}\int_0^l \left(\frac{AT_{11}^2}{E}\right)_{\text{Core}} dx + \frac{1}{2}\int_0^l EI\kappa^2 dx - Pe\theta_0 \qquad (22)$$

We consider the critical buckling load to be equal to the state of deformation where the bending energy is 1% the total energy of the beam.

Finally, the stress in silicon can be calculated from Eq. (17), resulting in the maximum stress used in building the phase maps.

(iii) Summary

The process of solving the lithium-induced buckling problem is summarized as follows. For a given normalized concentration, the swelling stretch is known from Eq. (19) and Eq. (21) can be solved to yield a relationship between the unknown force λ and the unknown shape of the beam as characterized by the slope Θ_0 at the pin boundaries. We compute a series of solutions by iterating over the initial slope Θ_0 and computing the corresponding deformed shape. We then

search for the deformed shape which produces no displacement of the roller and identify this as the solution of the lithium-induced buckling of a pin-pin beam.

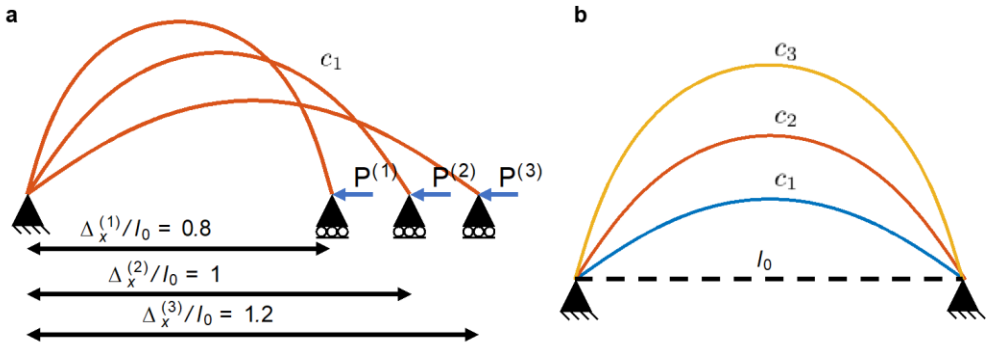

Figure B.2 Solutions from our post-buckling algorithm. (a) For a given concentration, we may solve for a family of solutions to the problem of a pin-roller beam under buckling due to an applied load P. We may then find which deformed shape is equivalent to a pin-pin condition in that there is no horizontal displacement of the pin. (b) Shows three solutions to the pin-pin problem for varying concentrations.

(iv) Plastic deformation of a straight beam and yield locus

In forming the phase-diagrams in Fig. 4.12f, we make use of a yield locus which corresponds to the force required to be applied to a straight beam to undergo plastic deformation. The yield stress is concentration dependent and given by

$$Y = Y_{\text{sat}} + (Y_0 - Y_{\text{sat}}) \exp(-\bar{c}/c^*), \tag{23}$$

Where Y_0 is the yield stress at zero concentration, Y_{sat} is the saturated yield stress, and c^* is a material property controlling how quickly the yield stress decays to its saturation value. We note that for the reduced-order model, unlike the full finite-element model, we neglect the rate-dependent portion of the plastic yield stress. The specific material properties are given by

$$Y_0 = 1.6 \text{ GPa}, Y_{\text{sat}} = 400\text{MPa}, \text{ and } c^* = 0.04. \tag{24}$$

(v) Electrochemistry

With the stress in the beam known we may compute a corresponding voltage for a given charging rate. The voltage is given by

$$V = V_0 + \mu/F + \eta \tag{25}$$

where V_0 is the reference potential, F the Faraday constant, μ the chemical potential of lithium at the surface of the electrode, and η the over-potential. The chemical potential is given by

$$\mu = \mu^0 + R\vartheta \ln\left(\gamma \frac{\bar{c}}{1-\bar{c}}\right) - \Omega \frac{\mathrm{T}_{11_{\mathrm{Si}}}}{3}, \tag{26}$$

which is simple to evaluate since we have assumed a uniform concentration across the beam. In (26), ϑ is the absolute temperature, and γ the activity coefficient (a function or $\bar{c}$). The over-potential for the lithium insertion is related to applied current through

$$\eta = 2\frac{R\vartheta}{F}\sinh^{-1}\left(\frac{-I}{2I_0}\right), \text{ with } I_0 = FK(1-\bar{c})^{1/2}(\bar{c})^{1/2}. \tag{27}$$

For a given C-Rate, the current is given by

$$I = F \frac{V_0}{A_{0,surface}} \frac{C_{\mathrm{rate}}}{3600}\, c_{R,\max} \tag{28}$$

where V_0 is the initial a-Si volume of the beam, and $A_{o,surface}$ is the initial surface area of the a-Si shell. These equations can be used to solve for the voltage vs. SOC (normalized concentration) of the beam during elastic-plastic or buckling deformations.

(vi) Results of the reduced-order model

Now we present the results of the reduced-order model, starting from force and stress curves. As can be seen in Fig. B.3, the shorter beam with $\lambda = 15$ has a significantly higher critical buckling force than the longer beam with $\lambda = 300$. Maximum bending stress during deformation of a beam is also shown in Fig. B.3. From these two force and stress vs SOC curves we can thus determine if a beam will deform through elastic buckling or by remaining straight and deforming elastic-plastically. For example, in Fig. B.3, the longest beam with $\lambda = 300$ would buckle and deform elastically without going to plastic deformation, while the shorter beam with $\lambda = 15$ would remain straight and deform elastic-plastically since the force required to yield any point on the beam plastically is below the critical buckling force. Finally, there is an in between deformation mode characterized by $\lambda = 30$ beam shown, where a beam is expected to first buckle and subsequently deform plastically when the maximum stress in the beam crosses the yield locus. Corresponding voltage plot for the same beam is also plotted in Fig. B.3c.

We note two important characteristics of the Force vs SOC curves shown in Fig. B.3. First, the decrease in reaction force after buckling is both due to non-linear geometric (large deformation)

effects as well as due to changes in material properties with concentration. Second, since the beams we are considering have an initial defect, there is no clear definition of a critical buckling load. We consider then as a buckling criterion the point in the deformation of the beam where the bending energy of the beam is 1% of the total elastic energy. This definition of buckling leads to points shown in black dots in Fig. B.3.

Using the force and stress vs. SOC results from the reduced-order model we may construct a phase-map of mechanical deformation regimes shown in Fig. 4.12f. The phase-map is a function of slenderness λ in the x-axis and SOC in the y-axis. The phase-map is divided into the four color coded regions. For small values of λ, as we increase SOC we have a transition from a straight beam which behaves elastically (green area) to a straight beam which behaves elastic-plastic (purple area). At larger values of λ, as we increase SOC we have a transition from a straight beam which behaves elastically (green area) to a buckled beam (blue area) and this transition is dependent on λ as it is governed by the critical buckling load which is length dependent. Continuing to increase SOC can lead the buckled beam (blue area) to transition to also yield plastically (red area). For very large values of λ, it is possible for a beam to buckle and not incur any plastic deformation.

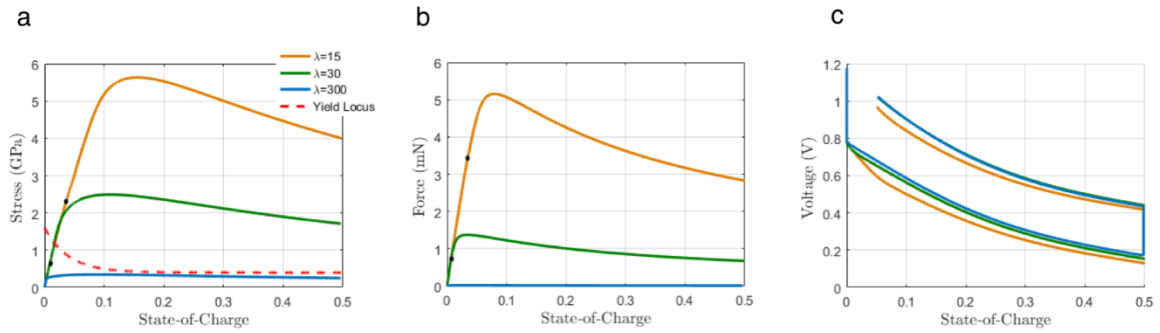

Figure B.3 Reduced-order model computations for beams with different slenderness ratios. (a) Stress vs. SOC including the yield locus. (b) Force vs. SOC predictions from reduced-order modeling. Here the beam imperfection is $e = 0.01 \times L$. (c) Voltage vs. SOC profiles.

Appendix C. Phononic Dispersion Relation Simulation of Si Microlattices

This section is adapted from [152] written by my collaborator Dr. Carlos M. Portela. To understand the effect of structural reconfiguration on the dynamic response of the electrochemically reconfigurable architected material, we conducted an eigenfrequency analysis on the three-dimensional unit cells at different stages of lithiation using the commercial finite element package COMSOL Multiphysics. We considered an extended unit cell consisting of 2 × 2 tetragonal unit cells for the buckled configurations to maintain compatibility and periodicity, while simulations for the initial as-fabricated configuration were done on a single unit cell (Fig. C.1). The geometry was represented using linear tetrahedral elements, with 18,600 to 110,000 elements per unit cell depending on geometry and the required discretization to ensure mesh-independent results. For simplicity, all material properties (i.e., Young's modulus, Poisson's ratio, and density) for a given beam were homogenized following a weighted volume average. This resulted in the elements corresponding to the horizontal beams (elliptical cross-section) and the vertical beams (circular cross-section) having different constituent material properties due to different volume ratios of Si, Ni, and polymer in each. This homogenization [201] is valid because the individual layer thicknesses of the polymer-Ni-Si beams are on the order of 100 nm, two orders of magnitude smaller than the size of the lattice unit cell. Therefore, the homogenized beam is indistinguishable from the multilayered beam for elastic waves in the MHz frequency range.

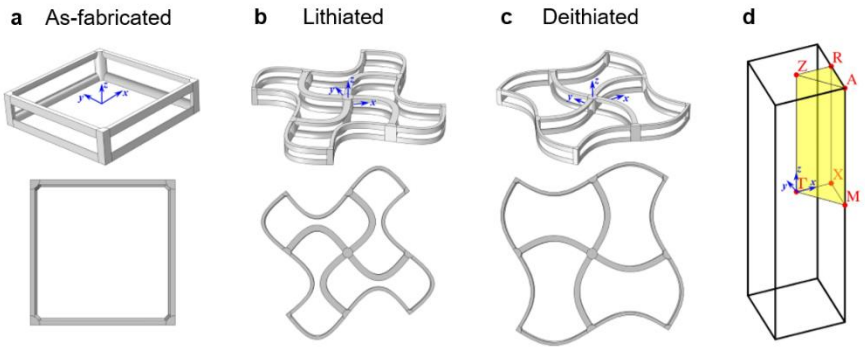

Figure C.1 (a) Initial, as-fabricated unit cell matching the dimensions of the fabricated samples. (b) Lithiated unit cell with buckled beams approximated by sinusoidal functions, resembling an 80% state-of-charge state corresponding to a Li_3Si phase. (c) Delithiated unit cell corresponding to a 70% Coulombic efficiency and 0.6V cutoff corresponding to $Li_{0.9}Si$. (d) First Brillouin zone (reciprocal space, black outline) and irreducible Brillouin zone (yellow). The real-space coordinate system is shown in blue.

For a comprehensive understanding of the dynamic response of this material, we considered three

different cases: (i) as-fabricated Si microlattices (Fig. C.1a), (ii) lithiated Si microlattices (Fig. C.1b), and (iii) delithiated Si microlattices (Fig. C.1c). For as-fabricated Si microlattices, we used the same geometry of the experimental samples described above. For lithiated Si microlattices, we considered a realistic 80% state-of-charge (SOC) that corresponds to the Li_3Si phase. For delithiated Si microlattices, we considered a realistic 70% Coulombic efficiency with a 0.6V delithiation voltage cutoff that leads to the $Li_{0.9}Si$ phase. We assumed 240% volumetric expansion for Li_3Si and 60% for $Li_{0.9}Si$ (compared to Si volume) based on simulation results in [156] and used those values to calculate the corresponding material densities. Poisson's ratios for $Li_{0.9}Si$ and Li_3Si were estimated by rule-of-mixtures of the atomic ratios of Si and Li. The Young's moduli of Si, $Li_{0.9}Si$, and Li_3Si were chosen to be 110GPa, 85GPa, and 50GPa, respectively, based on nanoindentation test results of amorphous Si thin films undergoing lithiation [202]. The calculated material properties for each material phase are summarized in Table C.1. The geometry of the buckled beams was approximated using sinusoidal functions for simplicity, although slightly smaller curvatures were observed at the center of some beams in the samples. The amplitudes of these functions were chosen based on experimental SEM images. To estimate the material volume ratios in each beam, the thickness of the $Li_{0.9}Si$ and Li_3Si layers were calculated from the sinusoidal geometry and the corresponding volumetric expansion ratios using SolidWorks.

	Polymer	**Ni**	**Si**	**$Li_{0.9}Si$**	**Li_3Si**	**Li**
E [GPa]	5	200	110	85	50	-
ν	0.38	0.31	0.22	0.31	0.33	0.36
ρ [kg/m^3]	1180	8080	2330	1784	1199	-

Table C.1 Material properties used in the phononic dispersion relation simulations.

Bloch boundary conditions were applied to the corresponding faces of the simulated unit cells. Using the corresponding irreducible Brillouin zone (IBZ) depicted in Fig. C.1d, we swept the wavevector through the edges and calculated the first 30 eigenfrequencies at each state to construct the dispersion relations. Fig. 4.20a-c demonstrate that lithiation-induced cooperative buckling creates two 6MHz-wide partial band gaps centered at 16MHz and 44MHz for waves propagating in the x or y direction of the microlattice, compared to no band gaps in the as-fabricated microlattice. Upon partial delithiation to a 0.6V cutoff, the center of the first band gap moves to 22MHz, and that of the second one to 53MHz, showing a correlation between the state-of-charge and the dynamic response. Fig. C.2a compares the dispersion relations between microlattices in

the buckled and partially unbuckled geometries without the changes in the chemical composition in the Si layer and the changes in the material properties of the beams due to lithiation. The mid-band frequencies for the first and the second band gaps change from 18MHz and 49MHz to 23MHz and 54MHz between the buckled and partially unbuckled states with purely geometric transformations. It indicates that the significant tunability of the phononic band gaps between the lithiated and delithiated states is a result of both structural transformations (whose effects are isolated in Fig. C.2a) and material property changes due to alloying/dealloying, with the latter enhancing the tunability of the band gaps (Fig. 4.20a-c). Sweeping the wavevector along the edges of the IBZ corresponding to all xy-plane direction (i.e., Γ-M-X-Γ) confirms the existence of the two partial band gaps in all in-plane directions for both the lithiated and delithiated configurations (Fig. C.2b-d).

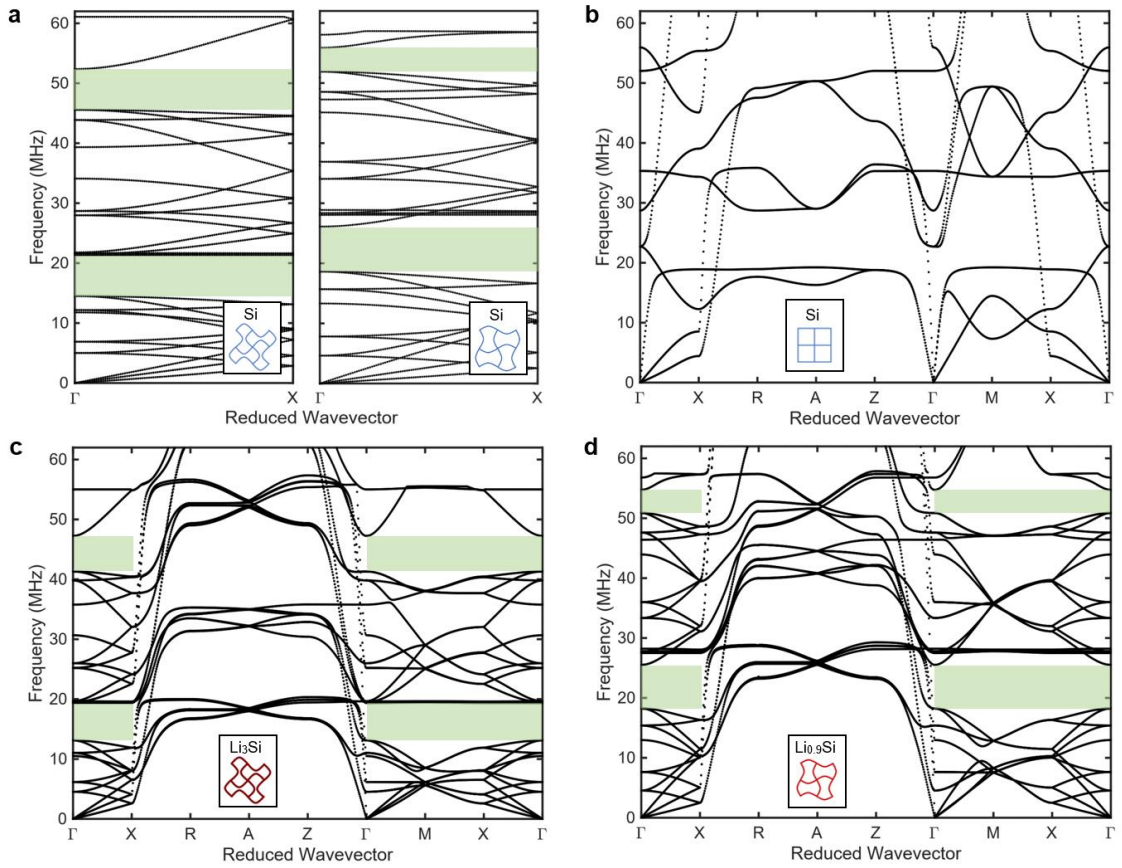

Figure C.2 (a) Comparison of dispersion relations (point Γ to point X) of buckled and partially unbuckled Si microlattices with the same curvature as the lithiated and delithiated microlattice, isolating the effects of geometric transformations from those of material property changes. (b-d) Extended dispersion relations of as-fabricated, lithiated and delithiated Si microlattices traversing through the Brillouin zone in 3D.

Appendix D. List of Supplementary Videos

Supplementary Video 1: *In situ* SEM lithiation of a Cu-Si Nanolattice

Supplementary Video 2: *In situ* SEM delithiation of a Cu-Si Nanolattice

Supplementary Video 3: FEA simulation results for Cu-Si Nanolattices

Supplementary Video 4: *In situ* lithiation of a Si microlattice at a constant current

Supplementary Video 5: *In situ* delithiation of a Si microlattice at a constant current

Supplementary Video 6: *In situ* lithiation of a Si microlattice with a resistor load

Supplementary Video 7: *In situ* cycling of a Si microlattice at high rates

Supplementary Video 8: *In situ* lithiation of a Si microlattice with programed artificial defects

Supplementary Video 9: FEA simulation of a 3D beam that buckles upon lithiation

Supplementary Video 10: FEA simulation to compare different deformation mechanisms

Supplementary Video 11: FEA simulation to compare beams with different slenderness ratios

Supplementary Video 12: FEA simulation of cooperative buckling of 2D extended unit cells

BIBLIOGRAPHY

1. Kroedel, S., Delpero, T., Bergamini, A., Ermanni, P. & Kochmann, D. M. 3D Auxetic Microlattices with Independently Controllable Acoustic Band Gaps and Quasi-Static Elastic Moduli. *Adv. Eng. Mater.* **16**, 357–363 (2014).

2. Babaee, S. *et al.* 3D soft metamaterials with negative poisson's ratio. *Adv. Mater.* **25**, 5044–5049 (2013).

3. Valentine, J. *et al.* Three-dimensional optical metamaterial with a negative refractive index. *Nature* **455**, 376–379 (2008).

4. He, H. *et al.* Topological negative refraction of surface acoustic waves in a Weyl phononic crystal. *Nature* **560**, 61–64 (2018).

5. Peng, S. *et al.* Three-Dimensional Single Gyroid Photonic Crystals with a Mid-Infrared Bandgap. *ACS Photonics* **3**, 1131–1137 (2016).

6. Tétreault, N. *et al.* New Route to Three-Dimensional Photonic Bandgap Materials: Silicon Double Inversion of Polymer Templates. *Adv. Mater.* **18**, 457–460 (2006).

7. Krödel, S. & Daraio, C. Microlattice Metamaterials for Tailoring Ultrasonic Transmission with Elastoacoustic Hybridization. *Phys. Rev. Appl.* **6**, 064005 (2016).

8. Matlack, K. H., Bauhofer, A., Krödel, S., Palermo, A. & Daraio, C. Composite 3D-printed meta-structures for low frequency and broadband vibration absorption. *Proc. Natl. Acad. Sci.* **113**, 8386–8390 (2015).

9. Bauer, J., Schroer, A., Schwaiger, R. & Kraft, O. Approaching theoretical strength in glassy carbon nanolattices. *Nat. Mater.* **15**, 438–443 (2016).

10. Meza, L. R., Das, S. & Greer, J. R. Strong, lightweight, and recoverable three-dimensional ceramic nanolattices. *Science* **345**, 1322–1326 (2014).

11. Wegst, U. G. K. *et al.* Bioinspired structural materials. *Nat. Mater.* **14**, 23–36 (2014).

12. Tanay, A. *et al.* Tough, Bio-Inspired Hybrid Materials. *Science* **322**, 1516–1520 (2008).

13. Song, J. *et al.* Processing bulk natural wood into a high-performance structural material. *Nature* **554**, 224–228 (2018).

14. Meza, L. R. *et al.* Resilient 3D hierarchical architected metamaterials. *Proc. Natl. Acad. Sci. U. S. A.* **112**, 11502–7 (2015).

15. Frenzel, T., Kadic, M. & Wegener, M. Three-dimensional mechanical metamaterials with a twist. *Science* **358**, 1072–1074 (2017).

16. Lin, X. *et al.* All-optical machine learning using diffractive deep neural networks. *Science* **361**, 1004–1008 (2018).

17. Montemayor, L. C., Meza, L. R. & Greer, J. R. Design and Fabrication of Hollow Rigid Nanolattices via Two-Photon Lithography. *Adv. Eng. Mater.* **16**, 184–189 (2014).

18. Wendy Gu, X. & Greer, J. R. Ultra-strong architected Cu meso-lattices. *Extrem. Mech. Lett.* **2**, 7–14 (2015).

19. Montemayor, L. C. & Greer, J. R. Mechanical Response of Hollow Metallic Nanolattices: Combining Structural and Material Size Effects. *J. Appl. Mech.* **82**, 1–10 (2015).

20. Jang, D., Meza, L. R., Greer, F. & Greer, J. R. Fabrication and deformation of three-dimensional hollow ceramic nanostructures. *Nat Mater* **12**, 893–898 (2013).

21. Schaedler, T. A. *et al.* Ultralight metallic microlattices. *Science* **334**, 962–5 (2011).

22. Papageorgiou, D. G., Kinloch, I. A. & Young, R. J. Mechanical properties of graphene and graphene-based nanocomposites. *Prog. Mater. Sci.* **90**, 75–127 (2017).

23. Wu, B., Heidelberg, A. & Boland, J. J. Mechanical properties of ultrahigh-strength gold nanowires. *Nat. Mater.* **4**, 525–529 (2005).

24. Greer, J. R. & Nix, W. D. Nanoscale gold pillars strengthened through dislocation starvation. *Phys. Rev. B - Condens. Matter Mater. Phys.* **73**, 1–6 (2006).

25. Zhang, X., Vyatskikh, A., Gao, H., Greer, J. R. & Li, X. Lightweight, flaw-tolerant, and ultrastrong nanoarchitected carbon. *Proc. Natl. Acad. Sci.* **116**, 6665–6672 (2019).

26. Thompson, R. L., Wang, Y. Q. & Greer, J. R. Irradiation enhances strength and deformability of nano-architected metallic glass. *Adv. Eng. Mater.* **20**, 1–11 (2018).

27. Shaw, L. A. *et al.* Computationally efficient design of directionally compliant metamaterials. *Nat. Commun.* **10**, 291 (2019).

28. Portela, C. M., Greer, J. R. & Kochmann, D. M. Impact of node geometry on the effective stiffness of non-slender three-dimensional truss lattice architectures. *Extrem. Mech. Lett.* **22**, 110–138 (2018).

29. Wang, Q. *et al.* Lightweight Mechanical Metamaterials with Tunable Negative Thermal Expansion. *Phys. Rev. Lett.* **117**, 1–6 (2016).

30. Qu, J., Kadic, M., Naber, A. & Wegener, M. Micro-Structured Two-Component 3D Metamaterials with Negative Thermal-Expansion Coefficient from Positive Constituents. *Sci. Rep.* **7**, 1–8 (2017).

31. Kadic, M., Bückmann, T., Stenger, N., Thiel, M. & Wegener, M. On the practicability of pentamode mechanical metamaterials. *Appl. Phys. Lett.* **100**, 191901 (2012).

32. Lipton, J. I. *et al.* Handedness in shearing auxetics creates rigid and compliant structures. *Science* **360**, 632–635 (2018).

33. Shaw, L. A., Chizari, S., Dotson, M. & Hopkins, J. B. Compliant rolling-contact architected materials for shape reconfigurability. *Nat. Commun.* **9**, 4594 (2018).

34. Haghpanah, B., Salari-sharif, L., Pourrajab, P., Hopkins, J. & Valdevit, L. Multistable Shape-Reconfigurable Architected Materials. *Adv. Mater.* **28**, 7915–7920 (2016).

35. Frenzel, T., Findeisen, C., Kadic, M., Gumbsch, P. & Wegener, M. Tailored Buckling Microlattices as Reusable Light-Weight Shock Absorbers. *Adv. Mater.* **28**, 5865–5870

(2016).

36. Overvelde, J. T. B., Weaver, J. C., Hoberman, C. & Bertoldi, K. Rational design of reconfigurable prismatic architected materials. *Nature* **541**, 347–352 (2017).

37. Coulais, C., Teomy, E., De Reus, K., Shokef, Y. & Van Hecke, M. Combinatorial design of textured mechanical metamaterials. *Nature* **535**, 529–532 (2016).

38. Kang, S. H. *et al.* Complex ordered patterns in mechanical instability induced geometrically frustrated triangular cellular structures. *Phys. Rev. Lett.* **112**, 098701 (2014).

39. Reid, D. R. *et al.* Auxetic metamaterials from disordered networks. *Proc. Natl. Acad. Sci.* **115**, E1384–E1390 (2018).

40. Rocks, J. W. *et al.* Designing allostery-inspired response in mechanical networks. *Proc. Natl. Acad. Sci.* **114**, 2520–2525 (2016).

41. Yablonovitch, E. Photonic band-gap crystals. *J. Phys. Condens. Matter* **5**, 2443–2460 (1993).

42. Olsson, R. H. & El-Kady, I. Microfabricated phononic crystal devices and applications. *Meas. Sci. Technol.* **20**, (2009).

43. Schittny, R., Kadic, M., Guenneau, S. & Wegener, M. Experiments on Transformation Thermodynamics : Molding the Flow of Heat. **195901**, 1–5 (2013).

44. Ergin, T., Stenger, N., Brenner, P., Pendry, J. B. & Wegener, M. Three-Dimensional Invisibility Cloak at Optical Wavelengths. (2010).

45. Zhang, S., Xia, C. & Fang, N. Broadband acoustic cloak for ultrasound waves. *Phys. Rev. Lett.* **106**, 024301 (2011).

46. Thiel, M., Rill, M. S., von Freymann, G. & Wegener, M. Three-Dimensional Bi-Chiral Photonic Crystals. *Adv. Mater.* **21**, 4680–4682 (2009).

47. Li, F., Huang, X., Lu, J., Ma, J. & Liu, Z. Weyl points and Fermi arcs in a chiral phononic crystal. *Nat. Phys.* **14**, 30 (2018).

48. Yu, Y. *et al.* Nonreciprocal transmission in a nonlinear photonic-crystal Fano structure with broken symmetry. *Laser Photon. Rev.* **9**, 241 (2015).

49. He, C. *et al.* Acoustic topological insulator and robust one-way sound transport. *Nat. Phys.* **12**, 1124–1129 (2016).

50. Lu, L., Joannopoulos, J. D. & Soljačić, M. Topological states in photonic systems. *Nat. Phys.* **12**, 626–629 (2016).

51. Huber, S. D. Topological mechanics. *Nature* **12**, 621 (2016).

52. Qi, X. L. & Zhang, S. C. Topological insulators and superconductors. *Rev. Mod. Phys.* **83**, (2011).

53. Bertoldi, K., Vitelli, V., Christensen, J. & van Hecke, M. Flexible mechanical metamaterials. *Nat. Rev. Mater.* **2**, 17066 (2017).

54. Chen, B. G., Upadhyaya, N. & Vitelli, V. Nonlinear conduction via solitons in a topological mechanical insulator. *Proc. Natl. Acad. Sci.* **111**, 13004 (2014).

55. Liu, B. *et al.* Topological kinematics of origami metamaterials. *Nat. Phys.* **14**, 811 (2018).

56. Paulose, J., Meeussen, A. S. & Vitelli, V. Selective buckling via states of self-stress in topological metamaterials. *Proc. Natl. Acad. Sci.* **112**, 7639–7644 (2015).

57. Coulais, C., Sounas, D. & Alù, A. Static non-reciprocity in mechanical metamaterials. *Nature* **542**, 461–464 (2017).

58. Khanikaev, A. B. *et al.* Photonic topological insulators. *Nat. Mater.* **12**, 233–239 (2012).

59. Lu, L. *et al.* Experimental observation of Weyl points. **349**, 622–625 (2015).

60. Serra-garcia, M. *et al.* Observation of a phononic quadrupole topological insulator. *Nature* **555**, 342–345 (2018).

61. Brown, T. L., LeMay, H. E., Bursten, B. E., Murphy, C. J. & Woodward, P. M. *Chemistry: the Central Science*. (Pearson).

62. Pham, M., Liu, C., Todd, I. & Lertthanasarn, J. Damage-tolerant architected materials inspired by crystal microstructure. *Nature* **565**, 305 (2019).

63. Truby, R. L. & Lewis, J. A. Printing soft matter in three dimensions. *Nature* **540**, 371–378 (2016).

64. Ruzin, S. & Aaron, H. Http://microscopy.berkeley.edu/courses/tlm/2P/index.html.

65. Fischer, J., Thiel, M. & Wegener, M. Matter made to order. *IEEE Spectr.* **51**, 34–58 (2014).

66. Yuk, H. & Zhao, X. A New 3D Printing Strategy by Harnessing Deformation, Instability, and Fracture of Viscoelastic Inks. *Adv. Mater.* **1704028**, 1704028 (2017).

67. Noor, N. *et al.* 3D Printing of Personalized Thick and Perfusable Cardiac Patches and Hearts. *Adv. Sci.* **6**, 1900344 (2019).

68. Ahn, B. Y. *et al.* Omnidirectional Printing and of Flexible , Stretchable , Silver Microelectrodes Spanning. *Science* **323**, 1590–1593 (2009).

69. Kim, Y., Yuk, H., Zhao, R., Chester, S. A. & Zhao, X. Printing ferromagnetic domains for untethered fast-transforming soft materials. *Nature* **558**, 274 (2018).

70. Cui, H. *et al.* Three-dimensional printing of piezoelectric materials with designed anisotropy and directional response. *Nat. Mater.* **18**, 234–241 (2019).

71. Sydney Gladman, A., Matsumoto, E. A., Nuzzo, R. G., Mahadevan, L. & Lewis, J. A. Biomimetic 4D printing. *Nat. Mater.* **15**, 413 (2016).

72. Zheng, X. *et al.* Multiscale metallic metamaterials. *Nat. Mater.* **15**, 1100 (2016).

73. Tumbleston, J. R. *et al.* Continuous liquid interface production of 3D objects. *Science* **347**, 1394 (2015).

74. Koffler, J. *et al.* Biomimetic 3D-printed scaffolds for spinal cord injury repair. *Nat. Med.* **25**, 263–269 (2019).

75. Grigoryan, B. *et al.* Multivascular networks and functional intravascular topologies within biocompatible hydrogels. *Science* **364**, 458 (2019).

76. Mateos, A. J., Huang, W., Zhang, Y. & Greer, J. R. Discrete-Continuum Duality of Architected Materials : Failure , Flaws , and Fracture. *Adv. Funct. Mater.* 1806772 (2018). doi:10.1002/adfm.201806772

77. Pearse, A. J. *et al.* Nanoscale Solid State Batteries Enabled by Thermal Atomic Layer Deposition of a Lithium Polyphosphazene Solid State Electrolyte. *Chem. Mater.* **29**, 3740 (2017).

78. Pearse, A. *et al.* Three-Dimensional Solid-State Lithium-Ion Batteries Fabricated by Conformal Vapor-Phase Chemistry. *ACS Nano* **12**, 4286–4294 (2018).

79. Kozen, A. C., Pearse, A. J., Lin, C.-F., Noked, M. & Rubloff, G. W. Atomic Layer Deposition of the Solid Electrolyte LiPON. *Chem. Mater.* **27**, 5324–5331 (2015).

80. Xu, C., Gallant, B. M., Wunderlich, P. U., Lohmann, T. & Greer, J. R. Three-Dimensional Au Microlattices as Positive Electrodes for Li–O2 Batteries. *ACS Nano* **9**, 5876–5883 (2015).

81. Lee, J. K., Kim, G. P., Song, I. K. & Baeck, S. H. Electrodeposition of mesoporous V2O5with enhanced lithium-ion intercalation property. *Electrochem. commun.* **11**, 1571–1574 (2009).

82. Armstrong, E., O'Sullivan, M., O'Connell, J., Holmes, J. D. & O'Dwyer, C. 3D Vanadium Oxide Inverse Opal Growth by Electrodeposition. *J. Electrochem. Soc.* **162**, D605–D612 (2015).

83. Engstrom, A. M. & Doyle, F. M. Exploring the cycle behavior of electrodeposited vanadium oxide electrochemical capacitor electrodes in various aqueous environments. *J. Power Sources* **228**, 120–131 (2013).

84. El-Enany, G., Lacey, M. J., Johns, P. A. & Owen, J. R. In situ growth of polymer electrolytes on lithium ion electrode surfaces. *Electrochem. commun.* **11**, 2320–2323 (2009).

85. Rhodes, C. P., Long, J. W. & Rolison, D. R. Direct electrodeposition of nanoscale solid polymer electrolytes via electropolymerization of sulfonated phenols. *Electrochem. Solid State Lett.* **8**, A579–A584 (2005).

86. Plylahan, N. *et al.* Highly conformal electrodeposition of copolymer electrolytes into titania nanotubes for 3D li-ion batteries. *Nanoscale Res. Lett.* **7**, 1–11 (2012).

87. Xia, X., Di Leo, C. V., Gu, X. W. & Greer, J. R. In situ lithiation-delithiation of mechanically robust Cu-Si core-shell nanolattices in a scanning electron microscope. *ACS Energy Lett.* **1**, 492–499 (2016).

88. McOwen, D. W. *et al.* 3D-Printing Electrolytes for Solid-State Batteries. *Adv. Mater.* **30**,

1–7 (2018).

89. Walker, S. B. & Lewis, J. A. Reactive silver inks for patterning high-conductivity features at mild temperatures. *J. Am. Chem. Soc.* **134**, 1419–1421 (2012).

90. Vyatskikh, A. *et al.* Additive manufacturing of 3D nano-architected metals. *Nat. Commun.* **9**, 593 (2018).

91. Eckel, Z. C. *et al.* Additive manufacturing of polymer-derived ceramics. *Science* **351**, 58–62 (2016).

92. Huggins, R. A. & Nix, W. D. Decrepitation model for capacity loss during cycling of alloys in rechargeable electrochemical systems. *Ionics (Kiel).* **6**, 57–63 (2000).

93. Chew, H., Hou, B., Wang, X. & Xia, S. Cracking mechanisms in lithiated silicon thin film electrodes. *Int. J. Solids Struct.* **51**, 4176–4187 (2014).

94. Li, J., Dozier, A. K., Li, Y., Yang, F. & Cheng, Y.-T. Crack Pattern Formation in Thin Film Lithium-Ion Battery Electrodes. *J. Electrochem. Soc.* **158**, A689 (2011).

95. Ryu, I., Choi, J. W., Cui, Y. & Nix, W. D. Size-dependent fracture of Si nanowire battery anodes. *J. Mech. Phys. Solids* **59**, 1717–1730 (2011).

96. Liu, X. H. *et al.* Size-Dependent Fracture of Silicon Nanoparticles During Lithiation. *ACS Nano* **6**, 1522–1531 (2012).

97. Obrovac, M. N. & Chevrier, V. L. Alloy negative electrodes for Li-ion batteries. *Chem. Rev.* **114**, 11444–11502 (2014).

98. Whittingham, M. S. History, Evolution, and Future Status of Energy Storage. *Proc. IEEE* **100**, 1518–1534 (2012).

99. *USABC Goals for Advanced Batteries for EVs — CY 2020 Commercialization*. (2017).

100. Chan, C. K. *et al.* High-performance lithium battery anodes using silicon nanowires. *Nat. Nanotechnol.* **3**, 31–5 (2008).

101. Seh, Z. W., Sun, Y., Zhang, Q. & Cui, Y. Designing high-energy lithium–sulfur batteries. *Chem. Soc. Rev.* **45**, 5605–5634 (2016).

102. Tikekar, M. D., Choudhury, S., Tu, Z. & Archer, L. A. Design principles for electrolytes and interfaces for stable lithium-metal batteries. *Nat. Energy* **1**, (2016).

103. McDowell, M. T., Lee, S. W., Nix, W. D. & Cui, Y. 25th anniversary article: Understanding the lithiation of silicon and other alloying anodes for lithium-ion batteries. *Adv. Mater.* **25**, 4966–4985 (2013).

104. Liu, N. *et al.* A pomegranate-inspired nanoscale design for large-volume-change lithium battery anodes. *Nat. Nanotechnol.* **9**, 187–192 (2014).

105. Zhang, H. & Braun, P. V. Three-dimensional metal scaffold supported bicontinuous silicon battery anodes. *Nano Lett.* **12**, 2778–83 (2012).

106. Liu, X. H. *et al.* Anisotropic swelling and fracture of silicon nanowires during lithiation.

Nano Lett. **11**, 3312–3318 (2011).

107. McDowell, M. T. *et al.* In situ TEM of two-phase lithiation of amorphous silicon nanospheres. *Nano Lett.* **13**, 758–64 (2013).

108. Braun, P. V. & Cook, J. B. Deterministic design of chemistry and mesostructure in Li-ion battery electrodes. *ACS Nano* **12**, 3060–3064 (2018).

109. Liu, J. *et al.* Mechanically and chemically robust sandwich-structured C @ Si @ C nanotube array Li-ion battery anodes. *ACS Nano* **9**, 1985–1994 (2015).

110. Pikul, J. H., Gang Zhang, H., Cho, J., Braun, P. V & King, W. P. High-power lithium ion microbatteries from interdigitated three-dimensional bicontinuous nanoporous electrodes. *Nat. Commun.* **4**, 1732 (2013).

111. Zhang, H., Shi, T., Wetzel, D. J., Nuzzo, R. G. & Braun, P. V. 3D Scaffolded Nickel-Tin Li-Ion Anodes with Enhanced Cyclability. *Adv. Mater.* **28**, 742–747 (2016).

112. Zhang, H., Yu, X. & Braun, P. V. Three-dimensional bicontinuous ultrafast-charge and -discharge bulk battery electrodes. *Nat. Nanotechnol.* **6**, 277–81 (2011).

113. Zhang, H. & Braun, P. V. Three-dimensional metal scaffold supported bicontinuous silicon battery anodes. *Nano Lett.* **12**, 2778–83 (2012).

114. Ning, H. *et al.* Holographic patterning of high-performance on-chip 3D lithium-ion microbatteries. *Proc. Natl. Acad. Sci.* **112**, 6573 (2015).

115. Wang, X. *et al.* High damage tolerance of electrochemically lithiated silicon. *Nat. Commun.* **6**, 8417 (2015).

116. Zhao, K. *et al.* Concurrent Reaction and Plasticity during Initial Lithiation of Crystalline Silicon in Lithium-Ion Batteries. *J. Electrochem. Soc.* **159**, A238–A243 (2012).

117. Ryu, I., Lee, S. W., Gao, H., Cui, Y. & Nix, W. D. Microscopic model for fracture of crystalline Si nanopillars during lithiation. *J. Power Sources* **255**, 274–282 (2014).

118. Berla, L. A. *et al.* Robustness of amorphous silicon during the initial lithiation / delithiation cycle. *J. Power Sources* 253–259 (2014). doi:10.1016/j.jpowsour.2014.02.032

119. Lee, S. W. *et al.* Kinetics and fracture resistance of lithiated silicon nanostructure pairs controlled by their mechanical interaction. *Nat. Commun.* **6**, 7533 (2015).

120. Yoon, T., Nguyen, C. C., Seo, D. M. & Lucht, B. L. Capacity Fading Mechanisms of Silicon Nanoparticle Negative Electrodes for Lithium Ion Batteries. *J. Electrochem. Soc.* **162**, A2325–A2330 (2015).

121. Cui, L.-F., Hu, L., Wu, H., Choi, J. W. & Cui, Y. Inorganic Glue Enabling High Performance of Silicon Particles as Lithium Ion Battery Anode. *J. Electrochem. Soc.* **158**, A592 (2011).

122. Wang, C. *et al.* Self-healing chemistry enables the stable operation of silicon microparticle anodes for high-energy lithium-ion batteries. *Nat. Chem.* **5**, 1042–8 (2013).

123. Boles, S. T., Sedlmayr, A., Kraft, O. & Mönig, R. In situ cycling and mechanical testing

of silicon nanowire anodes for lithium-ion battery applications. *Appl. Phys. Lett.* **100**, 243901 (2012).

124. Lee, B. S. *et al.* Fabrication of Si core/C shell nanofibers and their electrochemical performances as a lithium-ion battery anode. *J. Power Sources* **206**, 267–273 (2012).

125. Tsuda, T. *et al.* In situ SEM observation of the Si negative electrode reaction in an ionic-liquid-based lithium-ion secondary battery. *Microscopy* **64**, 159–168 (2015).

126. Hovington, P. *et al.* In situ Scanning electron microscope study and microstructural evolution of nano silicon anode for high energy Li-ion batteries. *J. Power Sources* **248**, 457–464 (2014).

127. Bridel, J.-S., Azaïs, T., Morcrette, M., Tarascon, J.-M. & Larcher, D. In Situ Observation and Long-Term Reactivity of Si/C/CMC Composites Electrodes for Li-Ion Batteries. *J. Electrochem. Soc.* **158**, A750 (2011).

128. Baranchugov, V., Markevich, E., Pollak, E., Salitra, G. & Aurbach, D. Amorphous silicon thin films as a high capacity anodes for Li-ion batteries in ionic liquid electrolytes. *Electrochem. commun.* **9**, 796–800 (2007).

129. Bucci, G., Nadimpalli, S. P. V, Sethuraman, V. A., Bower, A. F. & Guduru, P. R. Measurement and modeling of the mechanical and electrochemical response of amorphous Si thin film electrodes during cyclic lithiation. *J. Mech. Phys. Solids* **62**, 276–294 (2014).

130. Yang, H., Citrin, M., Xia, X., Nieh, S. & Greer, J. R. Microstructure evolution in “Li-free” thin film solid-state batteries. *Prep.* (2019).

131. Di Leo, C. V., Rejovitzky, E. & Anand, L. Diffusion–deformation theory for amorphous silicon anodes: The role of plastic deformation on electrochemical performance. *Int. J. Solids Struct.* **67**–**68**, 283–296 (2015).

132. Pharr, M., Suo, Z. & Vlassak, J. J. Variation of stress with charging rate due to strain-rate sensitivity of silicon electrodes of Li-ion batteries. *J. Power Sources* **270**, 569–575 (2014).

133. Xiao, X., Liu, P., Verbrugge, M. W., Haftbaradaran, H. & Gao, H. Improved cycling stability of silicon thin film electrodes through patterning for high energy density lithium batteries. *J. Power Sources* **196**, 1409–1416 (2011).

134. Pharr, M., Suo, Z. & Vlassak, J. J. Measurements of the fracture energy of lithiated silicon electrodes of Li-ion batteries. *Nano Lett.* **13**, 5570–5577 (2013).

135. Beuth, J. L. Cracking of thin bonded films in residual tension. *Int. J. Solids Struct.* **29**, 1657–1675 (1992).

136. Suo, Z. & Hutchinson, J. W. Sandwich Test Specimen for Measuring Interface Crack Toughness. *Mater. Sci. Eng.* **A107**, 135–143 (1989).

137. Hutchinson, J. W. & Suo, Z. Mixed Mode Cracking in Layered Materials. *Advances in Applied Mechanics* **29**, 63–191 (1991).

138. Maranchi, J. P., Hepp, A. F., Evans, A. G., Nuhfer, N. T. & Kumta, P. N. Interfacial Properties of the a-Si/Cu: Active–Inactive Thin-Film Anode System for Lithium-Ion

Batteries. *J. Electrochem. Soc.* **153**, A1246 (2006).

139. Irwin, G. R. Analysis of Stresses Strains Near End of a Crack Traversing a Plate. *J. Appl. Mech.* **24**, 361–364 (1957).

140. Griffith, A. A. The Phenomenon of Rupture and Flow in Solids. *Philos. Trans. Roy. Soc. London* **A221**, 163–198 (1920).

141. Graetz, J., Ahn, C. C., Yazami, R. & Fultz, B. Highly Reversible Lithium Storage in Nanostructured Silicon. *Electrochem. Solid-State Lett.* **6**, A194 (2003).

142. Perng, Y.-C. *et al.* Synthesis of ion conducting LixAlySizO thin films by atomic layer deposition. *J. Mater. Chem. A* **2**, 9566 (2014).

143. Sassin, M. B., Long, J. W., Wallace, J. M. & Rolison, D. R. Routes to 3D conformal solid-state dielectric polymers: electrodeposition versus initiated chemical vapor deposition. *Mater. Horiz.* **2**, 502–508 (2015).

144. Bryzek, J. *et al.* Marvelous MEMs: Advanced IC sensors and microstructures for high volume applications. *IEEE Circuits Devices Mag.* **22**, 8–28 (2006).

145. Hodgins, D. *et al.* Healthy aims: Developing new medical implants and diagnostic equipment. *IEEE Pervasive Comput.* **7**, 14–20 (2008).

146. Dou, N. G., Jagt, R. A., Portela, C. M., Greer, J. R. & Minnich, A. J. Ultralow thermal conductivity and mechanical resilience of architected nanolattices. *Nano Lett.* **18**, 4755–4761 (2018).

147. Fu, H. *et al.* Morphable 3D mesostructures and microelectronic devices by multistable buckling mechanics. *Nat. Mater.* **17**, 268–276 (2018).

148. Shan, S. *et al.* Multistable Architected Materials for Trapping Elastic Strain Energy. *Adv. Mater.* **27**, 4296–4301 (2015).

149. Kang, S. H. *et al.* Buckling-induced reversible symmetry breaking and amplification of chirality using supported cellular structures. *Adv. Mater.* **25**, 3380–3385 (2013).

150. Liu, J. *et al.* Harnessing Buckling to Design Architected Materials that Exhibit Effective Negative Swelling. *Adv. Mater.* **28**, 6619–6624 (2016).

151. Coulais, C., Kettenis, C. & van Hecke, M. A characteristic lengthscale causes anomalous size effects and boundary programmability in mechanical metamaterials. *Nat. Phys.* **14**, 40 (2018).

152. Xia, X. *et al.* Electrochemically reconfigurable architected materials. *Under Rev.* (2019).

153. Liu, X. H. *et al.* Self-limiting lithiation in silicon nanowires. *ACS Nano* **7**, 1495–1503 (2013).

154. Baggetto, L., Danilov, D. & Notten, P. H. L. Honeycomb-structured silicon: Remarkable morphological changes induced by electrochemical (De)lithiation. *Adv. Mater.* **23**, 1563–1566 (2011).

155. Bhandakkar, T. K. & Johnson, H. T. Diffusion induced stresses in buckling battery

electrodes. *J. Mech. Phys. Solids* **60**, 1103–1121 (2012).

156. Huang, S. & Zhu, T. Atomistic mechanisms of lithium insertion in amorphous silicon. *J. Power Sources* **196**, 3664–3668 (2011).

157. Körner, C. & Liebold-Ribeiro, Y. A systematic approach to identify cellular auxetic materials. *Smart Mater. Struct.* **24**, 025013 (2015).

158. Chen, Y., Li, T., Scarpa, F. & Wang, L. Lattice Metamaterials with Mechanically Tunable Poisson's Ratio for Vibration Control. *Phys. Rev. Appl.* **7**, 024012 (2017).

159. Clausen, A., Wang, F., Jensen, J. S., Sigmund, O. & Lewis, J. A. Topology Optimized Architectures with Programmable Poisson's Ratio over Large Deformations. *Adv. Mater.* **27**, 5523–5527 (2015).

160. Chan, C. K. *et al.* High-performance lithium battery anodes using silicon nanowires. *Nat. Nanotechnol.* **3**, 31–5 (2008).

161. Gao, H. *et al.* Parasitic Reactions in Nanosized Silicon Anodes for Lithium-Ion Batteries. *Nano Lett.* **17**, 1512–1519 (2017).

162. Feng, K. *et al.* Silicon-Based Anodes for Lithium-Ion Batteries: From Fundamentals to Practical Applications. *Small* **1702737**, 1702737 (2018).

163. Ogata, K. *et al.* Evolving affinity between Coulombic reversibility and hysteretic phase transformations in nano-structured silicon-based lithium-ion batteries. *Nat. Commun.* **9**, 479 (2018).

164. Wu, H. *et al.* Stable cycling of double-walled silicon nanotube battery anodes through solid-electrolyte interphase control. *Nat. Nanotechnol.* **7**, 310–315 (2012).

165. Nix, W. D. & Clemens, B. M. Crystallite coalescence: A mechanism for intrinsic tensile stresses in thin films. *J. Mater. Res.* **14**, 3467 (1999).

166. Nowak, U. & Usadel, K. D. Structure of domains in random Ising magnets. *Phys. Rev. B* **46**, 8329 (1992).

167. Landau, D. P. & Binder, K. *A Guide to Monte Carlo Simulations in Statistical Physics*. (Cambridge University Press, 2015).

168. Sahni, P. S., Grest, G. S., Anderson, M. P. & Safran, S. A. Kinetics of ordering in two dimensions. II. Quenched systems. *Phys. Rev. B* **28**, 2705 (1983).

169. Cornell, S. & Stinchcombe, R. Freezing in a two-dimensional Glauber system under continuous cooling. *Phys. Rev. B* **45**, 2725 (1992).

170. Shokef, Y., Souslov, A. & Lubensky, T. C. Order by disorder in the antiferromagnetic Ising model on an elastic triangular lattice. *Proc. Natl. Acad. Sci.* **108**, 11804 (2011).

171. Mayers, M. Z., Kaminski, J. W. & Miller, T. F. Suppression of dendrite formation via pulse charging in rechargeable lithium metal batteries. *J. Phys. Chem. C* **116**, 26214–26221 (2012).

172. Aryanfar, A. *et al.* Dynamics of lithium dendrite growth and inhibition: Pulse charging

experiments and monte carlo calculations. *J. Phys. Chem. Lett.* **5**, 1721–1726 (2014).

173. Haruta, M. *et al.* Temperature effects on SEI formation and cyclability of Si nanoflake powder anode in the presence of SEI-forming additives. *Electrochim. Acta* **224**, 186–193 (2017).

174. Zheng, J., Sun, A., Wang, Y. & Zhang, J. Energy Fluctuations in Slowly Sheared Granular Materials. *Phys. Rev. Lett.* **121**, 248001 (2018).

175. Song, C., Wang, P. & Makse, H. A. Experimental measurement of an effective temperature for jammed granular materials. *Proc. Natl. Acad. Sci.* **102**, 2299–2304 (2005).

176. Patrick, M., Gianfranco, D., Alain, B. & Vittorio, L. Observing Brownian motion and measuring temperatures in vibration-fluidized granular matter. *Nature* **424**, 909–912 (2003).

177. Ojha, R. P., Lemieux, P., Dixon, P. K., Liu, A. J. & Durian, D. J. Statistical mechanics of a gas-fluidized particle. *Nature* **427**, 521–523 (2004).

178. Segre, P. N., Liu, F., Umbanhowar, P. & Weitz, D. A. An effective gravitational temperature for sedimentation. *Nature* **409**, 594–597 (2001).

179. Stauffer, D. & Solomon, S. Ising, Schelling and self-organising segregation. *Eur. Phys. J. B* **57**, 473 (2007).

180. Restrepo, D., Mankame, N. D. & Zavattieri, P. D. Phase transforming cellular materials. *Extrem. Mech. Lett.* **4**, 52–60 (2015).

181. Correa, D. M. *et al.* Negative stiffness honeycombs for recoverable shock isolation. *Rapid Prototyp. J. 21/2* **21**, 193–200 (2015).

182. Liebold-Ribeiro, Y. & Körner, C. Phononic band gaps in periodic cellular materials. *Adv. Eng. Mater.* **16**, 328–334 (2014).

183. Cha, J. & Daraio, C. Electrical tuning of elastic wave propagation in nanomechanical lattices at MHz frequencies. *Nat. Nanotechnol.* **13**, 1016–1020 (2018).

184. Süsstrunk, R. & Huber, S. D. Observation of phononic helical edge states in a mechanical topological insulator. *Science* **349**, 47 (2015).

185. Süsstrunk, R. & Huber, S. D. Classification of topological phonons in linear mechanical metamaterials. *Proc. Natl. Acad. Sci.* **113**, E4767–E4775 (2016).

186. Fahrenkrug, E., Gu, J. & Maldonado, S. Electrochemically gated alloy formation of crystalline InAs thin films at room temperature in aqueous electrolytes. *Chem. Mater.* **26**, 4535–4543 (2014).

187. Wang, Y., Xu, H., Zhang, J. & Li, G. Electrochemical sensors for clinic analysis. *Sensors* **8**, 2043–2081 (2008).

188. Jager, E. W. H., Smela, E. & Ingana, O. Microfabricating Conjugated Polymer Actuators. *Science* **290**, 1540 (2000).

189. Acerce, M., Akdoğan, E. K. & Chhowalla, M. Metallic molybdenum disulfide nanosheet-

based electrochemical actuators. *Nature* **549**, 370 (2017).

190. Thackeray, M. M. Manganese Oxides for Lithium Batteries. *Prog. Solid State Chem.* **25**, 1–71 (1993).

191. Ven, A. Van Der, Marianetti, C., Morgan, D. & Ceder, G. Phase transformations and volume changes in spinel LixMn2O4. *Solid State Ionics* **135**, 21–32 (2000).

192. Liu, C., Neale, Z. G. & Cao, G. Understanding electrochemical potentials of cathode materials in rechargeable batteries. *Mater. Today* **19**, 109–123 (2016).

193. Li, J., Ma, C., Chi, M., Liang, C. & Dudney, N. J. Solid electrolyte: The key for high-voltage lithium batteries. *Adv. Energy Mater.* **5**, 1401408 (2015).

194. Bates, J. B., Gruzalski, G. R., Dudney, N. J., Luck, C. F. & Yu, X. Rechargeable thin-film lithium batteries. *Solid State Ionics* **70/71**, 619 (1994).

195. Albertus, P., Babinec, S., Litzelman, S. & Newman, A. Status and challenges in enabling the lithium metal electrode for high-energy and low-cost rechargeable batteries. *Nat. Energy* **3**, 16 (2018).

196. Van De Burgt, Y. *et al.* A non-volatile organic electrochemical device as a low-voltage artificial synapse for neuromorphic computing. *Nat. Mater.* **16**, 414–418 (2017).

197. Fuller, E. J. *et al.* Parallel programming of an ionic floating-gate memory array for scalable neuromorphic computing. *Science* **364**, 570–574 (2019).

198. Jang, D. & Greer, J. R. Size-induced weakening and grain boundary-assisted deformation in 60 nm grained Ni nanopillars. *Scr. Mater.* **64**, 77–80 (2011).

199. Luo, J. K., Flewitt, A. J., Spearing, S. M., Fleck, N. A. & Milne, W. I. Young's modulus of electroplated Ni thin film for MEMS applications. *Mater. Lett.* **58**, 2306–2309 (2004).

200. Bažant, Z. P. & Cedolin, L. *Stability of Structures*. (World Scientific, 2010).

201. Hussein, M. I. & Leamy, M. J. Dynamics of Phononic Materials and Structures : Historical Origins , Recent Progress , and Future Outlook. *Appl. Mech. Rev.* **66**, 040802 (2015).

202. de Vasconcelos, L. S., Xu, R. & Zhao, K. Operando Nanoindentation: A New Platform to Measure the Mechanical Properties of Electrodes during Electrochemical Reactions. *J. Electrochem. Soc.* **164**, A3840–A3847 (2017).